博士論文

Growth mechanisms of InN on zirconia surfaces

(ジルコニア表面上での InN の成長メカニズム)

Doctoral dissertation

GUO Yao

(郭　堯)

Department of applied chemistry

The University of Tokyo

Abstract

Indium nitride (InN) is a promising candidate for the high speed electron device applications. Cubic stabilized zirconia (111) surfaces are found to provide the lattice matched surfaces for InN growth. Theoretical investigations can help us investigate the InN growth at the atomic scale when the experiment is limited. The growth mechanism at the initial stage could be investigated for further improvement of the InN on zirconia surfaces.

In the case of experiment, InN has been successfully grown on the yttria-stabilized zirconia (YSZ) substrate. The film's quality of InN on the YSZ can be improved on the basis of understanding of the growth mechanism. On the other hand, high-quality InN also can be expected on the manganese-stabilized zirconia (MnSZ) substrate due to the small lattice mismatch. In this thesis, growth mechanisms of InN were investigated theoretically on the pure cubic zirconia, YSZ and MnSZ which represent the Y-segregation-free or Mn-segregation-free, Y-segregated and Mn-segregated substrates.

The initial stages of InN growth on pure zirconia and YSZ (111) surface were investigated by energy calculation of N and In atoms adsorption on the surface. To calculate adsorption energies based on the density functional theory (DFT) reveals that nitrogen atoms are more strongly adsorbed on the zirconia (111) surfaces than indium atoms, suggesting that the first layer of InN (0001) should be a nitrogen layer. These arrangements lead to the experimentally-confirmed epitaxial relationship of InN [11-20] // zirconia [1-10]. These phenomena can be explained by the hybridization between N2*p* and O2*p* and that between N2*p* and *d*-orbitals of metal cations.

Furthermore the mechanisms of polarity determination of InN on Y-segregation-free and Y-segregated zirconia surfaces were investigated by DFT calculation of In atom on the N layer covered zirconia surfaces. The energy difference between In-polar and N-polar InN on the Y-segregation-free YSZ surface was quite small. On the other hand, In-polar InN on Y-segregated surfaces was more stable than N-polar InN. These results

are consistent with the experimental data. Strong In5*s* and O2*p* hybridization caused by short In-O bond on the Y-segregated surface stabilize the In-polar structure. The hybridization effect between N2*p* and *d*-orbital of transition metals affects the polarity determination of InN films on YSZ (111) surfaces.

Growth mechanism of InN films on lattice-matched MnSZ (111) surfaces is investigated to confirm the feasibility of epitaxial growth of InN films on MnSZ (111). It is found that nitrogen atoms are more strongly adsorbed to the surface than indium atoms, suggesting that the first layer of InN (0001) should be a nitrogen layer. These results lead to the in-plane epitaxial relationships of InN [11-20] // MnSZ [1-10] as the same as those on YSZ (111) substrates, that implies MnSZ (111) substrates work as lattice-matched substrates to obtain high quality InN films. Polarity determination of InN on MnSZ (111) is also studied based on adsorption of In atom on the N layer covered MnSZ surface. Indium atom preferentially adsorbs at the center of three nitrogen atoms stacked on the MnSZ substrate, which leads to the formation of In-polarity InN. It is found that the stability of In-polar InN structure affected by the In-O bond strength.

In general, the nitrogen atoms have more adsorption energies than indium atoms on the zirconia surfaces and the in-plane epitaxial relationship is InN [11-20] // zirconia [1-10], which is independent of the dopants among the three surfaces. Transition metal atoms segregated at the zirconia surface affect the adsorption energies of N and polarity determination of InN through hybridization between atoms at the surface.

List of the contents

Chapter 1 Introduction

1.1 The group III-nitrides

1.1 .1 Properties of the group III-nitrides

In the past few decades, the group III-nitrides AlN, GaN, InN and their alloys have drawn a lot of attention due to the excellent properties such as wide range of bandgap, high electron mobility, physical and chemical stability. The group III-nitrides could be widely applied in optoelectronics and electron devices. The group III-nitrides have the direct bandgap energy from 0.65 to 6 eV (Fig. 1-1). It is covering a spectrum range for most of the optoelectronics applications from near infrared (NIR) to ultra-violet (UV) [1.1]. This will make the III-nitrides and their alloys be capable to develop a broad range of applications in optoelectronic devices, such as light emitting diodes and laser diodes. Because of the wide bandgap energies of the nitrides such as GaN and AlN, the III-nitrides can provide a high breakdown voltage. It will make the nitride a good candidate in high power applications. The high electron saturation velocity and high electron mobility in the group III-nitrides make them promising materials for application in high-speed electron devices [1.2]. The group III-nitrides are thermally, mechanically and chemically stable compared to the conventional semiconductors such as Si and GaAs. [1.3] The good thermal stability is due to the high bonding energy. Hence, nitride-based devices can operate at high temperature. The inert nature of nitrides is a double-edged sword. On one hand, it will present resistance to chemical etching and then hinder the device fabrications. On the other hand, it will enable the nitride-based devices to operate in extreme environment.

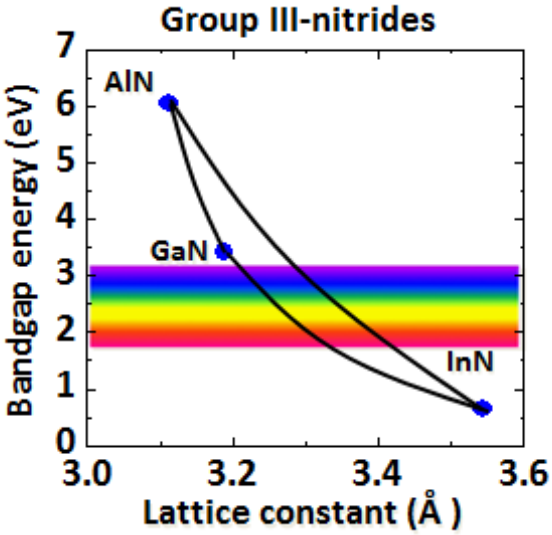

Fig. 1-1 Bandgap energies of the group III-nitrides as function of their lattice constants.

The III-nitrides can be grown either in wurtzite or zincblende phases depending on the growth conditions [1.4]. The former phase represents the equilibrium and the latter phase is metastable at normal conditions. Although the zincblende structure has been reported, the most investigated one is the wurtzite structure (Fig.1-2). The wurtzite structure of the III-nitrides can be described by the lattice constant *a* and *c* *(*Table 1.1*)*. InN, GaN and AlN have different lattice constants due to the differences in ionic radii (Al^{3+}: 0.39 Å, Ga^{3+}: 0.47 Å, In^{3+}: 0.79 Å) [1.5].

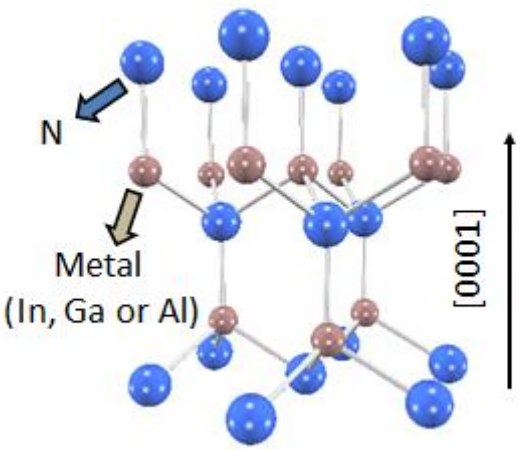

Fig. 1-2 Wurtzite crystal structure of nitride.

Table 1.1 Lattice constants and bonding energies of the nitrides [1.5].

	AlN	GaN	InN
a (Å)	3.11	3.19	3.54
c (Å)	4.98	5.18	5.71
E (eV)	11.52	8.92	7.72

Due to the absence of the inversion center, the wurtzite III-nitrides will have polarities on the most common growth direction of nitride is the c-plane (0001). The atoms are arranged in bilayers consisting of two closely spaced hexagonal layers. One consists of cations. The other consists of anions. The bilayers have polar faces: the N-polar and the metal (In, Ga or Al)-polar. It shows us the atomic structures of the In-polar and N-polar InN in Fig. 1-3. For In-polarity it means indium on the top position of the [0001] bilayer, corresponding to [0001] polarity. On the contrary, it means the nitrogen on the top position of the [0001] bilayer for the N-polarity. The definitions of the two polarities are also applicable in the cases of GaN and AlN.

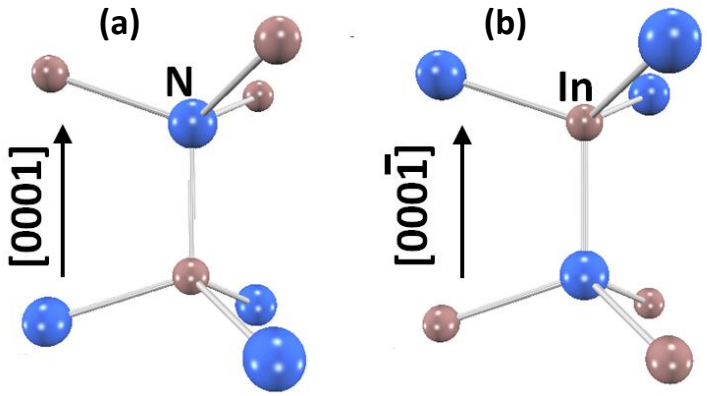

Fig. 1-3 Atomic structure of (a) In-polar and (b) N-polar InN.

The wurtzite nitrides in the *c*-plane lead to the existence of a piezoelectric polarization field and associated electrostatic charge densities in the strained materials. At the same time the nitrides possess a spontaneous polarization [1.6]. The uniform piezoelectric and spontaneous polarization fields are nullified spatially in bulk material because of the rearrangement of surface charges. However, in case of the heterostructures or inhomogeneous alloy layers, variations in composition are expected to create nonvanishing spontaneous and piezoelectric polarization fields and associated charge densities that can dramatically influence material properties and device behavior [1.6].

1.1.2 Epitaxial growth of the group III-nitrides

There is no doubt that the single crystals nitride is superior to the hetero epitaxy nitride to fabricate high performance devices. At the present stage, the supply of nitride bulk substrates is very limited. Especially, the bulk growth of GaN has been researched for a long time. The hydride vapour-phase epitaxy (HVPE) [1.7] is considered to be the most promising method to obtain the GaN bulk because of the high growth rate. However, the HVPE still faces the challenges of inefficiency and high cost.

The hetero epitaxial growth is employed to fabricate the cost-effective nitride. The nitrides are currently grown on the foreign substrates. In case of the hetero epitaxy, the most important factors regarding to the foreign substrates are the lattice mismatch, thermal expansion mismatch, the chemical stability, and so on. The most commonly used substrate for nitride growth is the sapphire substrate because of its wide availability, hexagonal symmetry, easy pre-growth cleaning and high temperature stability (~1000°C). At the same time, there are large lattice and thermal expansion mismatches between the nitrides and the sapphire substrates. It will produce the dislocations and strain in the nitride film and reduce the performance of the nitride-based devices at last.

Many growth techniques have been developed to realize the epitaxial growth of the group III–nitrides. Metal organic chemical vapor deposition (MOCVD) [1.8] and molecular beam epitaxy (MBE) [1.9] become dominating techniques to grow nitrides. They represent essentially 100% of the epitaxial tools used in the commercial production of nitride devices. The characteristics of the two methods are summarized in Table 1.2.

The MOCVD and the related technique have driven most parts of the progress in the nitrides epitaxial growth field. It has the special features such as fast growth, mass production, high growth temperature, use of toxic gas, and so on. The MOCVD is mostly used in the industrial production and research.

The MBE also has been widely used in nitrides research. Compared to MOCVD, MBE has the characteristic such as relatively low growth temperature, the possibility of in-situ monitoring, and better control of thickness. The MBE is mainly used for the research and development.

Table 1.2 The characteristics of MOCVD and MBE for GaN growth.

	MOCVD	MBE
Growth temperature (°C)	1000 – 1100	850 – 900
Growth rate (μm/hr.)	several	up to 1
Growth pressure (torr)	up to 1	1×10^{-8}
Growth source	solid	gas

The growth of nitrides suffers from lack of stable substrates because the interface reactions will happen at high temperatures. Reducing temperature growth will provide a solution to eliminate the interface reactions. At the same time, the pulsed laser deposition (PLD) technique is found to solve the problem [1.10]. With the help of the laser ablation, the film precursors can possess the high kinetic energies even at a relatively low temperature [1.11]. As a result, nitride can be grown on many different kinds of substrates by utilization of PLD, which are impossible for the conventional growth methods. In fact, it has been reported that the PLD technique enables us to grow GaN films epitaxially even at room temperature (RT) with a typical layer-by-layer mode on nearly lattice-matched substrates [1.12-1.14].

1.2 Indium nitride

1.2 .1 Excellent properties of InN

InN has the narrowest bandgap energy among the group III–nitrides. One reason is

that the p-d repulsion in InN pushes the valence band maximum (VBM) to higher energies [1.15]. Another is that the relatively long In-N bond will change of the conduction band edge [1.15]. For a long time there was a debate on the bandgap energy of InN because of a lack of high crystalline film quality. Recent advances in III-nitride deposition techniques have realized the growth of high quality InN films. An updated band gap value of 0.65 eV was established at last [1.16]. The smaller band gap value of InN has expanded the bandgap range of the III-nitride and opened the new application. For example, the band gap of InGaN alloy ranges from 0.65 to 3.43 eV. The minimum of 0.65 eV is determined by InN when the proportion of GaN is zero. The III-nitride alloy has attracted considerable attention for the fabrication of the LEDs with a wide range of wavelength.

Table 1.3 Physical properties of Si, GaAs, InN and GaN.

	Si	GaAs	InN	GaN
Crystal structure	Diamond	Zincblende	Wurtzite	Wurtzite
Electron mobility (cm^2/Vs)	1500	8500	4400	1200
Saturation velocity (cm/s)	1.0×10^7	2.0×10^7	6.0×10^7	3.0×10^7
Electric breakdown field (V/cm)	3.0×10^5	4.0×10^5	2.6×10^6	3.3×10^6
Bandgap (eV)	1.12	1.42	0.65	3.43
Absorption coefficient (cm^{-1})	1×10^4	2.3×10^4	$1\text{-}1.5\times10^5$	3.0×10^5
Thermal conductivity (W/cm·K)	149	0.55	45	2.3
Transition	Indirect	Direct	Direct	Direct

InN is found to have promising potential applications in photovoltaics and near infrared (NIR) photodetection [1.17]. As a candidate material for the new generation solar cell, the high radiation resistance makes InN suitable for the cell used for the satellites operating at the outer space. InN also has the additional advantages such as

high thermal conductivity and a large absorption coefficient. All of these above important features make the nitride-based solar cell can operate in severe environments that are not suitable for a Si cell. In case of the near infrared (NIR) photo detectors, the most devices have been composed of toxic elements such Pb, Se and As. InN containing no toxic elements could be used for replacing the current materials. Until now, the realistic InN-based is still limited because of the surface accumulation layer, large leakage current and the *p*-type doping [1.17].

InN has the highest transport property among the group III–nitrides. The smallest electron effective mass of InN among the III–nitrides leads to the highest electron mobility in the III–nitrides. The theoretical maximum electron mobility of InN in low carrier concentration 1.0×10^{16} is about 4400 cm^2/Vs at 300 K [1.18]. The value is beyond 30000 cm^2/Vs at 77 K because of the weak phonon scattering [1.18]. Moreover, InN also has the highest saturation velocity among the III–nitrides. Bhuiyan [1.19] has reported the velocity–field characteristics of the several III–V semiconductors including GaN, InN, AlN and GaAs. In the report, InN achieves the highest steady-state peak drift velocity: 4.2×10^7 cm/s. The excellent transport property makes InN potentially applicable in high-speed electron devices. Table 1.3 shows the physical characteristics associated with Si, GaAs, wurtzite GaN and InN.

In addition, the transport characteristics of InN were shown to be relatively insensitive to variations in temperature and doping concentration [1.19] because the InN has relatively large optical phonon energy. For example, it has been reported that the transport characteristics of InN are superior to those of GaN and GaAs not only in the temperature range from 150 K to 500 K but also in the doping concentration range up to 1.0×10^{19} cm^{-3} [1.20]. This suggested that InN-based devices may have a better performance.

1.2.2 High speed applications of InN-based devices

The development of the InN-based field effect transistors (FETs) moves slowly for a

long time because of the difficulty in fabricating high quality InN heterostructure. The advance in the epitaxial growth of InN will change this situation. The film quality of InN is improved in recent years. High speed applications of the InN-based devices could be expected. It gives us the structure of InN-based Metal-Insulator-Semiconductor field effect transistor (MISFET) reported by Lin [1.21] in Fig. 1-4. Even though the InN-based FET has been demonstrated, it still faces many challenges such as the lack of demonstrated dielectric layer, inability to form Schottky contacts and the intrinsic accumulation layer on the InN surface. The device performances need further improvement to match the excellent transport properties of InN.

The high electron mobility transistors (HEMTs) [1.22] utilizing the novel properties of the two-dimensional electron gas (2DEG) [1.22] are promising for the applications in high frequency operation. The HEMT is developed for high speed application at the beginning. And then the device exhibits the good noise performance due to the less electron collisions. It provides a combination of the low noise figure and the ability to operate at the very high frequencies. Accordingly the HEMT can be widely used in a wide range of radio frequency (RF) applications including cellular telecommunications, direct broadcast receivers (DBS), radar and radio astronomy. Up to now, the most common materials used in HEMT are aluminum gallium arsenide (AlGaAs) and gallium arsenide (GaAs) because they provide a high level of basic electron mobility, which is crucial to the operation of the device. Silicon is rarely used in a HEMT because of its much lower level of electron mobility (Table 1.3).

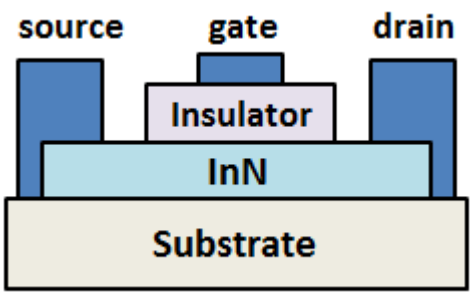

Fig. 1-4 InN-based Metal-Insulator-Semiconductor field effect transistor (MISFET).

The group III-nitrides have been recognized as promising materials for designing HEMT according to their highly attracting inherent properties such as high electric breakdown field, high thermal conductivity and high saturation velocity over the existing GaAs. Besides that, the 2DEGs in the nitride-based HEMT are polarization-induced. It means the intentional doping is not required when it is needed in the GaAs-based HEMT. Until now extensive studies have been carried out to optimize the AlGaN/GaN HEMT. The GaN-based HEMTs have already been commercialized. The key parameter to describe the high frequency performance is the cut-off frequency. Recent studies show that reduction of gate length has improved the cut-off frequency of the device. However, reduction of the gate length is limited by the saturation of electron drift velocity [1.23]. As a result, material with high electron saturation velocity is required for the gate scaling process.

InN has the highest saturation velocity among the III-nitrides. It will be helpful to solve the problem in the gate scaling process. The InN-based HEMTs seems to have the superiority over other conventional GaN-based HEMTs due to its superior transport properties as mentioned above. However, as the same as the InN-based FET, the research on InN-based HEMT is just at initial stage compared with GaN-based HEMTs. There are only a few reports on the InN-based HEMTs because the fabrication of the high quality InN film is very difficult [1.24].

It shows us the cross-sectional structure of a reported InN-based HEMT [1.25] in Fig.1-5. In a GaN-based HEMT, the devices rely on the formation of a high mobility electron accumulation layer at the AlGaN/GaN interface. In case of the InN-based HEMT, it will be replaced by the InN/InGaN interface. The significant lattice mismatch between InN and InGaN can result in a large piezoelectric polarization [1.26]. In addition, the spontaneous polarization is also very large in the nitrides. The polarization induced electric field will lead to a significant increase of the sheet carrier concentration at the heterointerface. At the same time, a large conduction band discontinuity will result in better electron confinement at the heterointerface. The electron accumulation layer at the interface is the 2DEG exactly. Within this region the

electrons are able to move freely because there are no other obstructions and the mobility of the electrons in the gas is very high. The conductivity of the high mobility accumulation layer can be modulated quite quickly by the gate voltage.

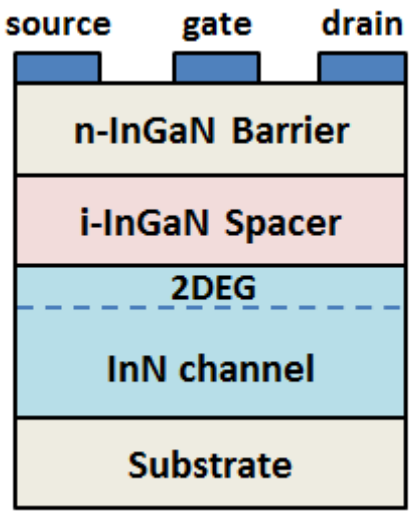

Fig.1-5 Schematic structure of InN-based HEMT.

1.2.3 Epitaxial growth of InN

The excellent properties of InN show us a promising prospect in the electronic and optoelectronic field. The key point is that the high performances devices require high quality materials, either InN or its alloys. However, the growth of InN is most undeveloped among the III-nitrides. The epitaxial growth of InN is difficult because of the low decomposition temperature and lack of proper substrates. Until now, MBE and metal organic vapor phase epitaxy (MOVPE) carry the main burden of the InN growth. The film quality of the InN is unsatisfied. Further improvement of the growth is required since the excellent transport property only can be demonstrated in the high crystalline quality film.

To date, recent progress in high-quality InN layers on GaN epilayer on sapphire

substrates by using boundary-temperature-controlled epitaxy have been reported. The film quality is improved with increasing layer thickness and a recorded electron mobility of ~3280 cm^2/Vs is obtained with the electron concentration of $1.47\times10^{17}cm^{-3}$ [1.27]. N. Khan *et al*. had reported the *c*-plane InN growth on AlN epilayer templates by MOCVD [1.28]. The improvement in electron mobility is attributed to AlN layer which allows for reduction in the related defects. Even though the growth high mobility InN is realized with the thick film, the electron mobility for the thin film thickness is still poor. The ultrathin InN film on the insulating substrates can be used for the channel layers of FETs. High electron mobility is required in the thin InN film too. It has been reported that yttria stabilized zirconia (YSZ) substrate by pulse sputter deposition (PSD) can be used for the ultrathin InN growth [1.29]. InN thin film has the higher electron mobility on YSZ than that on the GaN substrate.

1.3 Epitaxial growth of InN on YSZ substrates

Among the III-nitrides, the growth InN is the most difficult. The development of InN growth is relatively slow compared with the other nitrides.

One reason is that the growth of InN requires a relative low temperature compared with the other nitrides because of the dissociation temperature and high equilibrium N_2 vapor pressure over the InN film [1.30, 1.31]. InN decomposes at around 600 °C, which determines the upper limit of the growth temperature. As a result, it is difficult to realize the growth of high quality InN films since the conventional growth methods usually operate at the high temperature.

Development of a new growth technique is inherently needed to improve the film quality. The precursor on the surfaces should have large migration energies. Pulsed laser deposition (PLD) and the related pulse sputter deposition (PSD) are promising candidates for this purpose. It will give high kinetic energies to the group-III atoms

when they impinge onto the surface [1.11-1.13] as mentioned before. In previous section we have already known that epitaxial growth of AlN and GaN can be realized at low growth temperatures even at room temperature. With the help of PLD, III-nitrides can be grown on various substrates. It also includes those cannot be used as substrates by the conventional methods due to their high reactivity with nitride precursors. Therefore, the PLD is an appropriate technique for the epitaxial growth of InN.

Besides the problem of the low growth temperature, there is another problem for InN growth. Same as the other nitride, InN bulk substrates is still under investigation and far from application. Hetero epitaxial growth of InN on a foreign substrate is required when the bulk substrate is limited. The requirements for the nitride growth are very strict. The substrates must have thermal and chemical stability. On one hand, it is known that the environment of nitride growth is usually at a high temperature. The temperature is about 580 °C in case of InN. The nitrogen source is very active in such a high temperature. On the other hand, the chemical reaction at the interface must be prevented for a better high film quality. All of these limits are the reason why InN lacks of substrates. Until now the most used substrates for InN growth are sapphire and GaN substrates. Unfortunately, the lattice mismatches between the substrates and InN film are 29% for sapphire and 11% for GaN. The large lattice mismatch between the InN and substrate will cause the structural defects at the interface. For example it has been reported that InN/GaN interface has a high density of misfit dislocation (MD) [1.32, 1.33].

It is known that the structural defects extended from the hetero interface such as dislocations and stacking faults will adversely affect III-nitride device properties. It will cause nonradiative recombination, carrier scattering effects, and diffusion of dopants and impurities [1.34-1.36]. It is well known that film quality of the semiconductor material is inherently important to the III-V device performance. Especially, the threading dislocation (TDs) is a very important factor to the film quality. It will affect the performance of the III-V devices deleteriously. For example, TD densities greater than 10^4 cm^{-2} will greatly decrease the device efficiencies for the GaP and GaAs based

devices [1.37]. In the case of the nitrides, it is fortunate that the nitride-based devices can still work at the much higher TD densities (as high as 10^{10} cm^{-2}). Therefore, the reduction of the structural defects and improvement of the film quality are inherently important for III-V including the III-nitrides.

Since the structural defects are so important, a lot of research works have been taken on this related field. The developments of the growth techniques enable us to investigate the relation between the film quality and the defects. According to the investigations, people have reached a consensus that the TDs are the dominant scattering centers limiting the mobility of electrons in the InN [1.38]. TD strain scattering should be the dominant mechanism in limiting the mobility of electrons in InN [1.32]. For instance, tables 1.4 and 1.5 show us the simulative and experimental results of the dependence of the electron mobility as a function of the TD density [1.39, 1.40]. It is obviously shown that the electron mobility is greatly affected by the TD density. The dislocations affect the transport in the InN not only through the Coulomb interaction of electrons with charged dislocation cores, but also due to the induced lattice strain surrounding dislocations [1.41]. It gives us a simple model of the epilayer on substrate with a threading dislocation (TD) segment [1.42] in Fig. 1-6.

Table 1.4 Dependence of electron mobility on TD density by MC simulation [1.39].

TD Density (cm^{-2})	10^7	10^8	10^9	10^{10}
Electron mobility (cm^2/Vs)	12500	10000	4500	900

Table 1.5 Dependence of electron mobility on TD density in experiment [1.40].

TD Density (cm^{-2})	2.0×10^{10}	4.5×10^{10}	6.5×10^{10}	14×10^{10}
Electron mobility (cm^2/Vs)	1750	1250	850	≤300

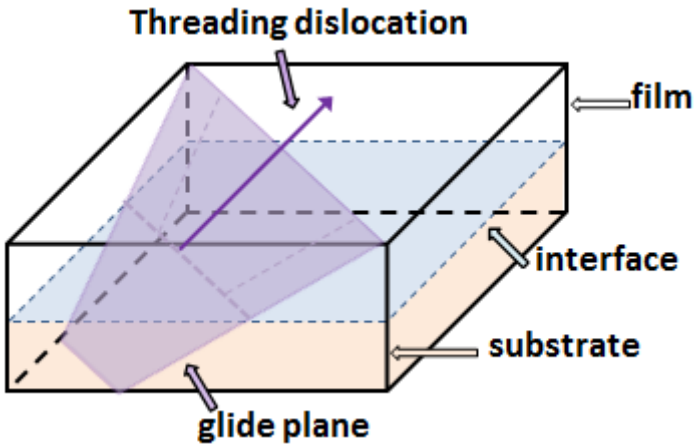

Fig. 1-6 Schematic illustration of the threading dislocation (TD).

The origin of the TDs is the large lattice mismatch between the substrate and the InN epilayer. The TD density must be reduced for the high electron mobility of the film. A search for new substrate materials with small lattice mismatch is inherently important. It has been known that the yttria stabilized zirconia (YSZ) (111) substrates could be a good candidate for the InN growth because it shares the threefold rotational symmetry with the InN c-plane and possibly gives a lattice mismatch of just 2.3% (Fig. 1-7). Utilizing the (111) plane of YSZ seems to resolve the problem of high TD density.

.

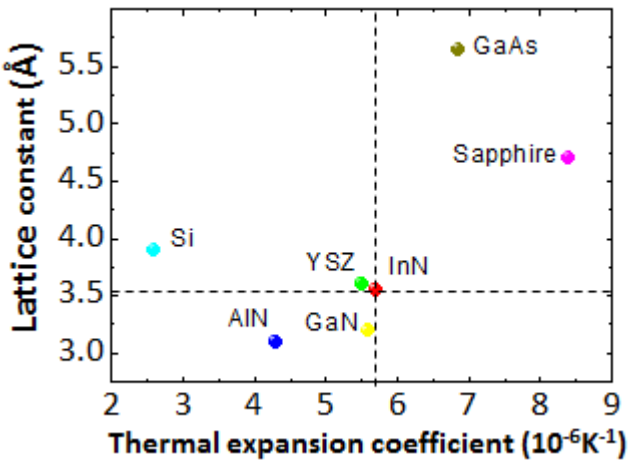

Fig. 1-7 Lattice constant *a* (Å) and thermal expansion coefficient *a* ($10^{-6}K^{-1}$) of various materials at 300 K [1.43-1.45].

The epitaxial growth of InN on YSZ still faces the challenge even though it has the advantage of small lattice mismatch. It is known that the strong interface reactions will degrade the film quality in hetero epitaxial growth. In case of the YSZ substrate, epitaxial growth of InN is difficult because the interface reaction occurs easily. To prevent the interface reaction, development of the epitaxial growth is required. As mentioned before, PLD has the special features of high kinetic energies and less interface reactions. Therefore, the PLD is appropriate for InN growth on YSZ substrates. It shows us the crystal structure of the YSZ (111) plane [1.46] in Fig.1-8.

In fact the epitaxial growth of InN films on YSZ (111) substrates have already been realized in the previous reports [1.47, 1.48]. Among these reports, utilizing the PLD techniques seemed to be a feasible solution to grow InN on YSZ substrates. The difficulties in the InN growth on YSZ can be solved by PLD techniques due to the special properties such as low temperature growth, less interface reaction and high kinetic energies. The details of InN growth on YSZ will be discussed in chapter 3.

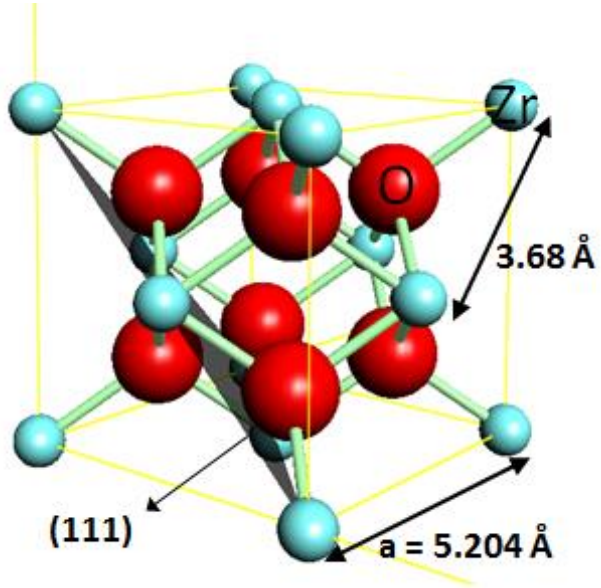

Fig. 1-8 Structure of the (111) plane of YSZ.

According to the experimental results [1.48], the epitaxial relationship between InN and YSZ was found to be InN (11-00) / /YSZ (11-0) and [0001] / /YSZ [111], which gives a small lattice mismatch of 2.3%. The in-plant epitaxial relationship between InN and

YSZ was obtained from the characterization using the XRD and RHEED. It can be found that the FWHM for the InN -202-4 X-ray rocking curve is 980 arcsec. The threading dislocation density in the InN film is 10^9 cm^{-2}. It shows cross sectional TEM observations of the InN/YSZ heterointerface [1.48] in Fig.1-9. The super-imposed picture is a magnified image of the interface [1.48]. It is found that the InN/YSZ heterointerface is atomically abrupt. There is no nitridation or buffer layers are employed during the InN growth. The abrupt interface will enable us to characterize the interfacial structure and to investigate the growth mechanism of InN at the initial stage. [1.49]

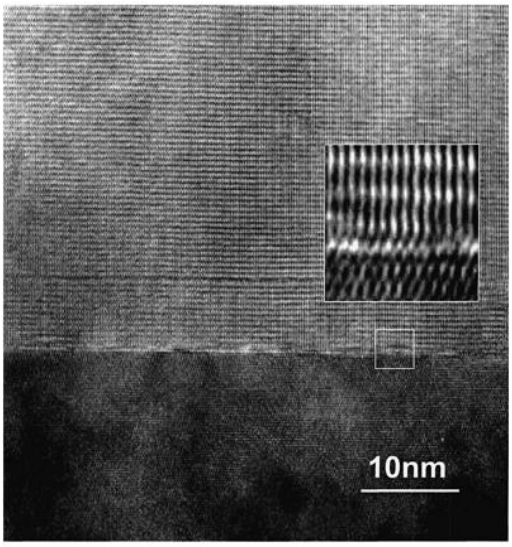

Fig.1-9 TEM lattice image of InN on YSZ (111) reprinted with permission from Journal of Vacuum Science and Technology A **22**, 2487 (2004) Copyright 2004, American Vacuum Society.

Recently it has been reported that the growth of the first several monolayers of InN on YSZ has much higher electron mobility than the conventional grown InN [1.29]. It indicates that the structural quality of the InN/YSZ hetero interface and the smooth surface are inherently important for obtaining high quality InN ultrathin films. Consequently, it can be known that the initial stage is so important to the film quality of the InN epilayer.

1.4 Motivation and purposes

As mentioned in the past sections, the YSZ substrates is known as promising candidate for the hetero epitaxial growth of InN because of the small lattice mismatch. In current condition, the film quality of InN is still far from satisfied even though the epitaxial growth of InN on YSZ substrates have been successfully reported [1.29, 1.47, 1.48]. It is known that the electron mobility of the InN film in the experiment is still far away from the theoretical value. In other words, there is a very large potential that the crystalline quality of the film could be further improved. Hence, in the case of the InN growth on cubic stabilized zirconia substrates including pure zirconia, YSZ and MnSZ, the further improvement of the crystalline quality is still inherently required to realize the high performance InN-based devices.

Until now, the phenomena that occur during the initial stage of InN growth on the substrates have not yet been well understood on the atomic scale. Therefore, to understand the growth mechanisms of this material system, it is important to develop a theoretical approach because the experimental techniques that are applicable for this highly resistive substrate are limited.

In the meantime, the polarity control of InN on the substrates is a crucial issue because the polarity of InN film seriously affects the device performance. Mixture of the In- and N-polar InN must be prevented during the growth. Recently, it is found that In-polarity *c*-plane InN can be reproducibly grown using the Y-segregated YSZ substrate [1.50]. The phenomenon is caused by surface segregation of Y atoms. The experimental technique at the present stage is limited to explain this phenomenon. Therefore, for further improvement of this polarity control technique, a theoretical investigation of *c*-plane InN on the substrates is quite important.

For these above reasons, it is necessary to carry out the theoretical study to investigate the growth mechanism of InN on the zirconia surfaces. In fact the theoretical study has been employed to investigate the growth mechanism of nitride on various substrates [1.49-1.54]. In the case of InN/YSZ system, there are only a few

experimental studies on it because the epitaxial growth of InN on the YSZ is difficult because of interface reactions. On the other hand, the theoretical investigation on such promising interface is still missing so far. Hence, theoretical study should be employed to investigate the InN/YSZ system.

Furthermore, the lattice mismatch between InN and YSZ could be reduced by introducing of the MnSZ substrate. Improved film quality can be expected on the MnSZ substrate.

The principle purpose of this doctoral thesis is the investigation of the growth mechanism of the InN growth on the zirconia surfaces based on the first principles calculation. Firstly, in order to understand the initial stages of InN growth and the in-plane epitaxial relationship formation, adsorption energies of In and N on the (111) plane of pure zirconia, YSZ and MnSZ are investigated. Secondly, on the basis of the initial stage adsorption, the mechanisms of polarity determination of InN on pure zirconia, Y-segregated zirconia and Mn-segregated zirconia surfaces are investigated by energy calculation of In atom on the N layer covered zirconia surfaces.

In chapter 1 the basic relevance of the nitride semiconductor especially the general situation about the InN materials were introduced. Finally the purpose of this doctoral thesis was presented. It is the theoretical investigation of the InN growth mechanism on zirconia surfaces. In chapter 2, it provides a general introduction of the computational modeling methods which are employed in this thesis. In chapter 3, the initial stage of InN growth on the YSZ (111) substrates are investigated based on the first principles calculations. In chapter 4, the polarity determination of the InN on the YSZ (111) substrates by theoretical study based on the results of chapter 3.In chapter 5, an attempt to investigate the InN growth on MnSZ (111) substrates by theoretical study is performed. Both the initial stage of growth and polarity determination investigations are carried out to make comparison to the results of the YSZ substrates. In chapter 6, the conclusions and outlook will be presented.

Reference

[1.1] F. A. Ponce and D. P. Bour, Nature **386**, 531 (1997).

[1.2] S. K. O'Leary, B. E. Foutz, M. S. Shur, U. V. Bhapkar and L. F. Eastman, J. Appl. Phys. **83**, 826 (1998).

[1.3] M. Ueno, M. Yoshida, A. Onodera, O. Shimomura and K. Takemura, Phys. Rev. B **49**, 14 (1994).

[1.4] J. W. Orton and C. T. Foxon, Rep. Prog. Phys. **61**, 1 (1998).

[1.5] O. Ambacher, J. Phys. D: Appl. Phys. **31**, 2653 (1998).

[1.6] E. T. Yu, X. Z. Dang, P. M. Asbeck, S. S. Lau and G. J. Sullivan, J. Vac. Sci. Technol. B **17,** 1742 (1999).

[1.7]K. Fujioto, S. Kubo, H. Nagaoka, ,T. Mochizuki, H. Namita and S. Nagao, J. Crystal Growth. **311**, 3011 (2009).

[1.8] B.-C. Chung and M. Gershenzon, J. Appl. Phys. **72**, 651 (1992).

[1.9] R. C. Powell, N.-E. Lee and J. E. Greene, Appl. Phys. Lett. **60**, 2505 (1992).

[1.10] J. Ohta, H. Fujioka, H. Takahashi, M. Sumiya and M. Oshima, J. Crystal Growth. **233**, 779 (2001).

[1.11] M. H. Kim, M. Oshima, H. Kinoshita, Y. Shirakura, K. Miyamura, J. Ohta, A. Kobayashi and H. Fujioka, Appl. Phys. Lett. **89**, 031916 (2006).

[1.12] A. Kobayashi, J. Ohta and H. Fujioka, J. Appl. Phys. **99**, 123513 (2006).

[1.13] J. Ohta, H. Fujioka and M. Oshima, Appl. Phys. Lett. **83**, 3060 (2003).

[1.14] K. Sakurada, A. Kobayashi, Y. Kawaguchi, J. Ohta and H. Fujioka, Appl. Phys. Lett. **90**, 211913 (2007).

[1.15] T.D Veal C.F. MnConville and W. J. Schaff, Indium Nitride and Related Alloys.

[1.16] J. L. Lyons, A. Janotti and C. G. Van de Walle, Phys.Rev. Lett. **108**, 156403 (2012).

[1.17] W.-J. Lai, S.-S. Li, C.-C. Lin, C.-C. Kuo, C.-W. Chen, K.-H. Chen and L.-C. Chen, Scripta Materialia **63**,653 (2010).

[1.18] V. W. L. Chin, T. L. Tansley and T. Osotchan, J. Appl. Phys. **75**, 7365 (1994).

[1.19] Bhuiyan, Hashimoto and Yamamoto, J. Appl. Phys. **94**, 2779 (2003).

[1.20] B. E. Foutz, S. K. O'Leary, M. S. Shur and L. F. Eastman, J. Appl. Phys. **85**,7727 (1999).

[1.21] Y. S. Lin, S. H. Koa, C. Y. Chan and S. S. H. Hsu, Appl. Phys. Lett. **90**, 142111 (2007).

[1.22] W. Knap, Y. Deng, S. Rumyantsev, J. Q, Lu, M. S. Shur, C. A. Saylor and L. C. Brunel, Appl. Phys. Lett. **80**, 3433 (2002).

[1.23] K. Shoinohara, Y. Yamashita, A. Endoh, K. Hikosaka, T. Matsui,T. Mimura and S. Hiyamizu, IEEE Electron Device Lett. **22**, 507 (2001).

[1.24] V. M. Polyakov and F. Schwierz, J.Appl. Phys. **101**, 033703 (2007).

[1.25] K. Jeganathan, V. Purushothaman, R. K. Debnath, R. Calarco and H. Luth, Appl. Phys. Lett. **97**, 093104 (2010).

[1.26] I. Mahboob, T. D. Veal, C. F. McConville, H. Lu and W. J. Schaff, Phys.Rev. Lett. **92**, 036804 (2004).

[1.27] X.-Q. Wang, S.-T. Liu, N. Ma, L. Feng, G. Chen, F.-J. Xu, N. Tang, S. Huang, Kevin J. Chen, S.-Q. Zhou and B. Shen, Applied Physics Express **5,** 015502 (2012).

[1.28] N. Khan, A. Sedhain, J. Li and H. X. Jiang, Appl. Phys. Lett. **92**, 172101 (2008).

[1.29] K. Okubo, A. Kobayashi, J. Ohta, M. Oshima and H. Fujioka, Appl. Phys. Lett. **102**, 022103 (2013).

[1.30] O. Ambacher, M. S. Brandt, R. Dimitrov, T. Metzger, M. Stutzmann, R.A. Fischer, A. Miehr, A. Bergmajer and G. Dollinger, J. Vac. Sci. Tech-nol. B **14**, 3532 (1996).

[1.31] J. B. McChesney, P. M. Bridenbaugh and P. B. O'Connor, Mater. Res.Bull. **5**,783 (1970).

[1.32] E. Bellet-Amalric, C. Adelmann, E. Sarigiannidou, J. L. Rouvière, G. Feuillet, E. Monroy and B. Daudin, J. Appl. Phys. **95**, 1127 (2004).

[1.33] V. Lebedev, V. Cimalla, J. Pezoldt, M. Himmerlich, S. Krischok, J. A. Schaefer, O. Ambacher, F. M. Morales, J. G. Lozano and D. González J. Appl. Phys. **100**, 094902 (2006).

[1.34] S. J. Rosner, E. C. Carr, M. J. Ludowise, G. Girolami and H. I. Erikson, Appl. Phys. Lett. **70**, 420 (1997).

[1.35] N. G. Weimann, L. F. Eastman, D. Doppalapudi, H. M. Ng and T. D. Moustakas, J. Appl. Phys. **83**, 3656 (1998).

[1.36] V. Lebedev, F. M. Morales, H. Romanus, S. Krischok, G. Ecke, V. Cimalla, M. Himmerlich, T. Stauden, D. Cengher and O. Ambacher, J. Appl. Phys. **98**, 093508 (2005).

[1.37] W. A. Brantley, O. G. Lorimor, P. D. Dapkus, S. E. Haszko and R. H. Saul, J. Appl. Phys. **46**, 2629 (1975).

[1.38] D. C. Look, H. Lu, W. J. Schaff, J. Jasinski and Z. Liliental-Weber, Appl. Phys. Lett. **80**, 258 (2002).

[1.39] V. M. Polyakov and F. Schwierz J. Appl. Phys. 101, 033703 (2007).

[1.40] C. S. Gallinat, G. Koblmuller and J. S. Speck, Appl. Phys. Lett. **95**, 022103 (2009).

[1.41] D. Jena and U. K. Mishra, Appl. Phys. Lett. **80**, 64 (2002).

[1.42] C. S. Gallinat, G. Koblmüller, Feng Wu and J. S. Speck, J. Appl. Phys. **107**, 053517 (2010).

[1.43] H. Hayashi, T. Saitou, N. Maruyama, H. Inaba, K. Kawamura and M. Mori, Solid State Inonics, **176**, 613 (2005).

[1.44] Optical Materials, Lasertech Inc.

[1.45] A. Hill Growth, characterization and thermodynamics of III-nitrides semiconductors. Arizona State University (2011).

[1.46] J. Oswald, R. Gracie, R. Khare and T. Belytschko, Comput. Methods Appl. Mech. Engrg. **198**, 1872 (2009).

[1.47] P. A. Anderson, C. E. Kendrick, R. J. Kinsey, A. Asadov, W. Gao, R. J. Reeves and S. M. Durbinphys. Phys. Status Solidi C **2**, 2320 (2005).

[1.48] T. Honke, H. Fujioka, J. Ohta and M. Oshima, J. Vac. Sci. Technol. A **22**, 2487 (2004).

[1.49] J. Ohta, H. Fujioka, M. Oshima, K. Fujiwara and A. Ishii, Appl. Phys. Lett. **83**, 3075 (2003).

[1.50] A. Kobayashi, K. Okubo, J. Ohta, M. Oshima and H. Fujioka, Phys. Status Solidi A **209**, 2251 (2012).

[1.51] S. Sanna and W. G. Schmidt, Appl. Surf. Sci. **256**, 5740 (2010).

[1.52] A. Ishii, T. Tatani and K. Nakada, Phys. Status Solidi C **8**, 1585 (2011).

[1.53] K. Fujiwara, A. Ishii, J. Ohta, H. Fujioka and M. Oshima, Thin Solid Films **464/465**, 112 (2004).

[1.54] K. Okamoto, S. Inoue, N. Matsuki, T.-W. Kim, J. Ohta, M. Oshima, H. Fujioka and A. Ishii, Appl. Phys. Lett. **93**, 251906 (2008).

Chapter 2 Computational Methodology

Over the past few decades, the computer modeling has been developed into a useful tool for prediction and understanding the materials in chemistry and physics. With the help of the computer, we can solve the Schrödinger equation at some level of approximation to understand the electronic structure of the system. The intensive growth of computational power makes it now possible to deal with the complicated mathematical relations of quantum mechanics for the complex solid-state systems. In chapter 2, the theoretical calculation method employed in this thesis will be presented.

2.1 Density Functional Theory (DFT)

The first principles calculations are based on the density functional theory (DFT). The DFT replaces the many body electronic wavefunctions with the electron density as the basic quantity. It is known that the wavefunction is not a physically observable but a purely mathematical construct. On the contrary, the electron density is a physical characteristic of all molecules. The wavefunction will become complicated mathematically when the number of electrons increases (spatial and spin variables for each of the electrons). Fortunately, it is easier to calculate for the density functional because the density functional theory depends only on density as the function. More importantly, DFT methods can overcome one main disadvantages of Hartree-Fock theory: electron correlation [2.1, 2.2]. In the Hartree-Fock methods the electron correlations were completely neglected. Up to this point, DFT methods can significantly increase the calculation accuracy without the additional cost in computing time.

2.1.1 Schrödinger Equation and Born-Oppenheimer approximation

According to the quantum mechanics, the quantum state of a physical system changes in time could be described by the Schrödinger equation. Because the time-dependent Schrödinger equation is too difficult to solve except for extremely small systems. Most quantum mechanical approaches attempt to solve the time-independent and non-relativistic Schrödinger equation. The non-relativistic equation can be written as:

$$\hat{H}\psi = E\psi\,, \tag{2.1}$$

$$H = \sum_i \frac{\mathrm{p}_i^2}{2\mathrm{m}} + \sum_i \frac{\mathrm{p}_i^2}{2\mathrm{M}_i} + \frac{1}{2}\sum_{i\neq j}\frac{\mathrm{e}^2}{\left|\mathbf{r}_i - \mathbf{r}_j\right|} - \sum_{i,j}\frac{\mathrm{e}^2 Z_j}{\left|\mathbf{r}_i - \mathbf{R}_j\right|} + \frac{1}{2}\sum_{i\neq j}\frac{\mathrm{e}^2 Z_i Z_j}{\left|\mathbf{R}_i - \mathbf{R}_j\right|}. \tag{2.2}$$

Here Ψ is the wavefunction and E is the energy of the system. The Hamiltonian (H) of the system is given in eq. 2.2. The nuclei are described by coordinates R and the masses M, electrons are described by coordinates r, masses m and the momenta p.

The Born-Oppenheimer approximation [2.3] is based on the fact that nuclei are several thousand times heavier than electrons. Due to this reason the electrons move much faster than the nuclei. Hence, the electrons can be taken as particles responding instantaneously to the motion of the nuclei without a finite relaxation time. The change in nuclei configuration is negligible during the time of a cycle of electrons motion. Thus, it can be assumed that the electrons are in the adiabatic equilibrium of their ground state with respect to the position of the nuclei at all times. This approximation will separate the electronic and nuclear coordinates in the many-body wavefunction and simplify the problem with the solution of the dynamics of the electrons in a frozen configuration of the nuclei.

As a result, the equation 2.2 is reduced:

$$H = \sum_i \frac{\mathrm{p}_i^2}{2\mathrm{m}} + \frac{1}{2}\sum_{i\neq j}\frac{\mathrm{e}^2}{\left|\mathbf{r}_i - \mathbf{r}_j\right|} - \sum_{i,j}\frac{\mathrm{e}^2 Z_j}{\left|\mathbf{r}_i - \mathbf{R}_j\right|}. \tag{2.3}$$

Although the system is simplified, it is impossible to solve the eq. 2.3. The further simplifications should be introduced. For instance, the Density Functional Theory (DFT) method could be employed to model the interactions between electrons. The pseudopotential theory could be employed to deal with electron-ion interactions.

2.1.2 Hohenberg-Kohn theorem

In 1964, the DFT was made possible by the existence of two ingeniously simple theorems. Hohenberg and Kohn put forward and proven the theorems on firmer mathematical grounds [2.4].

The first theorem: for any system of interacting particles in an external potential $V_{ext}(\mathbf{r})$, the density is uniquely determined. In other words, the external potential is a unique functional of the electronic density (Fig.2-1). It can be written as:

$$V_{ext}(\mathbf{r}) \Leftrightarrow \rho(\mathbf{r}) \quad (2.4)$$

$V_{ext}(\mathbf{r})$ will fix the Hamiltonian operator H. And then, the ground state wavefunction Ψ is a unique functional of density $\rho(\mathbf{r})$. Therefore, all material properties of the system can be calculated if system $\rho(\mathbf{r})$ is known. This theorem was proved by Hohenberg and Kohn. It was generalized to include systems with degenerate states by Levy in 1979 [2.5].

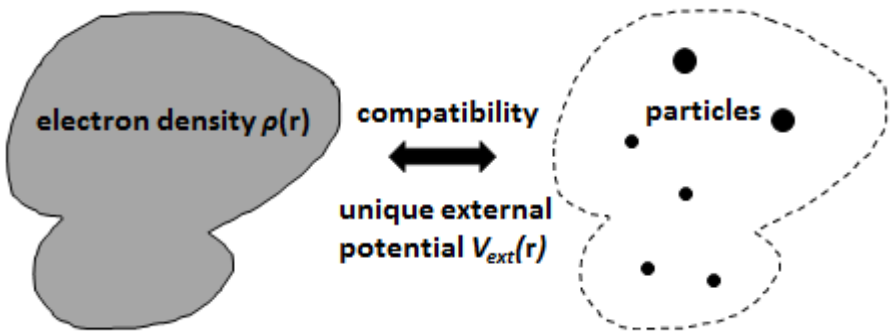

Fig. 2-1 Pictorial representation of the first Hohenberg–Kohn theorem [2.6].

The second theorem: a universal functional for the energy $E[\rho(\mathbf{r})]$ can be defined in

terms of the density $\rho(\mathbf{r})$. The exact ground state E_0 is the global minimum value of this functional E [$\rho(\mathbf{r})$]. Since the external potential $V_{ext}(\mathbf{r})$ is uniquely determined by the density $\rho(\mathbf{r})$ and since the potential in turn uniquely determines the ground state wavefunction. All the other observables of the system such as kinetic energy are uniquely determined. Then one may write the energy E [$\rho(\mathbf{r})$] as a functional of the density $\rho(\mathbf{r})$. It can be written as follows:

$$E_0 \leq E\left[\rho(\mathbf{r})\right] = F\left[\rho(\mathbf{r})\right] + \int V_{ext}(\mathbf{r})\rho(\mathbf{r})\, d\mathbf{r}\,. \qquad (2.5)$$

In eq. 2.5, a system comprises nuclei and electrons. Coulombic attraction between electron and nuclei is the external potential $V_{ext}(\mathbf{r})$ and F [$\rho(\mathbf{r})$] is the sum of the kinetic energy and the electron-electron coulombic exchange and correlation energies.

At the same time, it is already known as follow:

$$\int \rho(\mathbf{r})\, d\mathbf{r} = N\,. \qquad (2.6)$$

The two theorems give us the fundamental expression of density functional theory is:

$$\delta\left\{E\left[\rho(\mathbf{r})\right] - \mu\left(\int \rho(\mathbf{r})\, d\mathbf{r} - N\right)\right\} = . \qquad (2.7)$$

Here μ represents the electronic chemical potential:

$$\mu = \frac{\delta E\left[\rho(\mathbf{r})\right]}{\delta\rho(\mathbf{r})} = V_{ext}(\mathbf{r}) + \frac{\delta F\left[\rho(\mathbf{r})\right]}{\delta\rho(\mathbf{r})}\,. \qquad (2.8)$$

On the basis of the eq. 2.8, the electronic structure can be calculated if the F [$\rho(\mathbf{r})$] is known. However, it is still impossible to solve the Schrödinger equation. The difficulties in the calculation of the kinetic and electron-electron terms remain in Hamiltonian. After the joint efforts of Kohn and Sham, the density functional theory became workable in 1965 [2.7].

2.1.3 Kohn-Sham equations

In the Hohenberg–Kohn theorem the functional F [ρ(**r**)] can be divided into specific components:

$$F\left[\rho(\mathbf{r})\right]=T\left[\rho(\mathbf{r})\right]+J\left[\rho(\mathbf{r})\right]+E_{xc}\left[\rho(\mathbf{r})\right]. \qquad (2.9)$$

T [ρ(***r***)] refers to the kinetic energy. J [ρ(**r**)] is the classical electron-electron repulsion and E_{xc} [ρ(**r**)] is the non-classical part according to the self-interaction corrections exchange and electron correlation effects. The J [ρ(**r**)] is known that Hartree energy already can be calculated. The other parts remained unsolved until Kohn-Sham method is introduced [2.7].

In the Kohn-Sham (KS) method, the interacting electrons in the real system were replaced by the non-interacting electrons in a fictitious system that has the same density and moving in an effective potential V_{eff}. The Kohn-Sham orbitals (φ_i) could be postulated from V_{eff}. The electron density resulting from the summation of the moduli of the squared orbitals φ_i exactly equals the ground state density of the real system with interacting electrons:

$$\rho(\mathbf{r})=\sum_{i=1}^{N}|\phi_i|^2=\rho_0(\mathbf{r}), \qquad (2.10)$$

In the Kohn-Sham system, the true kinetic energy T [ρ(**r**)] of non-interacting fermions can be calculated based on the orbitals φ_i:

$$T_{KS}[\rho]=-\frac{1}{2}\sum_{i=1}^{N}\left\langle\varphi_i\middle|\nabla^2\middle|\varphi_i\right\rangle, \qquad (2.11)$$

The T_{KS} describes a main part of the true kinetic energy T [ρ(**r**)]. The method of finding the best kinetic energy for the system is similar to that of the Hartree-Fock theory. A set of orthogonal orbital is obtained via a self-consistent field to achieve the lowest energy for the system.

The Kohn-Sham equation:

$$\hat{h}_{KS}\,\varphi_i=\varepsilon_i\varphi_i, \qquad (2.12)$$

$$\hat{h}_{KS}=-\frac{1}{2}\nabla^2+\sum_i\frac{e^2Z_i}{|\mathbf{r}-\mathbf{R}_i|}+\int\frac{\rho(\mathbf{r}')}{|\mathbf{r}-\mathbf{r}'|}d\mathbf{r}'+V_{xc}(\mathbf{r}), \qquad (2.13)$$

Final term $V_{xc}(\mathbf{r})$ is the exchange correlation potential which is the functional derivative of the exchange correlation functional:

$$V_{xc}(\mathbf{r}) = \frac{\delta E_{xc}[\rho(\mathbf{r})]}{\delta \rho(\mathbf{r})}, \qquad (2.14)$$

The KS equation can be solved iteratively by assuming an initial density from the equation since the KS operator depends on the orbital φ_i of the solution. Based on the initial density, the effective potential V_{eff} can be calculated and the KS equation can be solved with the result of a new electron density. From this new electron density an updated effective potential is obtained. The iterative process is repeated until the new electron density is equal to the previous one (Fig. 2-2). Until now, the last unsolved problem is the approximation of the exchange correlation functional.

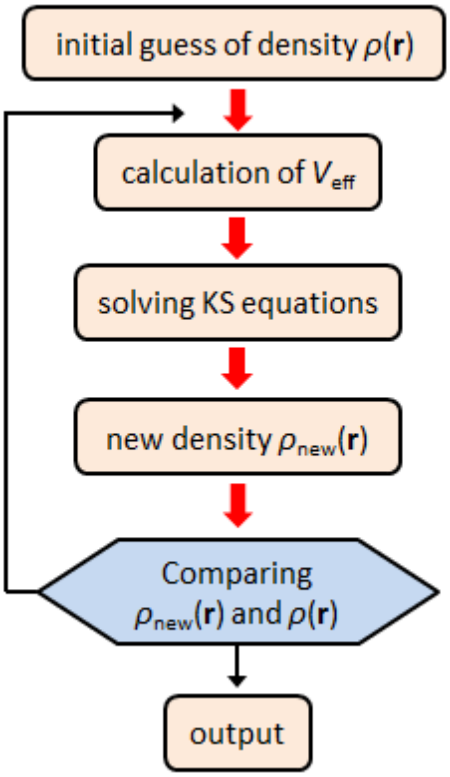

Fig. 2-2 The self-consistency cycle for Kohn–Sham DFT.

2.2 Exchange-Correlation functional

In the Kohn-Sham formalism, it provides an exact treatment of most contributions to the electronic energy including the major fraction of the kinetic energy. Up to this moment, the DFT theory is still exact and does not contains any approximations. All remaining uncertainty about the universal functional F [$\rho(\mathbf{r})$] are the no-classical exchange-correlation functional $E_{xc}[\rho(\mathbf{r})]$. The exchange effects are due to the Pauli Exclusion Principle and it is substantially larger than the correlation effect.

Approximation will be introduced to generate the non-classical exchange-correlation functional $E_{xc}[\rho(\mathbf{r})]$. It will lead to a large and rapidly expanding field of research. Many different functionals have been proposed. There are two most important approximations, including the local density approximation (LDA) and the generalized gradient approximation (GGA).

2.2.1 Local Density Approximation (LDA)

Local density approximation is the most commonly used and successful approximation formulated by Kohn and Sham in 1965.

In the local density approximation (LDA), the value of E_{xc} is approximated by the exchange-correlation energy of an electron in a homogeneous electron gas of the same density and same spin polarization, which is known as jellium [2.8]. As a result, the local exchange correlation energy is described as a function of the local charge density ε_{xc}. It can be written as follows:

$$E_{\mathrm{XC}}^{\mathrm{LDA}}\left[\rho(\mathbf{r})\right]=\int \rho(\mathbf{r})\varepsilon_{xc}\left(\rho(\mathbf{r})\right)d\mathbf{r}\cdot \qquad (2.15)$$

The ρ is the electronic density. The ε_{xc} is a functional representing the exchange-correlation energy at point **r** of a uniform electron gas as displayed in Ref. 2.9.

In the case of the systems with slowly varying charge densities, the LDA is often offering very good results which are surprisingly accurate. Because the correlation effects are well accounted in the LDA, the LDA-DFT has a higher accuracy than the methods such as Hartree-Fock method. Many experimentally relevant physical properties can be determined to a useful level of accuracy. However, the LDA becomes a poor approximation when the density varies quickly. The failings of the LDA are now well understood. The reason is that it has a tendency to favor more homogeneous systems and over-binds molecules and solids. In weakly bonded systems these errors are exaggerated and bond lengths are too short [2.10]. The accuracy can be improved by taking the gradient of the local density approximation. This modification is referred to as the generalized gradient approximation (GGA).

2.2.2 Generalized Gradient Approximation (GGA)

We have known that the exchange-correlation energy E_{xc} is a functional of the spin densities and depend on the value of spin densities in the whole space and not only at the integration point **r** as LDA. The LDA was improved by the generalized gradient approximation (GGA) technique considering the system as a non-uniform electron gas and taking account of non-local electron effects in the functional by incorporating a dependence of E_{xc} on the gradients of the spin densities [2.11, 2.12]. It can be written as follows:

$$E_{\mathrm{xc}}^{\mathrm{GGA}}\left[\rho(\boldsymbol{r})\right]=\int f_{xc}\left(\rho(\boldsymbol{r}),\left|\nabla\rho(\boldsymbol{r})\right|\right)d\boldsymbol{r}\,. \qquad (2.16)$$

In fact, the GGA is still local. Both the density and the gradients are only evaluated at the integration point **r**. Many different types of GGA have been developed for better approximations [2.13-2.15].

In general, GGA can provide a more accuracy description of the energy and the structure compared to LDA. It is more suitable for the investigation of an opened electron system. The calculation results of GGA have the many advantages over that of

LDA. For example, GGA can well describe the ground state of the light atom, molecular, cluster and the hydrocarbon. It is more accuracy for the properties of the transition metal 3*d* orbitals. In the case of the lattice constant, GGA usually overestimates the lattice constant. The LDA underestimates it conversely.

In this thesis, the GGA method [2.12] will be carried out for the theoretical investigation.

2.3 Plane-waves

To solve the difficulty of handling the infinite number of non-interacting electrons in the static potential of an infinite number of nuclei in a solid material, the electronic structures in periodic condensed matter system are discussed. According to the Bloch theorem, the solution of the Kohn–Sham equations for a periodic system can be expanded in plane waves.

According to the Bloch's theorem [2.16], the mono-electronic wavefunction in a periodic boundary condition can be described by:

$$\psi_k(\mathbf{r}) = e^{ik\cdot\mathbf{r}} u_k(\mathbf{r}). \qquad (2.17)$$

Here $e^{ik\,\mathbf{r}}$ is the phase factor. The **r** is the position and *k* is the wave vector. For any lattice vector **a**, it can be given by:

$$\psi_k(\mathbf{r}+\mathbf{a}) = e^{ik\cdot\mathbf{a}} \psi_k(\mathbf{r}). \qquad (2.18)$$

Because the u (**r**) has lattice periodicity, it can be given by:

$$u(\mathbf{r}+\mathbf{a}) = (u)\mathbf{r}. \qquad (2.19)$$

The plane-wave is perfectly periodic and submitting the Bloch's theorem. The periodic function $u(\mathbf{r})$ could be unfolded in a Fourier form:

$$u_i(\mathbf{r}) = \sum_G c_{i,G} e^{iG\cdot\mathbf{r}}. \qquad (2.20)$$

Here *G* is the reciprocal lattice vectors. Hence, the electronic wavefunction is given:

$$\psi_{i.k}(\mathbf{r}) = \sum_{G} c_{i,k+G} e^{i(k+G)\cdot\mathbf{r}} . \qquad (2.21)$$

From eq. 2.21 it is known that any wavefunction with index *k+G* is equal to the wavefunction with index *k*. And *k* is restricted to the first Brillouin zone [2.17] in the reciprocal space. Integration of *k* points on a regular grid will be performed.

The *k* point number needed in the unit cell is an important convergence parameter. As mentioned previously, it is required to use a finite number to sample the Brillouin zone in practical calculations. This means the calculating work is infinite. Fortunately, in general only a small *k* point number is required to calculate the wavefunctions because the wavefunctions and other properties such as Hamiltonian eigenvalues are smooth in the Brillouin zone. Development of choosing the *k* point efficiently has become important research works.

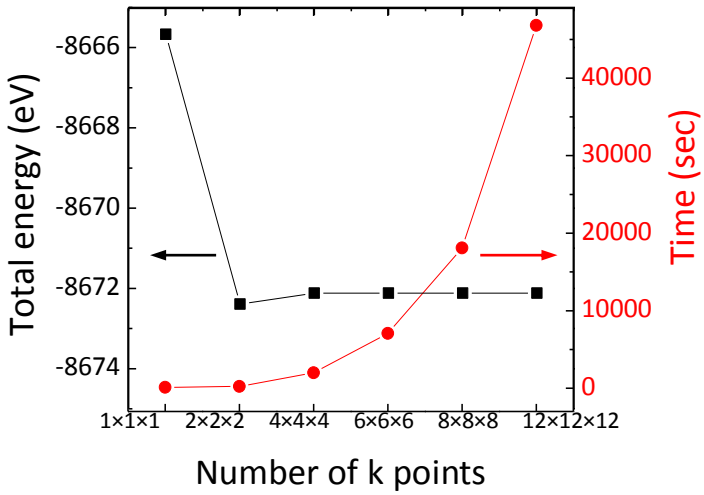

Fig. 2-3 Convergence test of the k-point sampling grid.

The Monkhorst-Pack grid [2.18] is developed for this. It is an unbiased method of choosing a set of *k* points for sampling the Brillouin zone. In fractional coordinates, it is a rectangular grid of points, which spaced evenly throughout the Brillouin zone. The sampling will be more accurate as a result of the enlarging of the grid. The required size of the grid depends on the system. The appropriate grid size can be established by means of a convergence test. For example, it shows us the dependence of the total

energy and the consumed time on the number of the k points in Fig. 2-3. The test model is a 1×1×1 unit cell of the cubic zirconia. The unit cell contains 12 atoms in total. According to the results, the 4×4×4 k point grid is enough for the unit cell since the difference is smaller than 0.01 eV. All of the calculations in this thesis are based on this convergence criteria.

The energy cut-off of plane waves is an important convergence parameter in the work. In the case of the higher cut-off energy, more plane waves will be included in the summation. Hence, it will lead to a better representation of the wavefunction. Meanwhile, a larger computation is required for higher cut-off energy. Appropriate cut-off energy for the basis set should be chosen efficiently. It is done by means of a convergence test. A series of calculations are performed under different cut-off energy.

The test is based on the 1×1×1 unit cell of cubic zirconia. It shows the total energy and calculating time determined by the cut-off energies in Fig. 2-4. On the basis of the balance between calculation accuracy and the computational capability, the cut-off energy of 60 Ry is chosen. The 60 Ry will be employed all through this thesis. Both the k point number and cut-off energy are key computational parameters because they determine the calculation time. Correctly selecting these parameters in the study will lead to satisfied high cost performance.

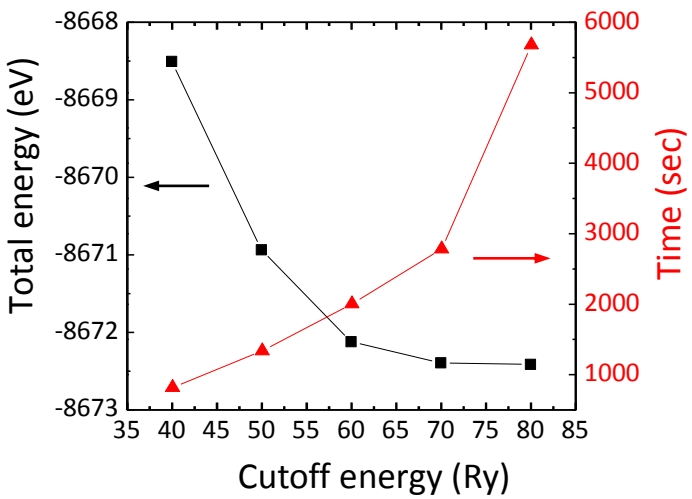

Fig. 2-4 Convergence test of the cut-off energy.

A tremendous amount of plane waves are required to reproduce the wavefunction in the region close to the atomic nuclei. The reasons are the rapid oscillations of the wavefunction caused by the steep ionic potential. It becomes extremely complicated as the system contains both the valence and core electrons. To solve this problem, pseudopotential method [2.19] is introduced to ignore the core electron effects and concentrate on the valence electrons.

2.4 Pseudopotentials

The Kohn-Sham equations have become tractable since the plane waves are used to expand the electron wavefunctions. However, it is still prohibitively expensive to use a plane wave basis set. The reason is that the all-electron calculations not only contain both core and valence electrons, but also coexist with the full Coulombic potential of the nuclei.

Physical properties of the solid are mostly depending on the valence electrons compared to the core electrons. In the pseudopotential approximation, the interactions between the atoms are only described by the valence electrons. The effects of the core electrons are described by the pseudopotential for each atomic species. Coulomb potential of the nucleus and the effect of the tightly bound core electrons are replaced by an effective ionic potential. The ionic potential only acts on the valence electrons [2.20, 2.21].

The pseudopotentials are deduced from the all-electron calculations to have the same energy levels for their wavefunctions. The valence electron pseudopotential is required to reproduce the behavior and properties of the valence electrons in the full calculation. The pseudo-wavefunctions corresponding to this modified potential do not exhibit the rapid oscillations as same as the true wavefunctions. And the number of basis set required in the calculation can be dramatically reduced without substantial

loss of any accuracy in the valence shell electrons [2.22].

It shows a schematic illustration of all-electron potential and the corresponding pseudopotential [2.23] in Fig. 2-5. Here Ψ is the wavefunction and V is the potential. It can be seen that the pseudo wavefunction has no radial nodes within the core region. At the same time the pseudo wavefunctions and potential agree with the true wavefunction and potential outside the certain cut-off radius $\mathbf{r}_c$.

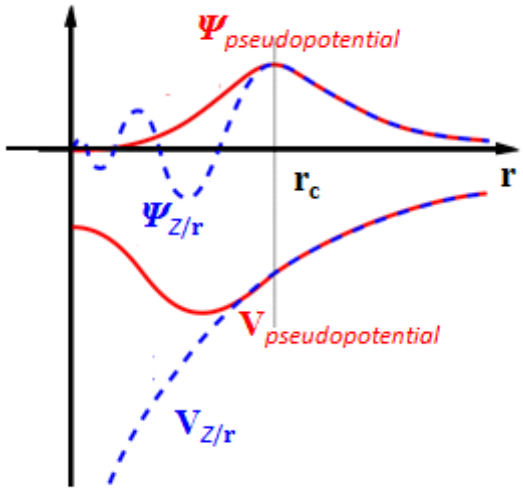

Fig. 2-5 Comparison of the real wavefunction in the potential (blue dashed lines) to the one in the pseudopotential (red solid lines).

Pseudopotentials are usually generated from all-electron calculations by self-consistently solving the all-electron Schrödinger equation. The results of valence eigenvalues are then substituted back into the Schrödinger equation along with the parameterized pseudo wavefunction. If both the pseudo wavefunction and all-electron wavefunction are normalized to one, then the norm-conservation constraint is automatically satisfied. The pseudopotential does not need to be unique but has to obey certain criteria. Firstly, the pseudo wavefunction must be the same as the all-electron wavefunction outside the cut-off radius. Secondly, the pseudo wavefunctions must be continuous at the cut-off radius. Thirdly, the valence all-electron and pseudopotential eigenvalues must be equal.

The utilizing of the pseudopotentials will simplify the computational works. The total energy of the valence electron system is much smaller than the all-electron system. Only a few plane waves used to expand the wavefunction and the relative high accuracy is maintained.

If the real and pseudo wavefunctions generate the same charge density outside the core, the pseudopotentials are norm-conserving [2.24]. This condition of norm-conservation is not possible to construct a pseudo wavefunction significantly smoother than the all-electron wavefunction in certain cases. It means the norm-conserving pseudopotentials still need many plane waves to describe the atoms with well-localized electrons. For examples, the atoms with strongly oscillating pseudo-wavefunctions such as first-row elements, elements with 3*d* and 4*f* valence electrons will produce hard pseudopotentials [2.25]. The high cut-off is required even if one atom is hard. This translates into large CPU and RAM requirements. Ultrasoft (Vanderbilt) pseudopotentials (USPP) are devised to overcome such a problem.

To relax the norm conservation condition, Vanderbilt [2.22] ultrasoft potentials (1990) were developed. It will allow smoother wavefunctions and lower cut-off energies. In the USPP method the constraint of norm-conservation is removed. Augmentation charges are introduced to compensate the resulting charge deficit. Even for the difficult cases of 2p and 3d elements, the scheme requires no more than 50-100 plane waves per atom to construct the ultrasoft pseudopotentials. According to these advantages, USPP allows the use of much smaller plane wave basis in many cases [2.24]. USPP approach is now adopted quite widely. But the success of the method is partly hampered by the difficult construction of the pseudopotentials. For example, too many parameters must be chosen and therefore extensive tests are required in order to obtain an accurate pseudopotential.

In this thesis, the USPP method [2.22] will be employed for the theoretical investigation.

2.5 Calculating procedures

In this study, the Density-functional theory calculations were performed using the periodic supercell plane-wave basis approach, as implemented in Advance/PHASE.

It shows us the processing procedure of the Advance/PHASE in Fig. 2-6. Here, the PHASE is the program of DFT software. The charge density could be calculated in the PHASE program after the input of the parameter. The ekcal is the program designed to calculate the density of states and the band structure. The CIAO is the program to generate the pseudopotentials.

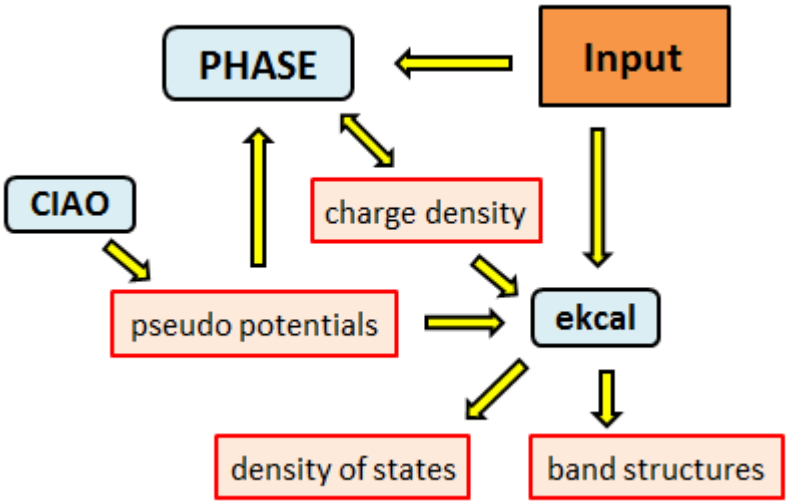

Fig.2-6 Processing procedure of the first principles calculation program

The flow chart in Fig.2-7 shows us the whole procedure of theoretical investigation employed in this study. In the first step, it will start from the bulk structures of the zirconia. Lattice constant of the zirconia will be investigated by a series of calculations in this step. Secondly, on the basis of the equilibrium lattice constant, the zirconia (111) surface models will be created to simulate the corresponding substrates. In order to match reality more exactly, the relaxation of surface structures will be carried out under certain convergence criteria. The optimized surface structure will be appropriate

for the subsequent investigation of the adsorption energies. In the third step, the adsorption of a nitrogen and indium atoms on the optimized (111) surfaces will be investigated to characterize the initial stage of the InN growth on the zirconia substrates. On the basis of the calculated adsorption energies, it will enable us to estimate the epitaxial relationship between the InN film and the substrates. The mechanism of the adatom adsorbed on the zirconia surface will be discussed. In the meantime, analysis of the density of states (DOS) will be carried out for a better understanding of the results. In the last step, on the basis of the adsorption energy at the initial stage, the hetero interface structure will be constructed and investigated. The polarity determination of the InN on the substrate will be discussed. At the same time, the DOS will also be employed to help us gain further insight into the results. Finally, the growth mechanism of InN on zirconia surfaces will be summarized on the basis of the results.

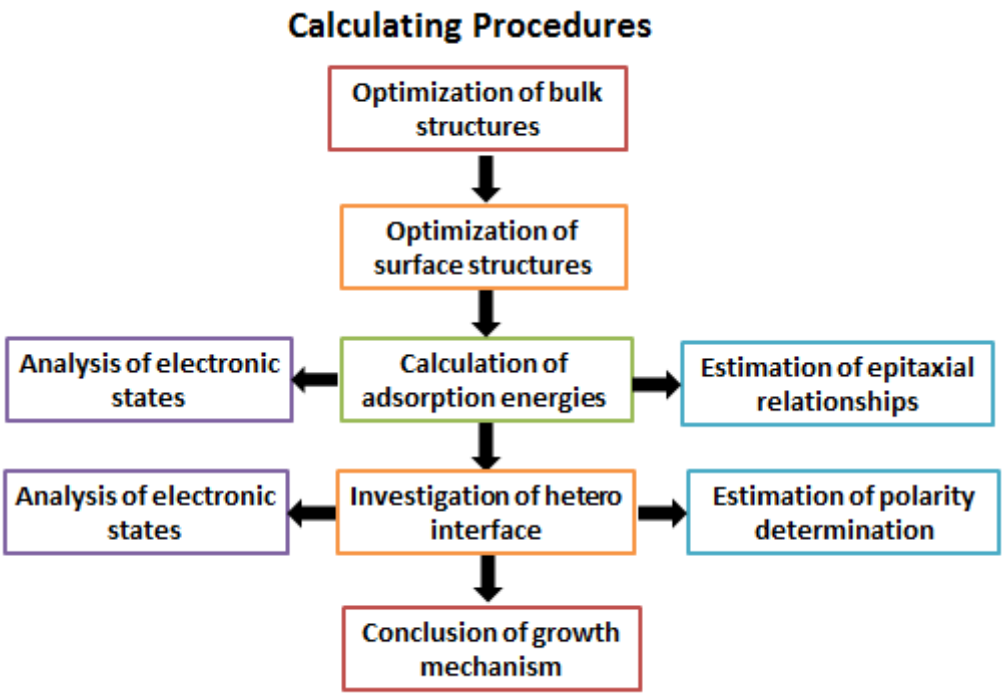

Fig 2-7 Calculating procedure of the theoretical investigation.

Reference

[2.1] D. R. Hartree, Proc. Cambridge. Philos. Soc. **24**, 89 (1928).

[2.2] V. Fock, Z. Phys. **61**, 126 (1930).

[2.3] M. Born e and J. R. Oppenheimer, Annalen der Physik **84**, 457 (1927).

[2.4] Kohn, Phys. Rev. B, **136**, 864 (1964).

[2.5] M. Levy, Proc. Nati. Acad. Sd. USA 76 **(12**), 6062 (1979).

[2.6] P. Geerlings and F. De Proft, Phys. Chem. Phys. **10**, 3028 (2008).

[2.7] W. Kohn and L. J. Sham, Phys. Rev. **140**, 1133 (1965).

[2.8] J. P. Perdew and A. Zunger, Phys. Rev. B **23**, 5048 (1981).

[2.9] W. Koch and M. C. Holthausen, A Chemist's Guide to Density Functional Theory Wiley-Vch, Weinheim, Germany, second edition, (2000).

[2.10] X. Xia, Computational Modelling Study of Yttria-stabilized Zirconia (2010).

[2.11] J. P. Perdew, J. A. Chevary, S. H. Vosko, K. A. Jackson, M. R. Pederson, D. J. Singh and C. Fiolhais, Phys. Rev. B **46**, 6671 (1992).

[2.12] J. P. Perdew, K. Burke and M. Ernzerhof, Phys. Rev. Lett. **77**, 3865 (1996).

[2.13] A. D. Becke, Phys. Rev. A **38**, 3098 (1988).

[2.14] J. P. Perdew and Y. Wang, Phys. Rev. B **45**, 13244 (1992).

[2.15] Chevary, S. H. Vosko and K. A. Jackson, Phys. Rev. B **46**, 6671 (1992).

[2.16] F. Bloch, Z. Phys. **52**, 555 (1928).

[2.17] L. P. Bouckaert, R. Smoluchowski and E. Wigner, Phys. Rev. **50**, 58 (1936).

[2.18] H. J. Monkhorst and J. D. Pack, Phys. Rev. B **13**, 5188 (1976).

[2.19] J. C. Philips, L. Kleinman, Phys. Rev. **136**, 287 (1959).

[2.20] M. L. Cohen and V. Heine, Solid State Physics, **24**, 1 (1970).

[2.21] M. T. Yin and M. L. Cohen, Phys. Rev. B **25**, 7403 (1982).

[2.22] D. Vanderbilt, Phys. Rev. B **41**, 7892 (1990).

[2.23] H. Hellmann, J. Chem. Phys. **3**, 61 (1935).

[2.24] L. Kleinmann and D. M. Bylander, Phys. Rev. Lett. **48**, 1425 (1982).

[2.25] G. Kresse, Pseudopotentials (Part II) and PAW.

Chapter 3 Initial stage of InN growth on YSZ (111) substrates

3.1 Zirconia

Zirconia is rarely found in minerals as a cubic structure, but can be prepared by several synthetic techniques. Pure zirconia exists in the monoclinic structure at the temperature below 1440 K. The monoclinic structure will convert to the tetragonal structure as the temperature increased. The tetragonal structure will turn into cubic phase when the temperature reaches to 2640 K. It shows us the atomic structures of the monoclinic, tetragonal and cubic zirconia in Fig. 3-1. The pressure-temperature phase transition diagram of the pure zirconia is shown in Fig. 3-2. Several high-pressure orthorhombic forms have also been found in the picture.

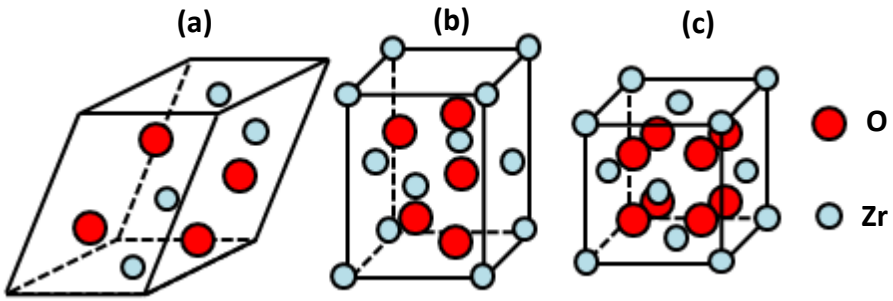

Fig. 3-1 Structure of zirconia: (a) monoclinic, (b) tetragonal and (c) cubic

The lattice size will be changed with the phase transformation. As a result, the large volume expansion of 3-5% on cooling will cause the extensive cracking in the material. This behavior destroys the mechanical properties of fabricated components during cooling and makes pure zirconia useless for any structural or mechanical application. In

order to manufacture the cubic zirconia components, it is necessary to 'lock' the material into the cubic phase wholly or partially by the use of additives or stabilizing agents. In fact, the cubic phase could be stabilized at the room temperature with addition of special elements. The addition of varying amounts of cubic stabilizers such as CaO, MgO, Mn_2O_3 and Y_2O_3 allows the formation of partially or fully stabilized zirconia. Stabilization of the cubic zirconia can be realized by doping with larger cations to expand the lattice or by doping with a lower valence cation to create oxygen anion vacancies, or a combination of the two effects. The lattice constant for the observed phases of zirconia are summarized in Table 3.1.

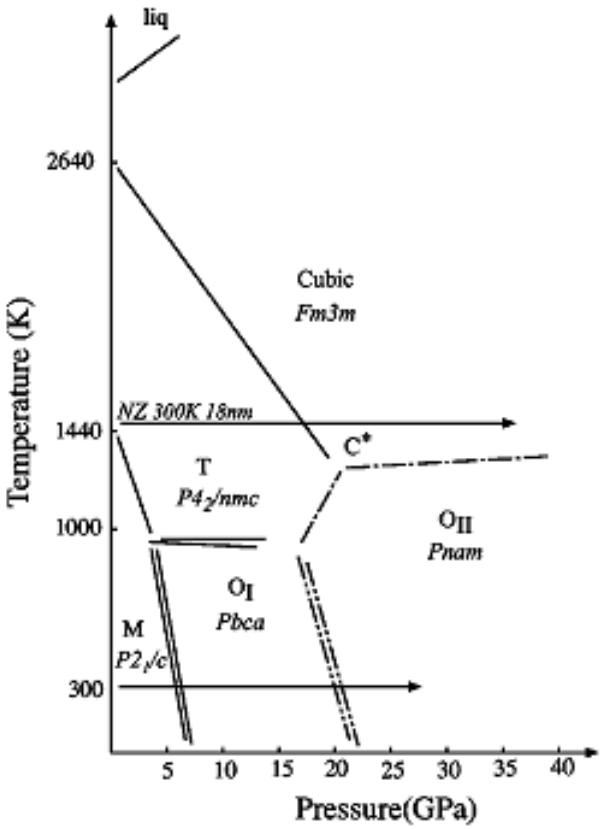

Fig. 3-2 Pressure-temperature phase diagram of zirconia. Reprinted with permission from Physical Review B. **62**, 8731 (2000). Copyright (2000) by the American Physical Society.

Table 3.1 Lattice parameters of zirconia for low pressure [3.1-3.3].

	Monoclinic	Tetragonal	Cubic
a (Å)	5.156	3.64	5.07
b (Å)	5.191	-	-
c (Å)	5.304	5.27	-
c/a	-	1.448	1
β	98.9°	90°	90°
Coordination	7	8	8
Space group	$P2_1/c$	$P4_2/nmc$	Fm3m
Density (gm/cm^3)	5.83	6.10	6.09
Reference	3.1	3.2	3.3

3.1.1 Bulk structure of Yttria-stabilized zirconia

Y_2O_3 is the most commonly used stabilizer for zirconia [3.4]. Yttria-stabilized zirconia (YSZ) has a solid solution in the cubic fluorite structure. The yttrium and zirconium are located at a face-centered-cubic cation lattice. Meanwhile, the oxygen and vacancies are located at a simple cubic anion lattice. In the cubic fluorite structure, the cation is in the center of a cube of eight anions and the oxygen ion or oxygen vacancy is in the center of a cation tetrahedron (Fig. 3-2).

YSZ is an attractive electrolyte for solid oxide fuel cell (SOFC) because it exhibits good ionic conductivity over a wide range of oxygen partial pressures. At the same time, in order to achieve sufficient ion conduction, an SOFC with the YSZ electrolyte must be operated at high temperatures (800 °C-1000 °C). YSZ has the mechanical robustness at those temperatures [3.5-3.6]. The introduction of yttria will create charge compensating oxygen vacancies. The oxygen vacancies are mobile at high temperatures and give rise to high oxygen ionic conductivity. In fact more than 99% of the current through YSZ is carried by oxide ions.

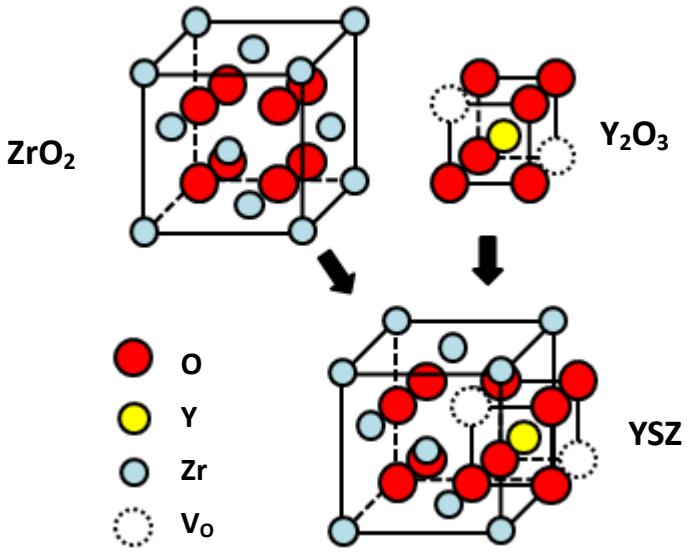

Fig. 3-2 The cubic fluorite structure of YSZ.

The YSZ crystals are fabricated by the induction skull melting technique (ISMT) [7]. The crystal is grown by directional solidification in a cold crucible. The growth is carried out in various ranges of compositions ZrO_2-Y_2O_3. The wafers were cut from the crystals. The wafer is up to 2 inches diameter.

According to previous experimental studies, various phases can be generated from the solid solution depending on the composition of Y_2O_3 (Table 3.2) [3.8-3.11]. The formation of m-ZrO2 is confined to the region under 3 mol% [3.10]. In the region of 1-8 mol%, the partially stabilized zirconia (PSZ) is produced with a tetragonal phase t'. The fully stabilized zirconia (FSZ) is shown above 8 mol%. However, it is only a cubic like t" phase around 8 mol% Y content. It cannot be distinguished from the cubic phase by XRD. The investigations of the Laser Raman spectroscopy and the electron diffraction have identified the t" phase from the cubic phase [3.9]. The cubic zirconia stabilized at 8-10 mol% Y_2O_3 is mostly employed because the highest conductivity at the concentration was found [3.11]. Mixtures of the cubic YSZ and segregated $Y_4Zr_3O_{12}$ [3.8] occur for the yttria content between 15-40 mol%. For the yttria content higher than 40 mol %, the system crystallizes only $Y_4Zr_3O_{12}$.

Table 3.2 The dependence of YSZ structure on yttria content.

	Monoclinic YSZ	Tetragonal' YSZ	Tetragonal'' YSZ	Cubic YSZ	Cubic YSZ and $Y_4Zr_3O_{12}$.	$Y_4Zr_3O_{12}$
Y_2O_3 (mol%)	0-2.5	1-8	6-10	10-20	20-40	≥40

A large number of computational [3.5, 3.12-3.14] and experimental [3.15-3.21] studies have been carried out to investigate the bulk yttrium-stabilized zirconia. These studies include the composition and ordering of bulk YSZ, the ordered ground-state structures of YSZ, the driving forces for structure stability and the direction of the atoms away from cubic fluorite sites during relaxation.

For the YSZ system, two Y^{3+} substitute for two Zr^{4+} to create one oxygen vacancy (V_O). The pair of yttrium dopants together with the charge compensating oxygen vacancy is considered as a bound defect cluster (Y-V-Y).

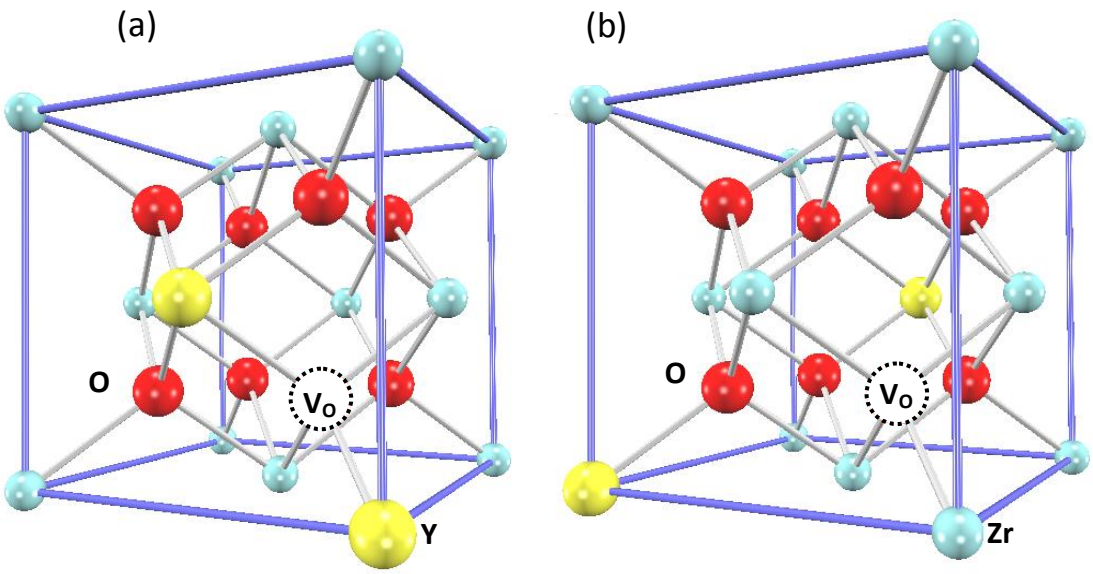

Fig. 3-3 Configurations of the Y dopants in nearest-neighbor (NN) sites or next-nearest-neighbor (NNN) sites to the oxygen vacancy.

It is found that the order of stability of the YSZ depended on the relative positions of the dopant and their charge compensating oxygen vacancies. For the charge neutral

Y-V-Y cluster, it has been found the most energetically favorable configurations are the Y dopants in nearest-neighbor (NN) sites or next-nearest-neighbor (NNN) sites to the oxygen vacancy. Some studies show that the oxygen vacancy prefers Y as its nearest neighbor (NN) [3.18-3.21]. However, several simulations and experiments indicate that oxygen vacancies tend to be located at the second nearest neighbor (NNN) position [3.16, 3.22-3.25]. There is no consistent pattern as to which configuration is most stable because the energy differences between NN and NNN configurations are within ± 0.1 eV per unit cell [3.26]. Fig. 3-3 shows us the NN and NNN sites configurations.

3.1.2 Surface structures of Yttria-stabilized zirconia

The surface structures of YSZ are less understood compared to the bulk structures. Both experimental techniques and computational simulations have been applied to investigate surface structure and properties of zirconia.

In the case of experimental studies, the YSZ surfaces have been examined by Auger, photoelectron, vibrational spectroscopy, high resolution transition electron microscopy (HRTEM) and X-ray diffraction. These techniques are limited because they provided indirect and incomplete information about the detailed surface atomic structure. HRTEM studies at lower temperatures (600 °C) show that YSZ appears to display small coin-like morphology with the (111) surface favored [3.27]. In monoclinic zirconia, it is found the material tends to form coin-like particles and have a strong preference for (111) and (-111) surfaces [3.27].

In the case of the computational modeling studies, the monoclinic (-111) and tetragonal (101) surfaces are predicted to be the most stable by DFT investigations [3.28]. For the pure cubic zirconia, according to the previous interatomic potential [3.26] quantum mechanical (QM), DFT [3.29] and Hartree−Fock [3.30] calculations, the (111) surfaces are predicted as the most thermodynamically stable surfaces. The results of experimental and computational morphology studies for the phases of zirconia are summarized in table 3.3.

Table 3.3 Surface stability for the phases of zirconia.

Stability	Cubic	Tetragonal	Monoclinic
Stable	(111)	(101)	(-111)
Metastable	(110) (100) (310)	(001) (111)	(111)

Previous theoretical study [3.31] also suggests that the stoichiometric oxygen (O) terminated phase is more stable than the Zr or O-O terminations, independent of the specific orientation of the surface. According this result, the O-terminated surface structure will be employed in this thesis.

3.1.3 Yttrium segregation on zirconia (111) surface

Surface segregation is a common phenomenon in multi-component materials. The segregation can dramatically influence the functionalities of materials. Both experimental and computational evidences show that Y in stabilized cubic zirconia does indeed segregate to the surface. The X-ray photoelectron spectroscopy (XPS) studies [3.32] indicate that Y/Zr ratio at the surface of the tetragonal YSZ was found to be about three times the bulk value. The segregated yttrium layer Y was estimated to be at least 50-60 Å thick. Segregation has also been confirmed by low energy ion scattering (LEIS), which indicated that there is a high enrichment of yttrium on YSZ surface monolayers. Y_2O_3 accumulates in the subsurface layer (Fig. 3-4). The surface composition is independent of Y concentration in the YSZ bulk. The Y_2O_3 concentration in the subsurface layer is about 18 and 30 mol % for the 3 and 10 mol % YSZ samples, respectively [3.33]. J. Lahiri *et al.* suggested a model system consisting of a Y-enriched surface layer and a bulk to estimate the surface Y enrichment [3.34]. They found the enrichment is either only in the first or the first two layers (Fig. 3-4). On the basis of the experimental results, the people suggest a sandwich structure model for the YSZ segregation. The model includes three regions from the top to the bottom. They are the Y-rich region, the Y-depleted region and the bulk region [3.33].

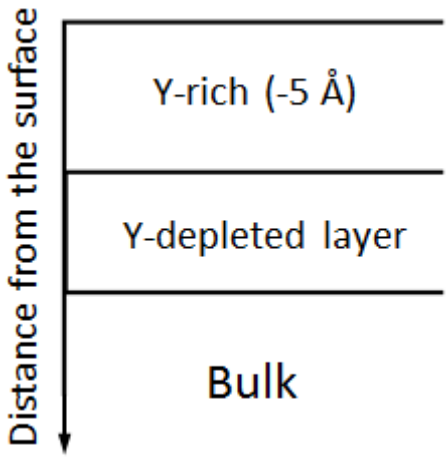

Fig. 3-4 The Sandwich structure for YSZ surface segregation.

In the theoretical study, Ballabio *et al*. [3.35] have performed DFT calculations for the (111), (110) and (100) surfaces of YSZ. They have found the presence of yttrium at the surface is crucial to reconcile theoretical study and experiment. From another theoretical investigation by Eicher *et al.* [3.32], the tetragonal YSZ (101) surface becomes more stable if the dopants are located close to the surface. There is a driving force for the Y surface segregation. It is known that the tetragonal (101) surface is equivalent to the cubic (111) surface. Stanek *et al.* [3.36] found that surface orientation dependence caused significant variation in concentration of yttrium at different surface. Therefore, the surface properties will be a function of defect concentration and distribution. Recently experimental and theoretical investigations on the surface composition of YSZ-ceramics [3.37] also suggest yttrium enrichment compared to the bulk.

Even though there have been considerable studies of yttrium segregation to the YSZ surface, our understanding is still limited. Especially the atomic structure of the YSZ (111) surface at the atomic scale is not well understood. At the same time, the oxygen vacancy and the yttrium dopant are so important since the many important properties are concerned to them. As mentioned before, in case of SOFCs, the electrical properties of YSZ are greatly affected by the oxygen vacancies and the yttrium dopants.

However, until now most studies of the YSZ surface only focus on the stability of yttrium at the zirconia (111) surface and the enrichment of the yttrium on the surface region. In particular, the dispersion and the location for both the yttrium and oxygen vacancy are still unclear. According to the limit of the current technology, it is currently difficult to get the clear description of the surface structure based on the experimental results. Further structural characterization using various techniques such as XPS, LEIS, STM and TEM can help us better understanding the atomic structure of the surface region.

In this study, based on the previous research works of YSZ surface structure, the atomic structure of YSZ (111) surface will be discussed. The computational model is required for investigation of the adsorption energy in the afterward. The model must have the similar atomic structure with the substrate to make the study believable. On the basis of both the experimental and the theoretical results, the surface model will be introduced. The detail will be explained in next section.

3.2 Experimental results of InN growth on YSZ (111)

As mentioned in chapter 1, the InN film can be epitaxially grown on the YSZ substrates by PLD. Here is the detail of the growth experiment. For the YSZ (111) substrates, it is found that the Y segregation at the surface region could be controlled by the surface treatment. According to the results of the XPS measurement, in case of the substrate with no Y segregation, Y was distributed uniformly from the surface into the bulk region of the substrate. Therefore, the Y content of the surface region for the Y-segregation free substrates is the same as the bulk region. On the other hand, in case of the Y-segregated substrate, the concentration of Y in the surface region is much higher than that in the bulk region [3.38] because of the Y enrichment at the surface region. The difference between the Y-segregated and segregation-free surfaces is the Y concentrations at the surface region.

The growth of InN films by PLD are carried out on the Y-segregation-free substrates

and the Y-segregated YSZ (111) substrates respectively. The growth temperature for Y segregation-free substrate is 550 °C. For the Y-segregated substrate it is 450 °C [3.38, 3.39].

As mentioned in chapter 1, there are the epitaxial relationships of InN [11-20] / /YSZ [1-10] and (0001) / /YSZ (111) in the InN/YSZ system [3.40]. The epitaxial relationships are independent of the Y segregation in the surface region of the substrates. Besides that, nothing is known quite well at the initial stage of the growth. Especially, the mechanism about the formation of such epitaxial relationships in the InN/YSZ system is not well understood. Presently, the experimental techniques that are applicable for the highly resistive substrates are limited. Better understanding of the film growth at the initial stage including the adsorption and migration are beneficial to the investigations of the system. Hence, theoretical study is performed to investigated the initial stage of InN on the YSZ (111) substrates in the next section.

3.3 Theoretical study of InN growth on YSZ (111)

In last section, it is known that the growth of InN at the initial stage is not well understood because the experimental techniques that are applicable for the highly resistive substrates are limited. For this reason, the fundamentally theoretical calculation could be employed to solve the problem.

As mentioned above, the first principles calculations provide us a useful tool to investigate the InN film growth on YSZ substrates at the atomic scale. In fact the theoretical study has been employed as a useful tool for characterization and simulation of the initial stage growth on various substrates [1.50-1.55]. It will help us understand the growth better. Especially, in the case of the InN/YSZ, the hetero-interface is atomically abrupt. This additional advantage enables us to characterize the interfacial structure and investigate the growth mechanism theoretically at the initial stage.

In this section, the initial stage of the InN growth on YSZ (111) substrate will be

discussed through the adsorption energies of single In and N atoms on the YSZ (111) surface, which represents the first step of the film growth.

3.3.1 Bulk structure of cubic zirconia

As mentioned before, the energy calculations and geometry optimizations were carried out in GGA [3.41] - DFT. Electron configurations of pseudopotentials [3.42] for In, N, Zr, O and Y are $4d^{10}5s^{2}5p^{1}$, $2s^{2}2p^{3}$, $4s^{2}4p^{6}4d^{2}5s^{2}$, $2s^{2}2p^{4}$ and $4s^{2}4p^{6}4d^{1}5s^{2}$ respectively. All of the calculations were performed by the Advance/PHASE package [3.43].

According to the calculating procedure, in order to construct the zirconia surface structure, the investigation of the bulk structure is required. Fig. 3-5 shows us the atomic structure of the bulk zirconia. The investigations of the equilibrium lattice constant will be carried out on the basis of the cubic zirconia structure. In detail, all the atoms in the cubic structure are fixed at the position. The structure is taken as the bulk. Then the lattice of the 1×1×1 unit cell will be changed while the cubic structure is kept. The total energy of the unit cell will be investigated to found out the energy dependence on the lattice size.

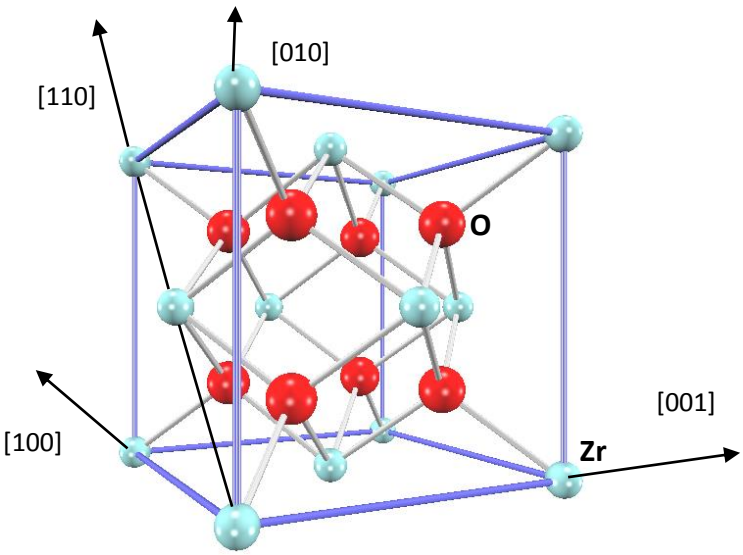

Fig. 3-5 The atomic structure of the bulk zirconia.

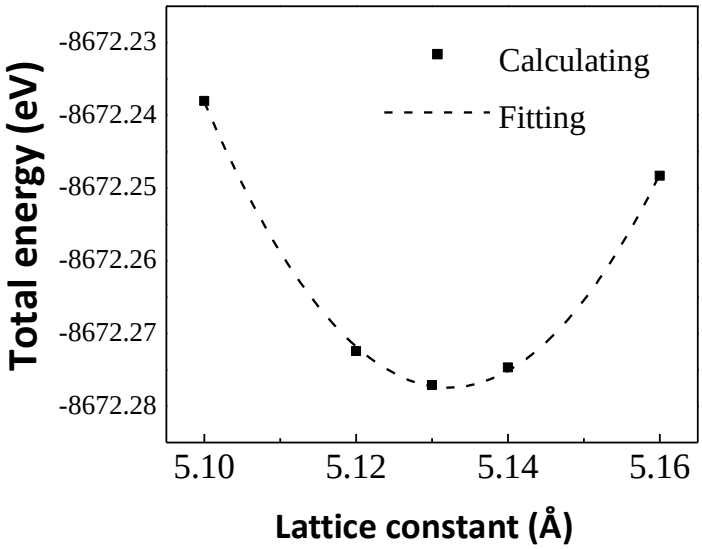

Fig. 3-6 The equilibrium lattice constant of cubic zirconia.

The results are shown in Fig. 3-6. The total energies of the cubic zirconia model depend on the lattice constant of the structure. In Fig. 3-6, the lower energy means the structure is stable. Hence, it is found that the total energy has the minimum value at the 5.13 Å. This indicates that the cubic structure is most stable at this lattice.

According to the investigations of equilibrium lattice constant, the lattice constant *a* is 5.13 Å in this theoretical study. This value is larger than the experimental one. Experimental data of 5.07 Å measured by the X-ray powder diffraction has been reported [3]. The reason is the GGA usually overestimates the lattice constant. This result of lattice is quite same to the previous reported [3.44] lattice constant based on the GGA.

The density of state (DOS) calculation for the bulk zirconia is performed and the result is shown in Fig. 3-7. It is found that the cubic zirconia is an insulator with a large bandgap 3.35 eV which is coincident with the previous calculations [3.45].

The filled O2*p* states comprised the valence band (VB) and the empty Zr4*d* states form the conduction band (CB). The absence of the Zr5s and *d*-character states in the valence bands suggests a nearly complete transfer of the Zr5*s* and 4*d* electrons to the oxygen atoms in the crystal [3.46]. The strong hybridization between Zr4*d* and O2*p* in

all the DOS indicate the covalent interaction between Zr and O ions [3.47].

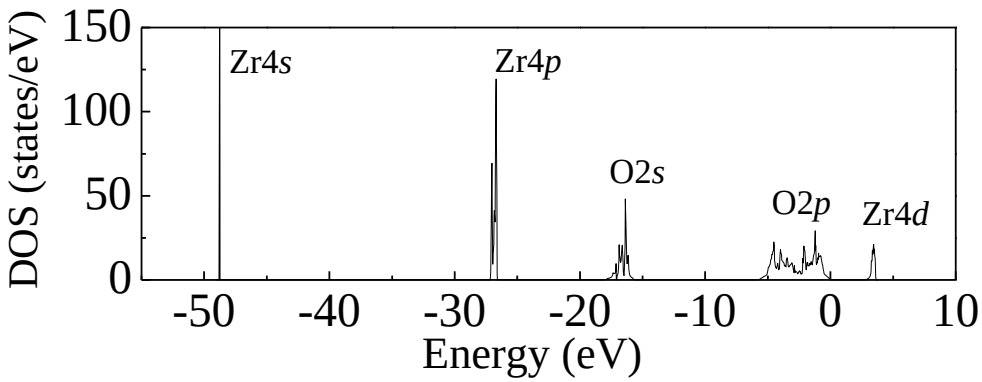

Fig. 3-7 Total DOS analysis of the bulk zirconia structure.

3.3.2 Theoretical study of the YSZ (111) surface

The equilibrium lattice constant is obtained in last section. On the basis of the equilibrium lattice constant, the structure of the (111) surface will be created by cleaving the bulk crystal along the (111) plane.

In order to perform calculations of the surfaces within a plane wave periodic framework, definition of the surface supercell is required. Since the surface is not periodic in the vertical direction, a periodic system should be defined to emulate the non-periodic system. A ``slab'' of material is introduced to solve the problem. The slab is thick enough that its surface behaves in the same way as the surface of an infinitely thick slab. In this thesis, the slab contained twelve atomic layers. A vacuum layer of 15 Å in the perpendicular direction is employed to remove the interactions between the slabs. The supercell consisted of a 2×2 array of hexagonal unit cell and contained 48 atoms in total.

It is already known that the surfaces of zirconia can be classified in non-polar and polar. In the case of the non-polar surfaces, the atomic planes contain atoms of both species maintaining charge neutrality. In the case of the polar surfaces, they can present different terminations. It shows us the side view of the cubic zirconia (111)

surfaces in Fig. 3-8. The atomic structures show repeats of the O-Zr-O trilayer in the perpendicular direction. Due to the crystallographic structure, the polar surface (111) can provide three different terminations.

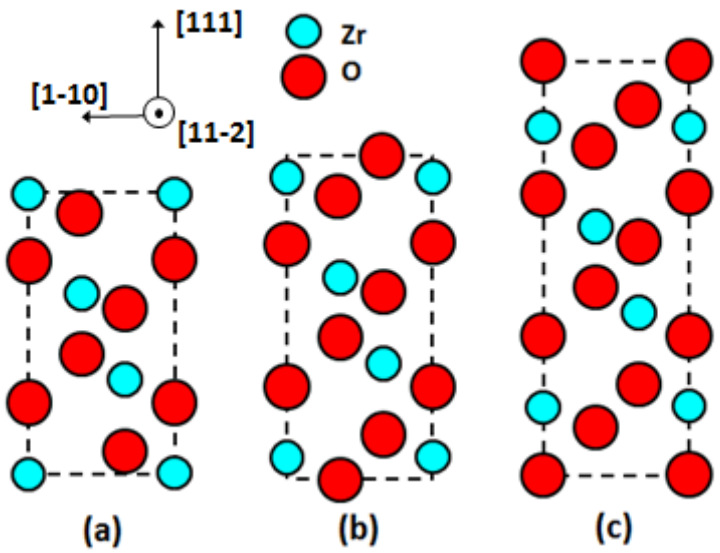

Fig. 3-8 Side view of the cubic zirconia (111) surfaces: (a) Zr-terminated, (b) O-terminated and (c) O-O terminated.

Among the terminations, only the O-terminated surface is stoichiometric. According to the previous report, the O-termination is more stable than the Zr- or O-O terminations [3.48]. Therefore, the O-terminated surface will be employed in this study.

Cleavage of the bulk crystal will create the dangling bonds on the both side of the slab models. For the simulation of the real substrate, in the supercell calculation, one side of the slab has a real surface. The other side of the slab should mimic the bulk material. If it is not properly handled, this will make the theoretical investigation deviated from the truth. Therefore, the effects of the dangling bonds at the backside need to be canceled. Saturation of the dangling bonds is one possibility to cope with this system. Other methods have also been proposed. For example, the dipole moment in the slab is canceled by symmetry or by an external field [3.49].

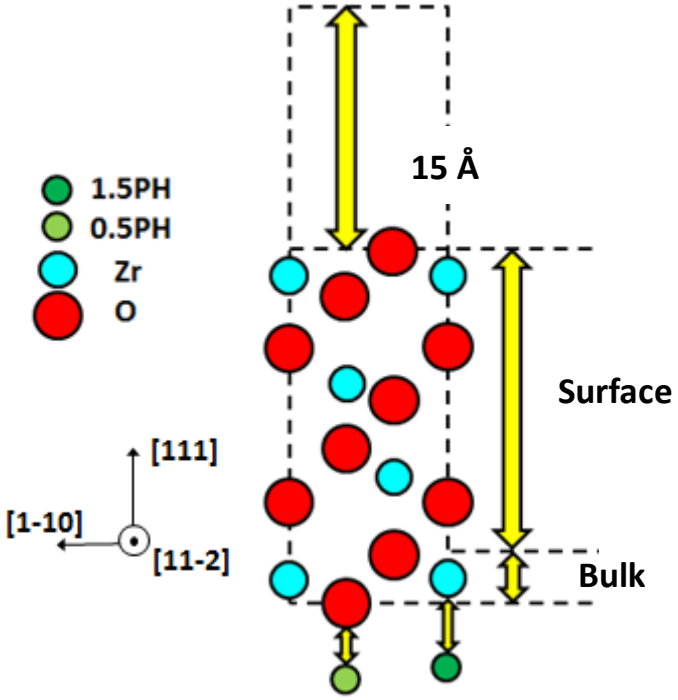

Fig. 3-9 Dangling bonds at the bottom are terminated by the PH.

In this thesis, the method of the pseudohydrogens (PH) termination is employed to saturate the dangling bonds. In this thesis, both the oxygen and zirconium atoms at the bottom of the supercell were saturated by the PH. The Zr atom is surrounded by eight oxygen atom and possessing four valence electrons. Therefore, each Zr atom contributes four eighths (1/2) to each bond. At the same time, the H needs two electrons to have a complete 1*s* shell, The Zr dangling bonds could be terminated by pseudohydrogens with charge of 1.5 e. It can be obtained from

$$Z = 2 - 1 / 2 = 3 / 2. \qquad (3.2)$$

In case of the O atom, it is surrounded by four Zr atoms and possessing six valence electrons. The most stable state for an O atom has eight electrons forming a closed shell. Therefore, pseudohydrogens with charge of 0.5e will be employed to saturate the O dangling bonds. It can be obtained from

$$Z = (8 - 6) / 4 = 1 / 2. \qquad (3.3)$$

It shows us the cross sectional view of the slab and the schematic illustration of the backside termination method in Fig. 3-9. The positions of the pseudohydrogens in the

perpendicular direction were determined by the Hellmann-Feynman forces on the atoms [3.50]. The convergence criteria of the Hellmann-Feynman forces is 1.0×10^{-3} hartree/bohr.

Table 3.3 Atomic forces (hartree/bohr) on Zr and O atoms in unterminated, backside terminated and bulk structures.

Atomic forces (hartree/bohr)	Unterminated	Terminated	Bulk
O	1.5×10^{-2}	5.0×10^{-4}	5.0×10^{-6}
Zr	1.3×10^{-2}	5.0×10^{-4}	5.0×10^{-6}

In table 3.3, it shows us the atomic forces on the Zr and O atoms in the in unterminated, backside terminated and bulk structures. By comparison, it is found that the terminations have reduced the atomic force and removed the effect of the dangling bonds. After the termination, the atoms at the bottom of the slab are more close to the one in the bulk structure. As a result, in case of the terminated slab, the top side will act as surface for the investigation. The bottom side is terminated by PH and acting as same as the bulk structure. So far, a slab model appropriate to mimic the real substrate is obtained.

For a better understanding of the electronic states of the Zr and O atoms and confirming the effect of the slab bottom termination, the local density of state (DOS) is calculated. The local DOSs of the bottom Zr and O atoms for the unterminated slab, the terminated slab, and the bulk are shown in Fig. 3-10. In Fig. 3-10 (a), it is found that the DOS of oxygen atoms in unterminated slab is different compared to those of the terminated and bulk slabs. Firstly, in case of the unterminated slab, the DOS majority locates at around -1 eV. Because the bond of surface oxygen is broken, the energy of the surface O is increased. This is the reason why the DOS of the surface O shifts compared to that of the bulk. Secondly, a new state at 5eV is found for the unterminated O. The new state is disappeared after the dangling bond termination. Therefore, it can be speculated that the new state origins from the dangling bond at

the surface. In the case of the Zr atom in Fig. 3-10 (b), the new state at 5eV is disappeared too after the dangling bond termination. On the basis of the results, it is known that the dangling bond is saturated and the electronic structure of the surface atoms becomes close to that of the bulk ones after the terminations.

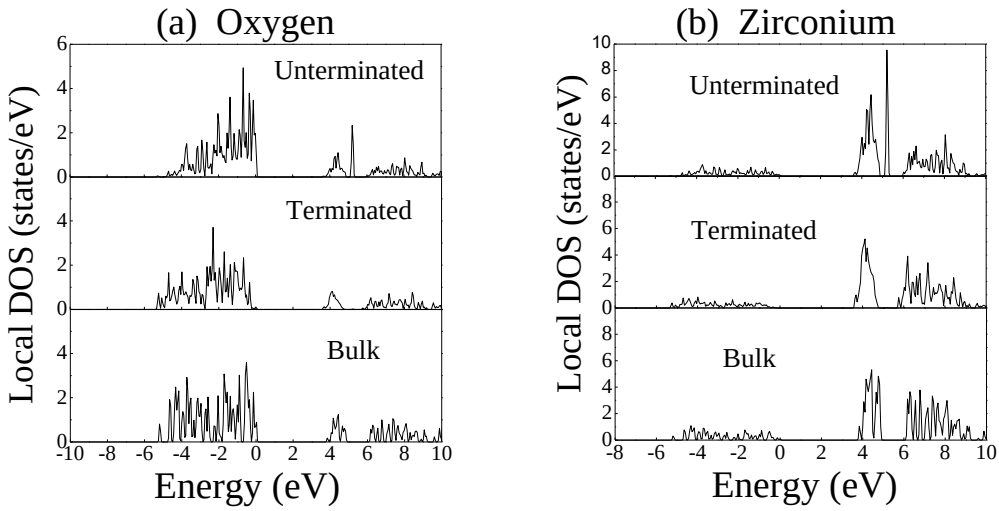

Fig. 3-10 Local DOSs of unterminated, terminated and bulk structures for (a) O atoms and (b) Zr atoms.

As mentioned before, a 2×2 array of the unit cell is employed to investigation the surface structures. The plane-wave cut-off energy was set to be 60 Ry. The Brillouin-zone integration was calculated using a 2×2×1 k-point grid, which is generated automatically by the Monkhorst-Pack method [3.51]. For the convergence criteria for the total energy calculation and surface relaxation, a self-consistent field (SCF) tolerance of 3.0×10^{-7} eV/atom and maximum force tolerance of 5.0×10^{-2} eV/Å were employed. The investigation is also performed under a denser 4×4×1 k-point grid. It is found that the energy difference between the 2×2×1 k-point grid and 4×4×1 k-point grid is less than 1 meV/atom. At the same time, the calculated adsorption energy in this thesis is about 1 eV. Therefore, the total energy difference is negligible. The 2×2×1 k-point grid for the 2×2 array supercell is enough.

As mentioned before, Y segregation at the surface region of the YSZ (111) substrates could be controlled by the surface treatment. In one case, the yttrium concentration at

the surface region is as low as the bulk. It is about 10 %mol. In the other case, the yttrium concentration at the surface region is higher than the bulk. It is about 30 %mol. For this reason, the atomic structures of the surface are totally different in the two cases. Hence, in order to ensure that the slab model is very close to the real substrate, two slab models with different surface structures will be prepared.

It shows us the two atomic structures of the (111) surface in Fig. 3-11. Fig. 3-11 (a) is the cubic zirconia (111) surface. Fig. 3-11 (b) is obtained on the basis of Fig. 3-11 (a). All the Zr atoms in the upper half of Fig. 3-11 (a) are replaced by Y atoms. The O vacancies occupied the NN sites to maintain electrical neutrality. In this thesis, these two slabs will be taken as the YSZ substrates in the subsequent investigations. Fig. 3-11 (a) is the slab model of the YSZ substrate without Y segregated in the surface region. It can be defined as segregation-free slab. Contrarily to (a), Fig. 3-11 (b) is the slab model of the YSZ substrate with Y segregated at the in the surface region. It will be called the Y-segregated slab.

The two slabs in Fig. 3-11 are quite appropriate to the imitation of the YSZ substrates. Firstly, the two slabs are created on the basis of the previous reports on the surface structure of the YSZ substrates. As mentioned before, it has been experimentally confirmed that the content of the Y at the surface region is different for the Y-segregation substrate and Y-segregation-free substrate. As to the atomic structure of the surface, the theoretical studies have been employed when the experimental characterization are limited. In case of the Y segregation, theoretical studies find that the both O vacancy and Y energetically exist on the surface region as deep as 5 Å [3.26]. This depth is just about two O-Zr-O trilayers. Therefore, the upper half Zr atoms are replaced with Y atoms to imitate the Y-segregation. Secondly, in spite of recent studies of YSZ surfaces, a detailed understanding of the surface properties at the atomic level is still lacking. In case of the Y-segregation free substrate, the location and the dispersion of the minority yttrium dopants are completely unknown. Due to this reason, for the slab model of the Y-segregation free substrate, the effects of the small quantity of Y atoms are ignored. The cubic zirconia surface is employed as the

Y-segregation free substrate. In this way the two slab models will be established according to the Y-segregation-free and Y-segregated YSZ (111) substrates.

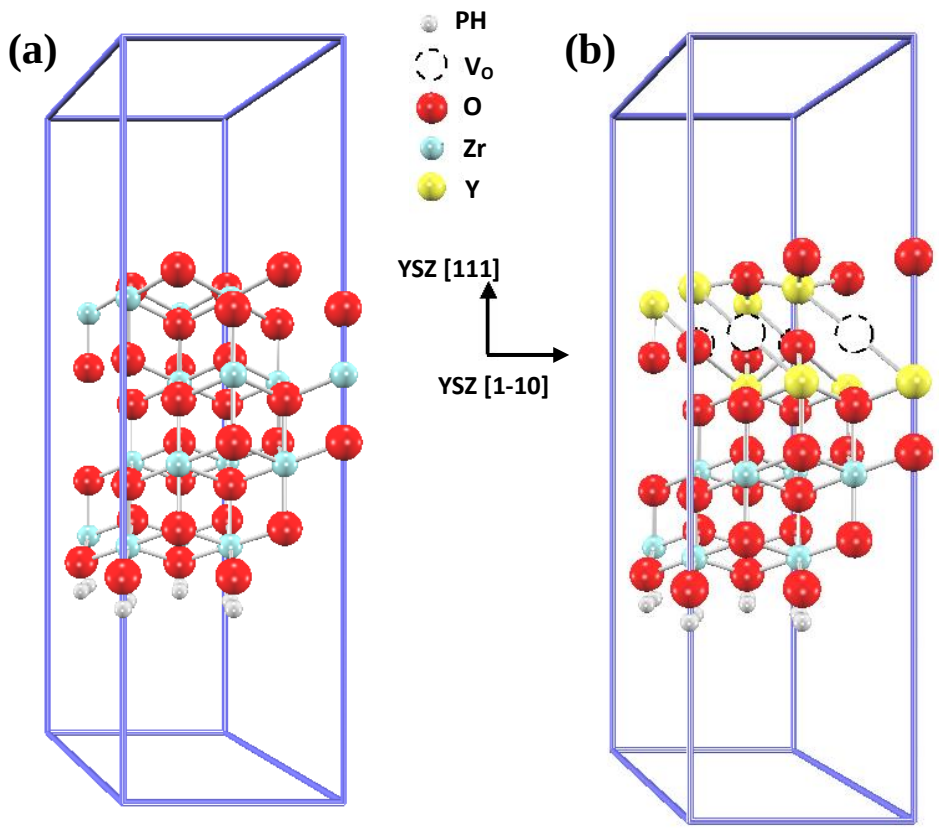

Fig. 3-11 Slab models of YSZ substrates: (a) Y-segregation-free surface, (b) Y-segregated surface.

In order to make the slab model more close to the YSZ substrates, a further optimization of surface relaxation is inherently needed. As shown in Fig. 3-9 and 3-11, in the relaxation, the five bottom layers consisting of an O-Zr-O trilayer and two pseudohydrogen layers are fixed at the bulk positions. This part of the slab will be used as the bulk substrate. Meanwhile, the top nine layers are consisted of three trilayers. This part will be treated as the surface region. The layers will be fully relaxed under the convergence criteria of 0.05eV/Å. As a result, the position of the atoms in the surface region will be changed. The surface part was not the bulk structure any more. The structure becomes more close to the surface region of the substrates.

The results of the surface relaxations are summarized in tables 3.4 and 3.5. The relaxations of interplanar distance for segregation-free slab and Y-segregated slab can be given by

$$\Delta_{i\text{-}j} = (d_{i\text{-}j} - d_{\text{bulk}})/d_{\text{bulk}}. \qquad (3.4)$$

Here $d_{i\text{-}j}$ is the distance between i-th layer and j-th layer. The d_{bulk} is the corresponding distance before relaxation in bulk structure. The definition of the in interplanar distance can be seen in Fig. 3.12 and 3.13.

Table 3.4 Interplanar relaxations $\Delta_{i\text{-}j}$ for Y-segregation free slab.

$\Delta_{1\text{-}2}$	$\Delta_{2\text{-}3}$	$\Delta_{3\text{-}4}$	$\Delta_{4\text{-}5}$	$\Delta_{5\text{-}6}$	$\Delta_{6\text{-}7}$	$\Delta_{7\text{-}8}$	$\Delta_{8\text{-}9}$	$\Delta_{9\text{-}10}$
8.5 %	1.0 %	-3.7 %	2.1 %	0.5 %	1.0 %	0.4 %	0.6 %	-0.7 %

Table 3.5 Interplanar relaxations $\Delta_{i\text{-}j}$ for Y-segregated slab.

$\Delta_{1\text{-}2}$	$\Delta_{2\text{-}3}$	$\Delta_{3\text{-}4}$	$\Delta_{4\text{-}5}$	$\Delta_{5\text{-}6}$	$\Delta_{6\text{-}7}$	$\Delta_{7\text{-}8}$	$\Delta_{8\text{-}9}$
-23.4%	-7.4%	88.1%	-6.5%	8.1%	-3.5%	1.7%	-1.7%

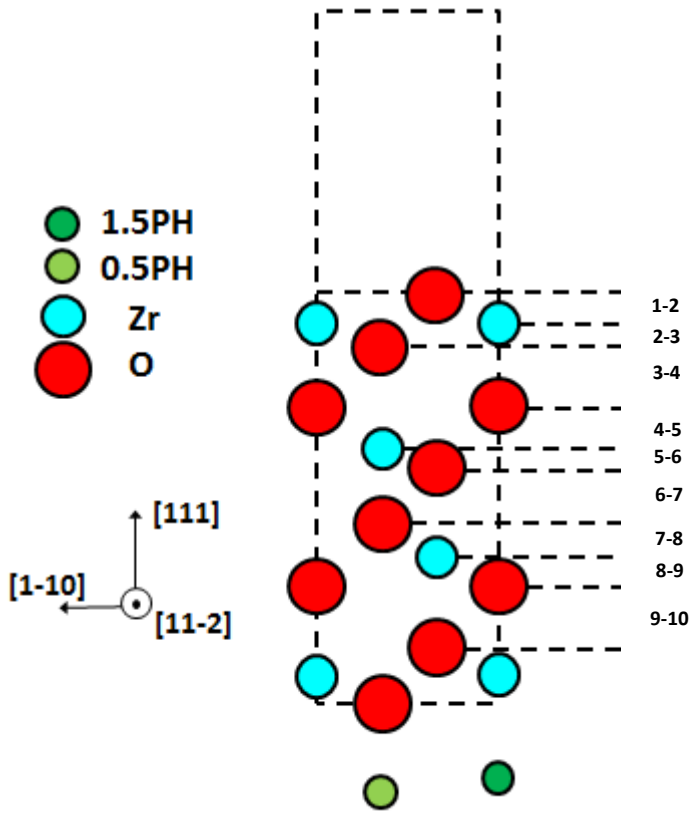

Fig. 3-12 Cross-sectional view of the segregation-free slab after relaxation.

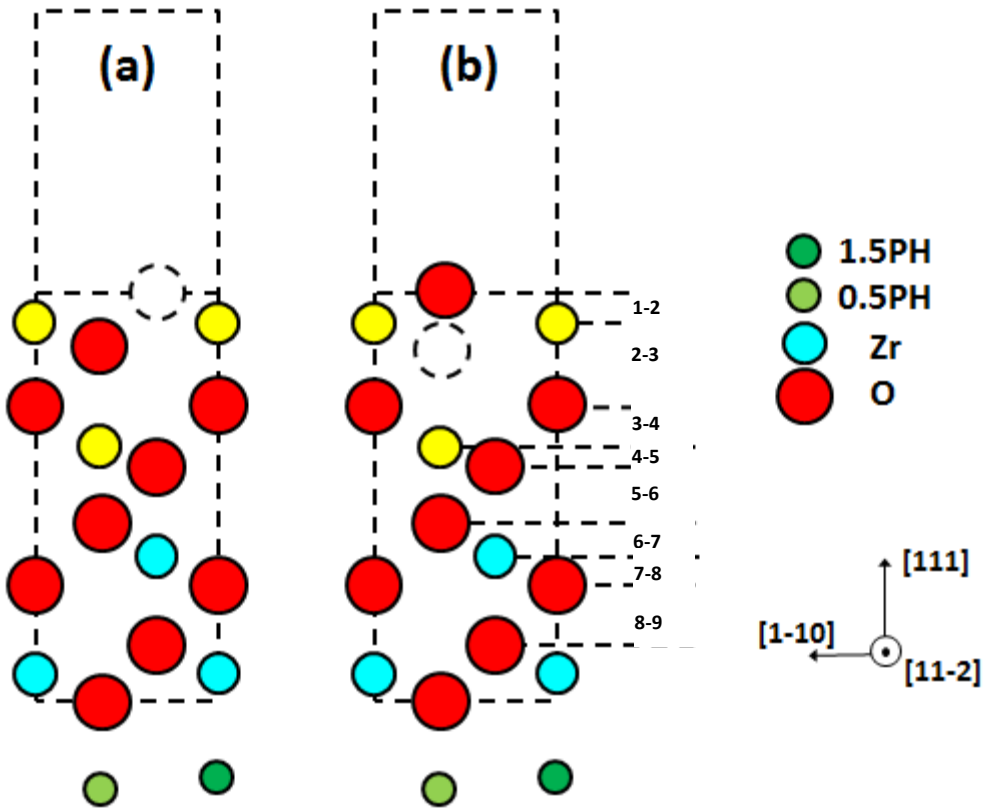

Fig. 3-13 Cross-sectional view of the Y-segregated slab: (a) before relaxation, (b) after relaxation.

The results of interplanar relaxations help us understand the difference between the surface and the bulk structures. The cross-sectional views of the slabs are shown in Fig. 3-12 and 3-13. Firstly, the surface layers have changed enormously compared to the inner layer for both of the slabs. In the truncated bulk surface, equilibrium positions of the remaining atoms are broken. A new balance will be established after the relaxations. It will create a different surface structure. Overall, in case of the segregation-free slab, the interplanar spaces between O layers and Zr layers ($d_{1\text{-}2}$ and $d_{4\text{-}5}$) will increase. The interplanar spaces between Zr layers and O layers ($d_{2\text{-}3}$ and $d_{5\text{-}6}$) are nearly unchanged. The interplanar spaces between O layers and O layers ($d_{3\text{-}4}$ and $d_{6\text{-}7}$) will decrease. The interplanar space below the $d_{6\text{-}7}$ is almost same as bulk. Similar results of interplanar relaxation are found in the previous report [3.44]. In case of the Y-segregated slab, it is found that the relaxation of the Y-segregated slab is larger than

that of the segregation-free slab. The O atoms even displace from its original position in the (111) surface. It can be attributed to the O vacancies and Y atoms at the surface region. These defects destroy the periodic structure and lead to a large relaxation.

Secondly, it is found that both of the slabs are O-terminated after the surface relaxations. The stability of O-termination structure is independent of the surface relaxation and the content of the Y dopants at the surface region.

Total energies of the slabs before and after the relaxations are summarized in table 3.6. The negative value means the slab is stable. These calculation results show that the surface relaxation had an energy gain. Therefore, a more stable surface structure is obtained after the relaxation.

Table 3.6 Total energy of the YSZ (111) surface.

	Before relaxation (eV)	After relaxation (eV)
unit cell 1×1	-320.26797	-320.26925
unit cell 2×2	-1281.0719	-1281.07698

3.3.3 Adsorption of In and N on the YSZ (111) surface

The Y-segregation-free and Y-segregated slabs have been obtained in last section. In this section, on the basis of the slab models, adsorption energies of In and N on the two YSZ (111) surface will be investigated respectively. The initial stage of InN growth on the YSZ (111) substrates will be discussed. In the calculation, it is assumed that the film procures are neutral In and N atoms.

The adsorption energy $E_{adsorption}$ is defined as

$$E_{adsorption} = E_{substrate} + E_{adatom} - E_{total}. \qquad (3.3)$$

Here E_{total} is the energy for the substrate with an adatom adsorbed on it. $E_{substrate}$ is the energy for the substrate without adatom. E_{adatom} is the energy for an isolated adatom. According to the definition in eq. 3.3, a positive value of $E_{adsorption}$ indicates

exothermic (stable) reaction and a negative value indicates endothermic (unstable) reaction. A larger value corresponds to more stable adsorption. The definition of the adsorption can also be described in Fig. 3-14.

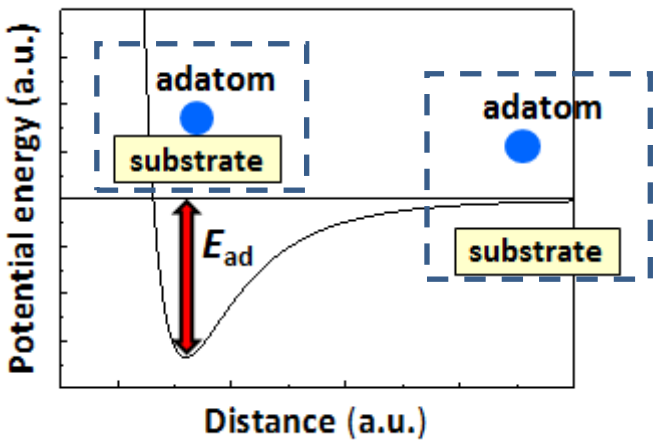

Fig. 3-14 Definition of the adsorption energy.

As shown in Fig. 3-14, one adatom is put on the slab mode. The adatom only can move along the z-axis. The position in z-axis is determined by the atomic force on the adatom. The convergence criteria of the atomic forces are 1.0×10^{-3} hartree/bohr. Since the atomic force fulfills the convergence criteria, the system (adatom and surface) will have the most stable total energy. Based on the eq. 3.3, the adsorption energy on this site is obtained. The investigations of the adsorption energy will be carried out at various high symmetric sites on each surface.

As mentioned in section 3.3.2, two slabs models have been prepared for the YSZ substrates with different Y contents at the surface region. After that, investigation of the adsorption will be performed on the two slabs.

For the Y-segregation free slab, adsorption of In and N on seven high-symmetric adsorption sites were investigated as shown in Fig. 3-15. These adsorption sites consist of three on-top sites, three bridge sites, and one hollow site. The three on-top sites are denoted as top O_u, top Zr, and top O_d, respectively. Specifically, O_u (up) is an O atom in

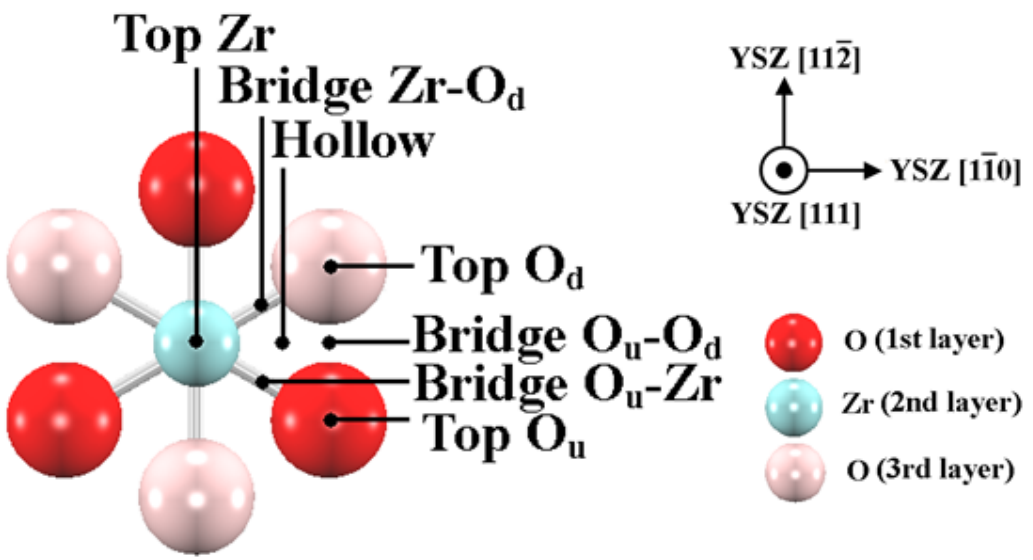

Fig. 3-15 Adsorption sites for the segregation-free slab surface.

the first layer and O_d (down) is an O atom in the third layer, respectively. The three bridge sites are denoted as bridge O_u-Zr, bridge Zr-O_d, and bridge O_u-O_d, respectively. The hollow site sitting on the center of an O_u atom, a Zr atom, and an O_d atom is labeled as Hollow.

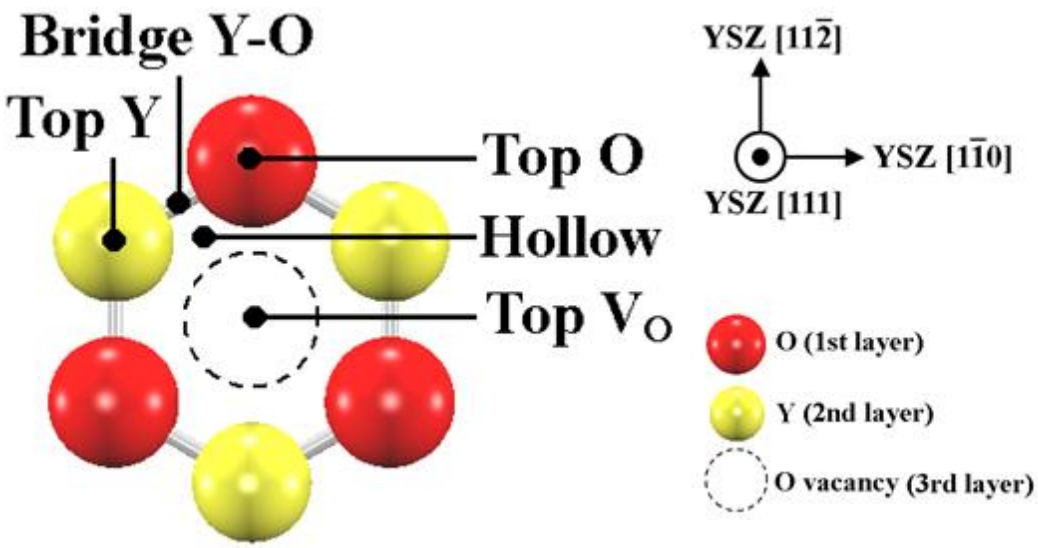

Fig. 3-16 Adsorption sites for the Y-segregated slab surface.

For the Y-segregated slab, five highly-symmetric adsorption sites are chosen. As shown in Fig. 3-16, these adsorption sites included three on-top sites, one bridge site, and one hollow site. The three on-top sites are labeled as top O, top V_O and top Y, where V_O denotes an oxygen vacancy. The bridge site is labeled as bridge Y-O. The hollow site sitting on the center of O, Y, and V_O is labeled as Hollow.

The results for the In and N adsorption on the segregation-free slab are summarized in Table 3.7. The positive values denote that the adsorption is more stable than the corresponding surface and the isolated adatom. It is found that the adsorption energy of a single N adatom on the 2×2 surface is larger than that of single In adatom. It means a nitrogen monolayer is more strongly bound to the substrate than the indium monolayer at the initial stage of the growth.

Table 3.7 Adsorption energies (eV) on the segregation-free slab surface.

Adatom	Adsorption sites						
	Top O_u	Bridge O_u-Zr	Top Zr	Bridge Zr-O_d	Top O_d	Bridge O_u-O_d	Hollow
In	0.43	0.46	0.32	0.44	0.27	0.50	0.46
N	0.82	2.00	1.31	0.31	1.27	1.94	1.89

The differences of the indium adsorption energy at different adsorption sites were smaller than the nitrogen. It can be attributed to the fact that the bond lengths of the indium adatom equilibrium were longer than the nitrogen. In case of the In adsorption, the bondlength between In and first layer O is 2.42 Å. In case of the N adsorption, the bondlength is 1.43 Å. The difference in bondlength is determined the hybridizations between the adatom and the atoms at the surface region of the substrates. Detail DOS analysis will be performed to discuss it later. The influence from the surface on the

adatom became weak if the bondlength is long. Based on this point of view, it can be predicted that the migrations of indium adatoms at the initial stage are more likely to happen than the nitrogen adatoms. Similar tendencies are reported for adsorptions of Cu, Ag, and Au atoms on cubic zirconia (111) surfaces [3.44]. The reports about simulations of nitrides growth on various substrates (sapphire, Fe, $LiNbO_3$) get the same conclusion that the nitrogen adatom is more energetically stable on the substrates at the initial stage.

The results of the adsorption energy for the Y-segregated surface are summarized in table. 3.8. It is same as the results of segregation-free slab. On one hand, N atom has the lager adoption energy than that of the In atom. It means the first layer should be the N layer at the initial stage. On the other hand, it can be seen that the differences in adsorption energies of In atoms at various sites are less than 0.25 eV. It is very small compared to that of N atoms at various sites. This result indicates that the migration of indium atoms on Y-segregated slab easily occurs. At the same time, the larger differences in adsorption energies of N atoms at various sites suggest that nitrogen atoms tend to stay on one site.

Table 3.8 Adsorption energies (eV) on the Y-segregated slab surface.

Adatom	Adsorption site				
	Top O	Top V_O	Top Y	Bridge Y-O	Hollow
In	0.25	0.27	0.26	0.15	0.28
N	0.98	0.52	1.38	1.37	1.31

It is found that N atom is stable on both Y-segregation free slab and Y-segregated slab than indium. These results suggest that the first layer of InN (0001) on YSZ (111) surfaces should consist of the N layer.

As mentioned before, the 2×2 slab model in the periodic system is employed to mimic the substrate. Adatom on the 2×2 slab gives out a surface coverage of 0.25 ML. To make sure the interactions between the neighboring adatoms are negligible compared to the adsorption energy at such coverage, the charge density analysis of the adatom adsorbed on the surface will be performed. The cross-sectional view of the slab in the periodic system is shown in Fig. 3-17. It gives us the charge density of the N atom absorbed on the Y-segregation-free slab in Fig. 3-17 (a). Fig. 3-17 (b) presents the charge density of the Y-segregation-free surface without adatom subtracted from Fig. 3-17 (a). It is obvious that the adatom only has direct interactions with nearest O and Zr atoms of the slab. It is found that there are no obvious interactions not only between adatom and other atom in the surface region but also between the adatoms in the neighbor slabs. It indicates that the adsorption energy is mostly determined by adatom-substrate interactions. Therefore, the 2×2 slab is sufficient for the adsorption energy calculation.

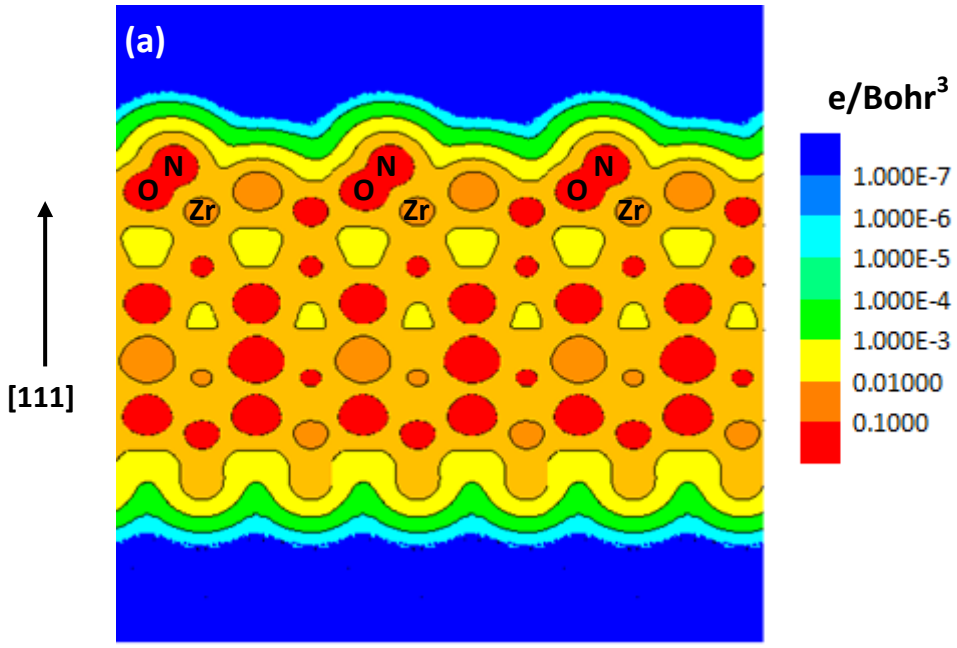

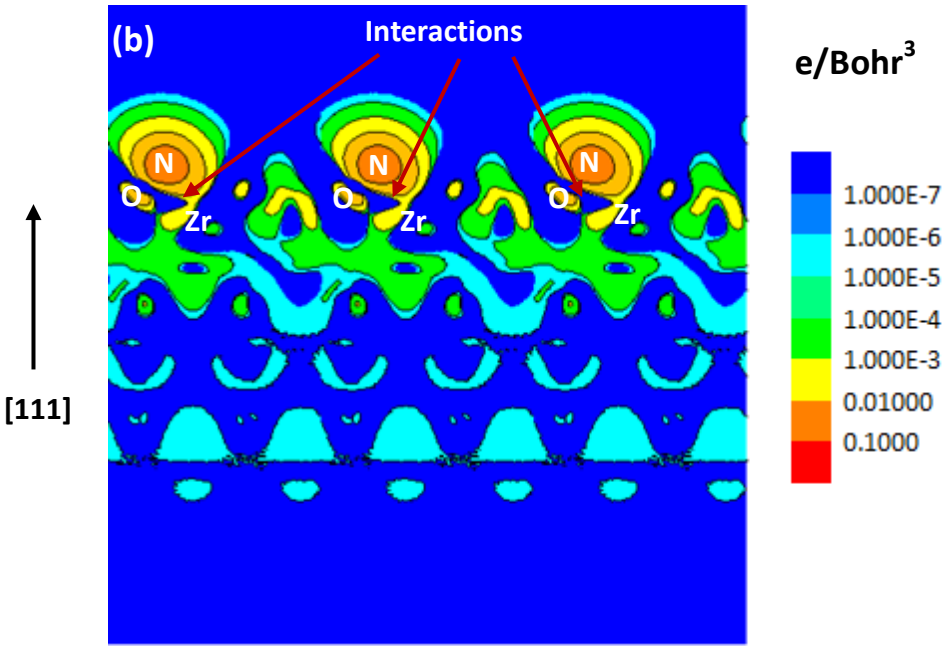

Fig.3-17 Contour plots of the charge density : (a) N atom absorbed on the Y-segregation-free slab (b) the Y-segregation-free surface without adatom subtracted from (a).

Based on the calculated adsorption energies, the energy potential maps for nitrogen adsorption on the Y-segregation-free and Y-segregated slab are plotted in Fig. 3-18. The potentials energy map is helpful to understand the migration of the adatoms on the surface.

According to the Boltzmann distribution [3.52], the possibilities of adatom arriving at adsorption sites could be roughly estimated based on the adsorption energies. The possibilities for segregation-free and Y-segregated slabs are summarized in Table 3.9. It is found that the possibilities for the first three stable sites are dominant. On the other hand, the possibility for the other unstable sites is very small. As a result, the site with smaller adsorption energy could be ignored. It can be predicted that the N adatom will stay at the first three stable sites with large adsorption energies.

According to the results in table 3.7 and 3.8, for the N adsorption energies, it is found that the energy difference between the first three stable sites is less than 60

meV for both of the segregation-free and Y-segregated slabs. At the same time, it has shown that the locations of first three sites are close to each other in Fig. 3-18. As mentioned before, the growth temperature of InN on YSZ substrates by PLD is up to 580°C. The k_BT is about 70 meV in such growth temperature. Hence, even if the adatom arrives at the second or third stable sites, the energy in such growth temperature will make the adatom gradually migrate to the most stable site.

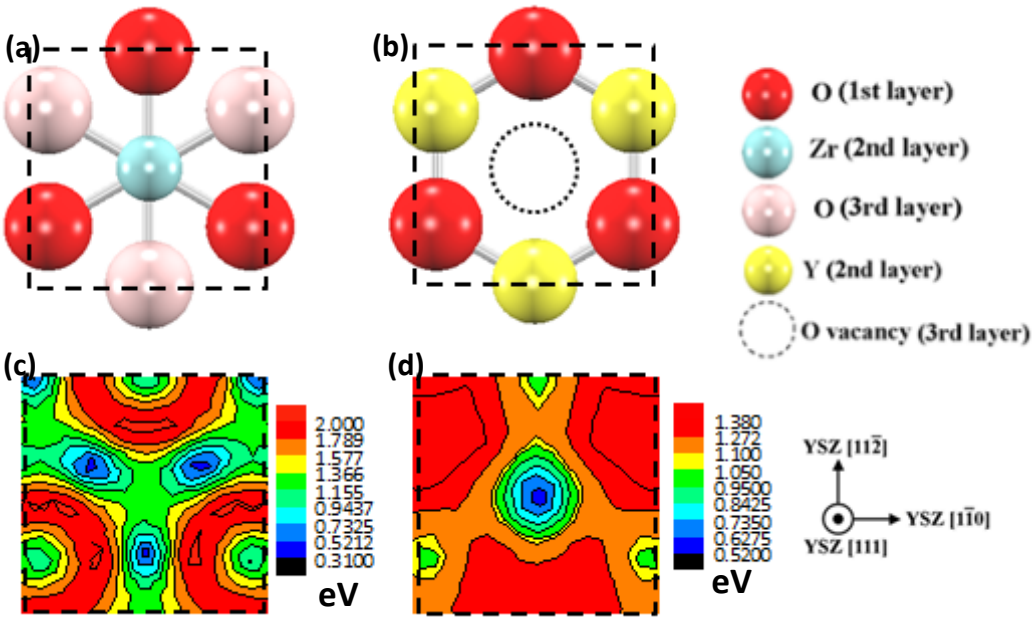

Fig. 3-18 Potential map of N adsorption energy: (a) (c) for the segregation-free slab and (b) (d) for the Y-segregated slab.

Table 3.9 ratio of the atom arriving at the different sites.

	1st	2nd	3rd	4th	5th	6th	7th
Segregation -free	Bridge O_u-Zr 61.1%	Bridge O_u-O_d 26.1%	Hollow 12.8%	Top Zr 0.0%	Top O_d 0.0%	Top O_u 0.0%	Bridge Zr-O_d 0.0%
Y-segregated	Top Y 44.6%	Bridge Y-O 38.7%	Hollow 16.5%	Top O 0.2%	Top V_O 0.0%		

It has been known that the N atom is stable on the both slabs compared to the In atom. In case of the segregation-free slab, the bridge site between the first layer

oxygen and the second layer zirconium was the most stable site for the nitrogen adatom to growth at the initial stage. In case of the Y-segregated slab, the nitrogen atom is stable on the top site of the surface yttrium. For a better comparison of the two slab model, the top view of the atomic structure is shown in Fig. 3-19. The bondlength and adsorption energies are shown in table 3.10.

Table 3.10 Comparison of N adsorption on segregation-free and Y-segregated slabs.

	Segregation-free	Y-segregated
Most stable site	Bridge O_u-Zr	Top Y
Adsorption energy of N (eV)	2.00	1.38
Bond length (Å)	N-O =1.34 N-Zr =1.96	N-O = 2.16 N-Y = 2.88

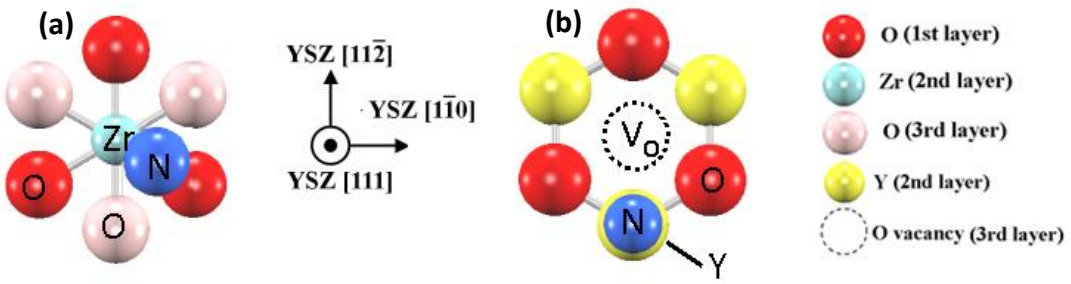

Fig. 3-19 Top view of N adsorbed on YSZ slabs: (a) segregation-free slab (b) Y-segregated slab.

It gives us the top view of the nitrogen adsorbed on the most stable sites on the segregation-free (a) and Y-segregated (b) slabs in Fig. 3-19. It is found that the adsorption energy of nitrogen atom on the segregation-free surface is larger than that of the Y-segregated surface. In fact, for the In atom, adsorption energies on the segregation-free (a) slab is larger than that of Y-segregated (b) slab too. The bond length of N on the segregation free slab and Y-segregated slab are listed in table 3.10. In case of the segregation-free slab, both the N-O and N-Zr bonds are short compared

with the N-O and N-Y bonds on the Y-segregated slab. These results are consistent with the adsorption energies. It indicates that the bond lengths of the adatom adsorbed on the slab surface are determined by the adsorption energy. Large adsorption energy means strong interaction between the adatom and the surface and leads to short bond with the atom at the surface region.

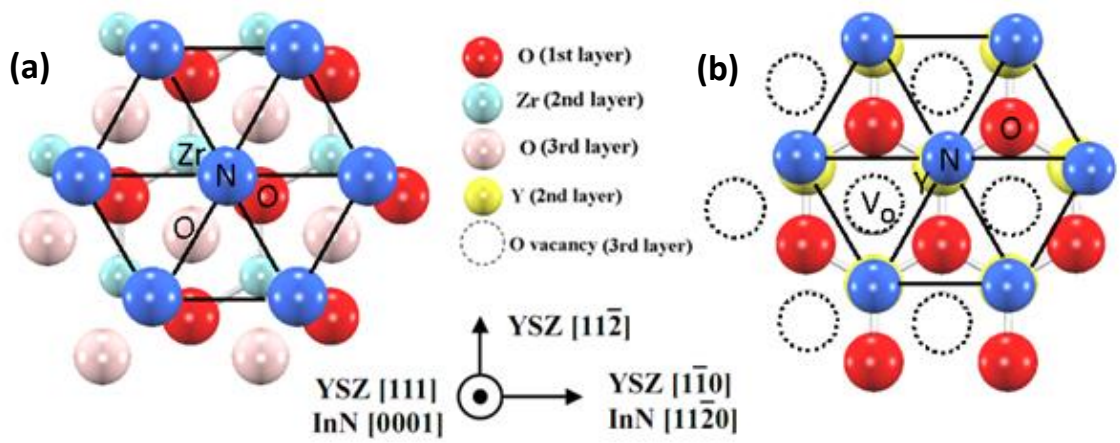

Fig. 3-20 Arrangement of the N layer adsorbed on the YSZ (111) surfaces: (a) no yttrium at the surface region defined as segregation-free surface (b) yttrium enrichment at the surface region defined as Y-segregated surface.

As mentioned before, it is already known that the lattice constant of the InN is 3.54 Å. In case of the slab model, the size of the corresponding (111) surface unit cell was 3.63 Å. Let us suppose that the crystal growth proceeds while keeping the first nitrogen atom on the most stable site. The InN/YSZ in-plane epitaxial relationship will be obtained. It shows us that all of the nitrogen atoms are adsorbed at the stable sites in every 1×1 unit cell of (111) surface at the initial stage of growth in Fig. 3-20. The regular hexagon structure composed of nitrogen atoms suggested us top view of the c-plane wurtzite InN. As a result, the epitaxial relationships of YSZ (111) // InN (0001) and InN [11-20] // YSZ [1-10] are determined. As mentioned in chapter 1, the epitaxial same relationships have been confirmed before. Theoretical results agreed well with the experimental results. This indicates that the epitaxial relationships can be

estimated on the basis of the theoretical investigations. Considering these results and the reported phenomena such as GaN/Sapphire [1.49] and InN/Sapphire [1.53], the theoretical approach is a powerful tool to estimate the in-plane alignment in hetero-epitaxial growth. Consequently, with the help of the DFT calculation, the mechanism of epitaxial relationship formation of InN/YSZ system is elucidated on the basis of the adsorption of the initial stage.

3.3.4 DOS analysis of the adsorption on the YSZ (111) surface

The adsorption of In and N on the YSZ (111) has been investigated in last section. In this section, the density of states (DOS) calculation is carried out to investigate the electronic state of the In or N adsorption on the segregation-free and Y-segregated slabs.

Firstly, the DOS analyses are carried out for the slab model without adatom on it. In Fig. 3-21 (a), it shows us the local DOSs of the first layer O and second layer Zr in the surface region of the segregation-free slab model. In Fig. 3-21 (b), it shows us the local DOSs of the first layer O and second layer Y in the surface region of the Y-segregated slab model.

(a)

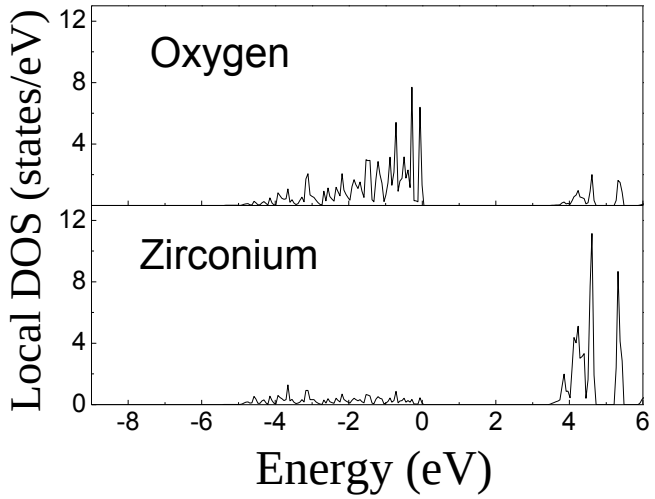

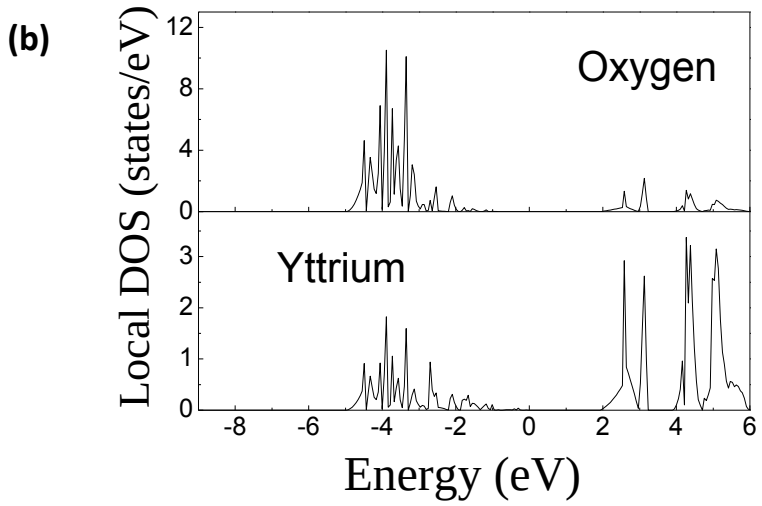

Fig. 3-21 Local DOSs of (a) first layer O and second layer Zr in the segregation-free slab, and (b) In and first layer O and second layer Y in the Y-segregated slab.

A comparison between the (a) and (b) in Fig. 3-21 shows the difference in surface O between the segregation-free and Y-segregated slabs. In case of the segregation-free slab, the DOS is shifted to the high energy level. In case of the Y-segregated slab, the DOS is shifted to the low energy level. These results are due to the different atoms at the second layers. It is found that the hybridization between the O and Zr is weaker than that between the O and Y. As a result, the major difference of the metal atom at the surface region will affect the electronic states of the O at the surface region. This is also the reason why the atomic structures of the segregation-free and Y-segregated slabs are different after the surface relaxations.

Secondly, to confirm the relationship between the adsorption energy and electronic states, the DOS of atom on the slab will be discussed. For the segregation-free slab, N atom is most stable on the bridge O_u-Zr site and unstable on the bridge Zr-O_d site. DOS investigations are performed in the two cases. The results are shown in Fig. 3-22 (a). It gives us the local DOSs of the N atom and the O atom. The O atom is the O_u in the bridge O_u-Zr site. It is the nearest atom to the N in the surface region. In contrast to the

N, the DOS investigations of In adsorption are presented in Fig. 3-22 (b).

In Fig. 3-22 (a), the hybridizations between N2*p* and O2*p* could be seen clearly. It shows a strong hybridization between N2*p* and O2*p* extended to -7eV for the most stable bridge O_u-Zr site. In comparison with the bridge O_u-Zr site, the hybridization for the unstable bridge Zr-O_d site are weak and only extended to -6eV. It means there will be strong N2*p* - O2*p* hybridizations when the N atom arrives at the stable bridge O_u-Zr site. The strength of the hybridizations will decrease when the N atom arrives at the less stable site. The results of hybridizations on different sites are quire consistent with the adsorption energies. It can be predicted that the adsorption energy of N on the slab could be determined by the hybridization between N and O. On the other hand, as shown in Fig. 3-22 (b), it is known that the adsorption energy of In on the slab should be determined by the hybridizations between the In5*s* and O2*p*. In Fig. 3-12 (b), it shows the difference in In-O hybridizations between the stable site (bridge O_u-O_d) and the unstable site (top O_d) is very small. It can be expected that the adsorption energy difference between the two sites should be small too. As mentioned in last section, the energy difference for In at various adsorption sites is small. These calculated energies are quite agreeable to the results of DOS.

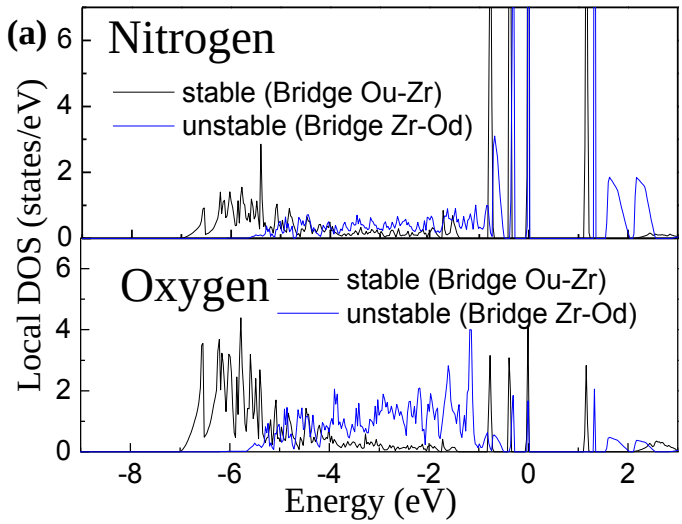

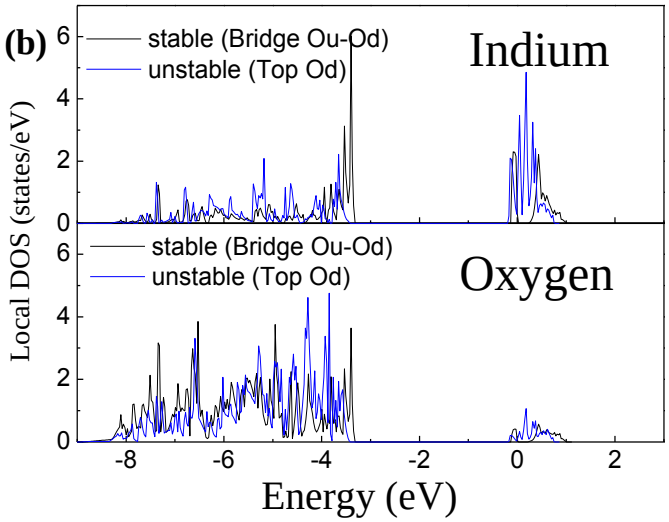

Fig. 3-22 Local DOSs of (a) N and O atoms for the N adsorption on the stable site (Bridge O_u-Zr) and the unstable site (Bridge Zr-O_d), and (b) In and O atoms for the In adsorption on the stable site (Bridge O_u-O_d) and the unstable site (Top O_d).

Thirdly, to understand the reason why the segregation-free slab has larger adsorption energy than Y-segregated slab, the local DOS of N adsorption on the slabs will be discussed.

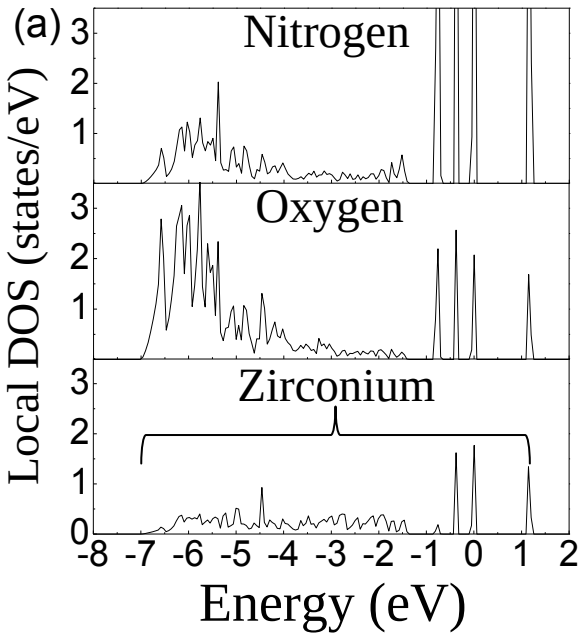

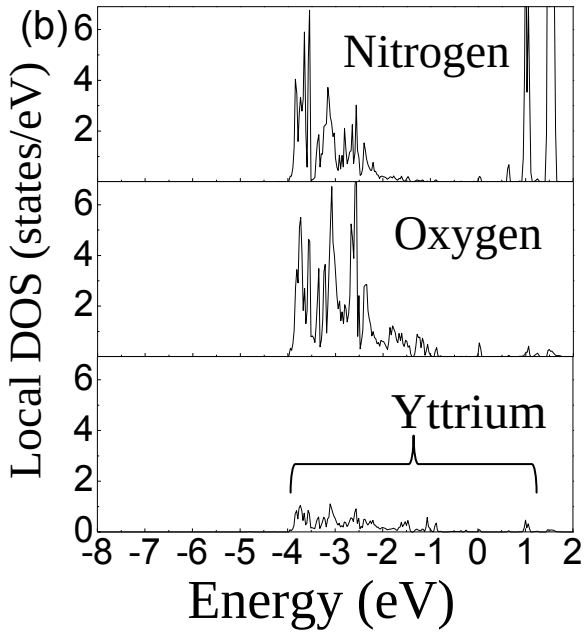

Fig. 3-23 Local DOSs for a nitrogen atom on (a) segregation-free slab, and (b) Y-segregated slab.

The DOS analyses are performed to understand the dependence of the adsorption energies of a nitrogen atom on the yttrium segregation. In Fig. 3-23 (a), it shows the local DOS of the N atom, O atom at the first layer and the Zr atom at the second layer for the segregation-free slab. In Fig. 3-23 (b), it shows the local DOSs of the N atom, O atom at the first layer and the Y atom at the second layer for the Y- segregated slab. First of all, hybridizations among the N2*p*, O2*p* and Zr4*d* (or Y4*d*) are confirmed because the DOS are found at the same energy level for both segregation-free slab (a) and Y-segregated slab (b). The hybridization between the N2*p* and O2*p* orbitals is a major part of the hybridization. It can be predicted that the adsorption is manly determined by the interaction between the adatom and the first layer O atoms. Secondly, it is found that the hybridization of the segregation-free (a) slab is stronger than that of Y-segregated (b). Particularly, in one hand, hybridization in segregation-free slab (a) extends to -7eV over a wide range. In the other hand, hybridization in Y-segregation slab (b) only extends to -4eV. At the same time, it can

also see that there exists a clear hybridization between N2*p* and Zr4*d* on the Y-segregation-free slab (a). The hybridization extends to the low energy to -7 eV. On the other side, the range of the hybridization between N2*p* and Y4*d* is small (to -4 eV) on the Y-segregated slab (b). This means that the hybridization on Y-segregated slab is weak compared to that on segregation-free slab. It indicates that the hybridization between the adatom and the second layer Zr (or Y) atoms can also affect the adsorption. As a result, the adsorptions of the N atom on the two slabs in Fig. 3-23 are different. The DOS analysis is quite consisted with the calculated adsorption energies in section 3.3.3. Although it is possible to provide a qualitative analysis of the hybridization strength, it is unfortunately known that the quantitative analysis of the hybridization strength requires other methods such as the analysis of charge distribution [3.53].

3.3.5 Arrival of second an adatom on the surface

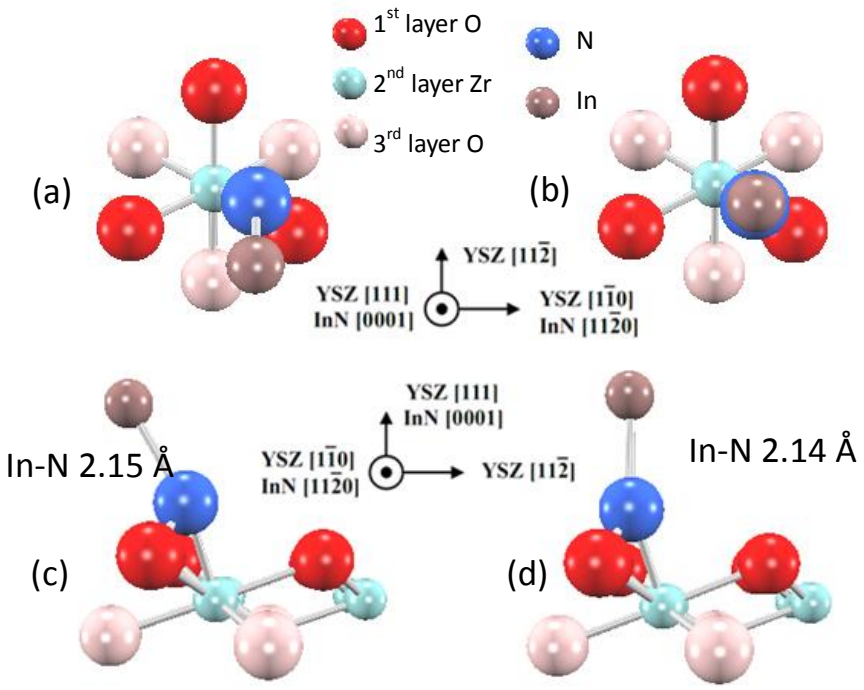

Fig. 3-24 Top view of the surface structure: (a) In atom lies beside the N, (b) In atom lies on top of the N. Side view of the surface structure: (c) In atom lies beside the N, (d) In atom lies on top of the N.

As in last section, in case of one adatom, It is found that N is stable than In on the segregation-free and Y-segregated slabs. Here a discussion will be carried out to investigate the case of second adatom arrived at the surface.

When a N atom approaches the surface, it is found that the second N is energetically favorable to adsorb on the surface instead of formation of nitrogen molecular with the first N adatom. The result indicates that the interaction between the 1st and 2nd N atoms is quite small compared to that between the atoms and the surface.

If the second adatom is In, as shown in Fig. 3-24, the top view and side view of the In and N on the slab are shown. The structures of the second In atom on the slab are relaxed on the basis of convergence criteria of 1.0 × 10-3 hartree/bohr. The total energies for (a) and (b) in Fig. 3-24 are -36653.15 eV and -36653.21 eV, respectively. These results mean the second In are energetically stable on top layer of the N atom. The structure is quite consistent with the *c*-plane InN. It could be predicted that the first layer is composed of N atoms. The In atoms are preferentially on the second layer on top of the N atom.

3.4 Summary

The growth mechanisms of InN epitaxial growth on yttria stabilized zirconia (YSZ) (111) substrates are investigated by first principles calculation in chapter 3. The adsorption energies of In and N adatom on the Y-segregation-free and Y-segregated slabs are studied by total energy calculation. The most stable sites for In and N adsorption on the surfaces are investigated respectively. N atoms have lager adsorption energies than In atoms on both segregation-free and Y-segregated slabs. This indicates that the first layer at the initial stage of the growth should be a nitrogen layer. The theoretical calculations have revealed that the epitaxial relationships of YSZ (111) // InN (0001) and InN [11-20] // YSZ [1-10] are determined by the adsorption process of

nitrogen atoms on the surfaces at the initial stage of the growth. The local DOS analysis reveals that there exists a clear strong hybridization between N2*p* and Zr4*d* on the Y-segregation-free surface. On the other hand, weak hybridization between N2*p* and Y4*d* is observed on the Y-segregated surface probably due to the difference of the number of valence electrons for Zr and Y atoms. Therefore, the segregated Y atoms will affect the adsorption energy of adatoms on the Y-segregated zirconia substrates..

Reference

[3.1] JCPDS XRD pattern No.37-1484.

[3.2] JCPDS XRD pattern No.42-1164.

[33] C. R. A. Catlow, J. Chem. Soc., Faraday Trans. **86**, 1167 (1990).

[3.4] G. Balducci, J. Kaspar, P. Fornasiero and M. Graziani, M. S. Islam and J. D. Gale, J. Phys. Chem. B **101**, 1750 (1997).

[3.5] A. Predith, G. Ceder, C. Wolverton, K. Persson and T. Mueller, Phys. Rev. B **77**, 144104 (2008).

[3.6] T. H. Etsell and S. N. Flengas, Chem. Rev. **70**, 339 (1970)

[3.7] B. Nacke, T. Behren, M. Kudryash and A. Jakovics, SKULL MELTING TECHNOLOGY FOR OXIDES AND GLASSES

[3.8] C. Pascual and P. Durán, J. Am. Ceram. Soc. **66**, 22 (1983).

[3.9] M. Yashima, H. Takanhashi, K. Ohtake, T. Hirose. M. Kakihana, H. Arashi and M. J. Yoshimura. J. Am. Ceram. Soc. **57**, 289 (1996).

[3.10] C. Schusterius and N. N. Padurow, Ber, Dtsch, Keram. Ges. **30**, 235 (1953).

[3.11] S. P. S. Badwal, Solid State Ionics **52**, 23 (1992).

[3.12] J. Katamura and T. Sakuma, Acta. Mater. **46** (5), 1569 (1998).

[3.13] A. Bogicevic and C. Wolverton, Phys. Rev. B **67**, 024106 (2003).

[3.14] A. Bogicevic and C. Wolverton, Europhys. Lett. **56**, 393 (2001).

[3.15] F. Frey, H. Boysen and I. Kaiser-Bischoff, Z. Kristallogr. **220**, 1017 (2005).

[3.16] C. Catlow, A. Chadwick, G. N. Greaves and L. Moroney, J. Am. Ceram. Soc. **69**, 272 (1986).

[3.17] D. Steele and B. Fender, J. Phys. C **7**, 1 (1974).

[3.18] D. Argyriou, M. Elcombe and A. Larson, J. Phys. Chem. Solids **57**, 183 (1996).

[3.19] K. McClellan, S.-Q. Xiao, K. Lagerlof and A. Heuer, Philos. Mag. A **70**, 185 (1994).

[3.20] S. Suzuki, M. Tanaka and M. Ishigame, J. Phys. C **20**, 2963 (1987).

[3.21] T. Welberry, R. Withers, J. Thompson and B. Butler, J. Solid State Chem. **100**, 71 (1992).

[3.22] M. Zacate, L. Minervini, D. Bradfield, R. Grimes and K. Sickafus, Solid State Ionics **128**, 243 (2000).

[3.23] A. Gallardo-Lopez, J. Martinez-Fernandez and A. Dominguez- Rodriguez, J. Eur. Ceram. Soc. **22**, 2821 (2002).

[3.24] P. Li, I. Chen and J. Penner-Hahn, J. Am. Ceram. Soc. **77**, 118 (1994).

[3.25] A. Gallardo-Lopez, J. Martinez-Fernandez and A. Dominguez-Rodriguez, Philos. Mag. A **81**, 1675 (2001).

[3.26] X. Xia, R. Oldman and R.Catlow, Chem. Mater. **21**, 3576 (2009).

[3.27] C. Morterra, G. Cerrato, L. Ferroni and L. Montanara. Mat. Chem. and Phys. **37**, 243 (1994).

[3.28] F. Haase and J. Sauer, J. Am. Chem Soc. **120**, 13503 (1998).

[3.29] G. Balducci, J. Kaspar, P. Fornasiero and M. Graziani M. S. Islam, J. Phys. Chem. B **102**, 557 (1998).

[3.30] A. Bernasik, K. Kowalski and A. Sadowski, J. Phys. Chem. Solids **63**, 233 (2002).

[3.31] A. Eichler and G. Kresse, Phys. Rev. B. **69**, 045402 (2004).

[3.32] D. Majumdar and D. Chatterjee, J. Appl. Phys. **70**, 988 (1991).

[3.33] M. de Ridder, R. G. van Welzenis, A. W. Denier van der Gon and H. H. Brongersma, J. Appl. Phys. **92**, 3056 (2002).

[3.34] J. Zhu, J. G. van Ommen, J. Henny, M. Bouwmeester and L. J. Lefferts, Catal. **233**, 434 (2005).

[3.35] G. Ballabio, M. Bernasconi, F. Pietrucci and S. Serra, Phys. Rev. B. **70**, 075417 (2004).

[3.36] C. R. Stanek, R. W. Grimes, M. J. D. Rushton, K. J. McClellan and R. D. Rawlings, Philos. Mag. Lett. **85**, 445 (2006).

[3.37] J. Lahiri, A. Mayernick , S. L. Morrow , B. E. Koel, A. C. T. van Duin , M. J. Janik and M. Batzill J. Phys. Chem. C **114**, 5990 (2010).

[3.38] A. Kobayashi, K. Okubo, J. Ohta, M. Oshima and H. Fujioka, Phys. Status Solidi A **209**, 2251 (2012).

[3.39] K. Okubo, A. Kobayashi, J. Ohta, H. Fujioka and M. Oshima, Appl. Phys. Express **4**, 091002 (2011)

[3.40] T. Honke, H. Fujioka, J. Ohta and M. Oshima, J. Vac. Sci. Technol. A **22**, 2487 (2004).

[3.41] J. P. Perdew, K. Burke and M. Ernzerhof, Phys. Rev. Lett. **77**, 3865 (1996).

[3.42] D. Vanderbilt, Phys. Rev. B **41**, 7892 (1990).

[3.43] http://www.advancesoft.jp.

[3.44] R. Grau-Crespo, N. Cruz Hernández, J. F. Sanz and N. H. de Leeuw, J. Phys. Chem. C **111**, 10448 (2007).

[3.45] G. Jomard, T. Petit, A. Pasturel, et al., Phys. Rev. B, **59**, 4044 (1999).

[3.46] B. Králik, E. K. Chang and S. G. Louie, Phys. Rev. B **57**, 7027 (1998).

[3.47] B.E. Douglas and D.H. McDaniel, Concepts and Models of Inorganic Chemistry Blaisdell, New York, 90 (1965).

[3.48] B. Meyer and D. Vanderbilt, Phys. Rev. B **63**, 205426 (2001).

[3.49] A. Christensen and E. A. Carter, Phys. Rev. B **58**, 8050 (1998)

[3.50] Feynman R., Phys. Rev. **56**, 340 (1939).

[3.51] H. J. Monkhorst and J. D. Pack, Phys. Rev. B **13**, 5188 (1976).

[3.52] Landau, L. Davidovich and Lifshitz, Evgeny Mikhailovich (1980).

[3.53] R. Grau-Crespo, F. Cora, A. A. Sokol, N. H. de Leeuw, and C. R. Catlow, Phys. Rev. B, **73**, 035116 (2006).

Chapter 4 Polarity determination for *c*-plane InN grown on YSZ (111) substrates

The initial stage of the InN growth on YSZ (111) substrates were investigated in chapter 3. The adsorption energies of single In and N adatoms on the Y-segregation-free and Y-segregated slabs were studied by the total energy calculation. The theoretical calculations had revealed that the epitaxial relationships of YSZ (111) // InN (0001) and InN [11-20] // YSZ [1-10] were determined by the adsorption process of nitrogen atoms on the surfaces at the initial stage of the growth. In this chapter, further research on the basis of the adsorption at the initial stage will be discussed. More precisely, adsorption of the In atom on the N layer covered segregation-free and Y-segregated slabs will be investigated. The structures are employed to mimic the first InN layer on the YSZ substrate. Based on the investigations of the interface structures of the InN/YSZ system, the mechanism of the polarity determination for InN (0001) on YSZ (111) substrate will be elucidated.

4.1 Polarity control of InN on YSZ (111) substrates

In chapter 1 it was mentioned that group III-nitrides have polar axes due to the absence of the inversion center. In case of the InN, there will be two kinds of polarity structures. These are the In- and N polarities. The atomic structures of the In-polar and N-polar InN are shown in Fig. 1-3.

According to the existence of In- and N-polar structures, both In- and N-polar InN film could be obtained during the growth. It is already known that the In- and N-polar films have large differences in their crystal growth and surface structures. The polarity also significantly affects the electrical and optical properties of the nitride film. As a

result, the polarity is a very important parameter for the growth of InN.

Although the growth of In- and N-polar InN has already been reported in experiments, the theoretical studies on the mechanism about InN polarities growth are relatively few. In the case of the InN grown on the GaN substrates, the molecular dynamics (MD) simulations [4.1] of the InN on GaN (0001) surface find the InN films on Ga- and N-polar surface are quite different. The morphology of InN layer growth on the N-terminated GaN (0001) surface is rough and three-dimensional. Contrary to this, InN on the Ga-terminated (0001) surface has the result of two-dimensional growth. It is said that the growth mechanism can be interpreted from the viewpoint of the atomic interaction. In the case of the Ga-terminated surface, uniformly deposited InN molecules easily adhere to the surface instead of aggregating due to the strong atomic interaction. In the case of the N-terminated surface, the aggregation of InN molecules occurs and causes a three-dimensional growth [4.2-4.4].

As mentioned before, polarities are important parameters to the nitride. It is known that control of the polarity in the wurtzite nitrides is inherently important in exploring and investigating material properties [4.5]. At the same time, the mixture of the N-polar and metal-polar polarities will cause inversion domain boundaries [4.6, 4.7], which affect the performance of nitride-based devices. In order to avoid the mixture of these and keep the uniform N-(or metal-) polar nitride growth at the same time, polarity control will be carried out. Most of the controlling methods are based on interface engineering, such as substrate treatment before growth and insertions of the interfacial layers between substrates and the films.

In case of the InN growth on the YSZ (111) substrates, the polarity control was already reported [4.8]. In more detail, as mentioned in chapter 3, two types of YSZ (111) substrates are prepared by surface treatments. They are the Y-segregation-free substrate and the Y-segregated substrate. The control of Y-segregation at the surface region has been realized. Based on the segregation-free and Y-segregated substrates, the growth of InN films by pulsed laser deposition (PLD) will be investigated. The polarity of the InN films was examined by surface reconstructions [4.9] and chemical

etching in a KOH solution. It is established that the InN polarity could be confirmed by the KOH etching method. After a long time etching, the surface region of N-polar is rough. On the other hand, the surface region of In-polar is relatively smooth [4.10]. The KOH method could be used to characterize the polarity of InN grown on the YSZ substrates. It is found that the In-polar InN (0001) films with atomically flat surfaces grow on Y-segregated YSZ (111) substrates, which makes a striking contrast to the case of N-polar InN (000-1) films grown on the Y-segregation free YSZ (111) substrates with rough surfaces. Therefore, the control of InN polarity on the YSZ (111) substrates could be realized through Y-segregation at the surface region of the YSZ substrates.

In previous reports, the SEM and AFM measurements have been employed to investigate the surface morphology of InN grown on YSZ in Ref. 4.11. The root mean square (RMS) values of surface roughness were 0.6 and 6.9 nm for In- and N-polar InN films, respectively. These indicate that In-polar InN films are more suitable for the fabrication of abrupt heterointerface structures than for N-polar InN films, which have rougher surfaces [4.11]. However, the mechanism of the polarity determination for the InN/YSZ system is still not well understood. Further study is necessary to clarify the mechanism that determines the polarity of InN [4.8].

Table 4.1 Polarity control of InN on YSZ (111) [4.11].

Polarity	Yttrium segregation	Growth temperature
In-polar InN	Y-segregated	470 °C
N-polar InN	Y-segregation-free	580 °C

The experimental results of the InN polarity control on YSZ (111) substrates are summarized in table 4.1. From the growth experiment, it is known that the In-polar InN structure is always grown on the Y-segregated substrates. On the other hand, the growth of N-polar InN could be obtained at high temperature on the Y-segregation free

substrates. In order to find out the mechanism of the polarity determination for the InN/YSZ system and explain this phenomenon in the experiment, in this chapter theoretical study will be carried out to investigate the atomic structure of the InN/YSZ interface. On the basis of the theoretical study, the polarity determination of InN on YSZ (111) substrate will be discussed.

4.2 Theoretical study on the polarity determination

Theoretical investigation [4.13-4.14] could be employed to investigate the polarity determination when the experimental technique is limited. DFT has been used to investigate the interface stability of nitride growth on various substrates such as GaN/ZrB_2, GaN/Sc_2O_3 and GaN/Ga_2O_3 [4.15-4.17]. For the InN/YSZ, the mechanism of polarity determination will be investigated at this section.

4.2.1 In adsorption on N-covering YSZ substrates

Polarity control of InN (0001) films on YSZ substrates, which have no polarity, is another crucial issue because the mixture of N- and In-polar InN growth affects device performance. The inversion domain boundaries [4.12] originated from the mixture polarity will decrease the efficiency of the nitride-based device. As mentioned before, the control of InN polarity has been realized by the Y segregation on the substrates. In this section, theoretical investigation will be employed to characterize the InN/YSZ structure at the atomic scale.

As mentioned in chapter 3, it is already known that the N atom has larger adsorption energy than In atom on the YSZ (111) substrate. The initial stage of InN growth on the substrate should be a nitrogen layer. In this section, to understood the mechanism of InN polarity determination on the YSZ substrates, the adsorption of an In atom on the

N layer covering YSZ substrate are introduced to mimic the first InN layer growth on the substrate. The adsorption energy of the In atom on the N covering YSZ will be discussed.

The definition of adsorption energy on the N layer covering is similar as the one on the YSZ slab in chapter 3. The adsorption energies of an indium atom on the nitrogen layer covering YSZ (111) surfaces could be given by:

$$E_{\text{adsorption}} = E_{\text{nlayer/substrate}} + E_{\text{In}} - E_{\text{total}}. \qquad (4.1)$$

Here E_{total} is the energy of an In adsorbed on N layer-covering YSZ slab. $E_{\text{nlayer/substrate}}$ is the energy for the N layer-covering YSZ slab without In. E_{adatom} is the energy for an isolated In atom. According to the definition in eq. 4.1, $E_{\text{adsorption}}$ always has a positive value. A larger value corresponds to more stable adsorption.

As mentioned before, InN (0001) grown on the YSZ (111) substrates have hexagonal structures. From this point of view, the In atom will be placed on the YSZ slab according to the InN hexagonal structure (Fig. 1-3). For the N-polar InN, structures of an indium atom sitting on the top of a nitrogen atom correspond to N-polarity. For the In-polar InN, structures of an indium atom sitting on the center of three nitrogen atoms correspond to In-polarity. At the same time, there are two kinds of YSZ slabs. They are the segregation-free and Y-segregated slabs. In order to make a comparison between the segregation-free and Y-segregated slabs, In- and N-polar InN structure on the segregation-free and Y-segregated slabs are fully investigated.

In the case of the segregation-free slab, the top views of the surface region are shown in Fig. 4-4. Accordingly, the side views of Fig 4-4 are shown in Fig. 4-5. As mentioned before, the investigations are carried out on the 2×2 super cell. Therefore, there will be two kinds of In-polar position for the In atom to sit. It shows us the difference between the two In-polar structures in Fig. 4-4. For In-polar (a), there is only one surface O atom (red) close to the In atom. For the In-polar (b), there are two surface O (red) atom close to the In atom. The relative positions between the In and

surface O determine the difference. For the N-polar (c), there is only one possibility because the relative positions are all the same.

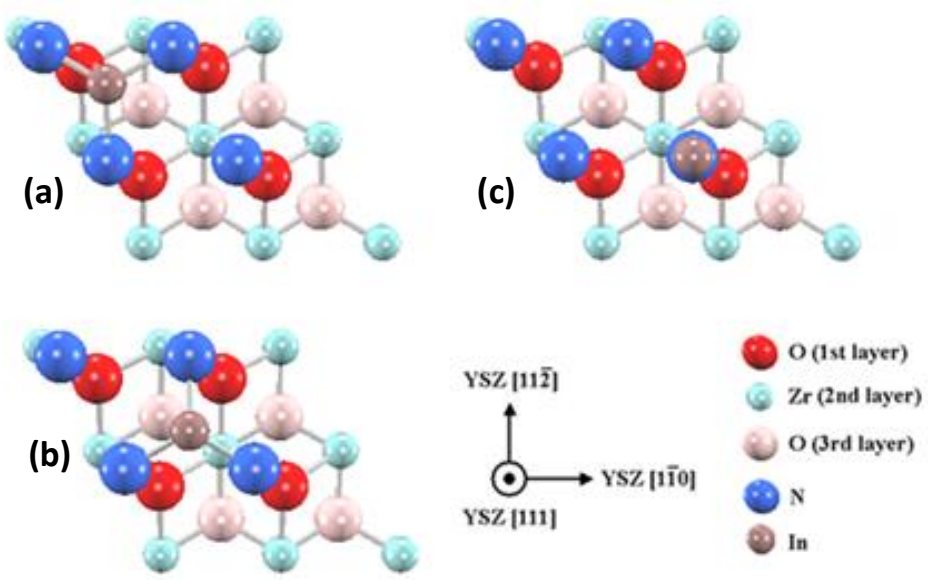

Fig. 4-4 Top views of In-polar InN (a) (b) and N-polar InN (c) on the segregation-free slab.

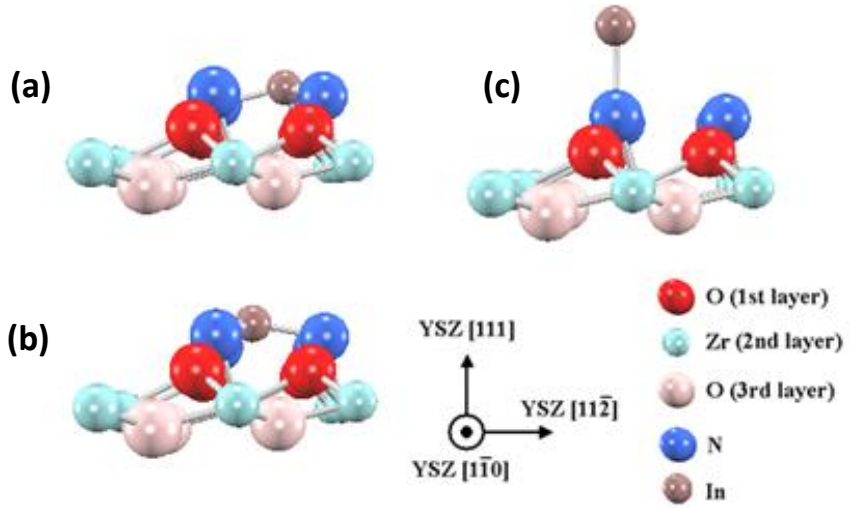

Fig. 4-5 Side views of In-polar InN (a) (b) and N-polar InN (c) on the segregation-free slab.

In the case of Y-segregated slab, the top views of the surface region are shown in Fig. 4-6. Accordingly, the side views of Fig 4-6 are shown in Fig. 4-7. It is same as the

segregation-free slab. According to the relative position between In atom and the surface O (red) atoms, two kinds of In-polar structure will be defined. For In-polar (a), the In atom is located in the middle of three oxygen vacancy (broken line) and lied on top of the surface O (red) atom. For the In-polar (b), the In atom is lied on top of the oxygen vacancy (broken line) and located in the middle of the surface O (red) atom. For the N-polar (c) structure, In atom is on top of the N atom. It is also surrounded by three O vacancies and O atoms, respectively.

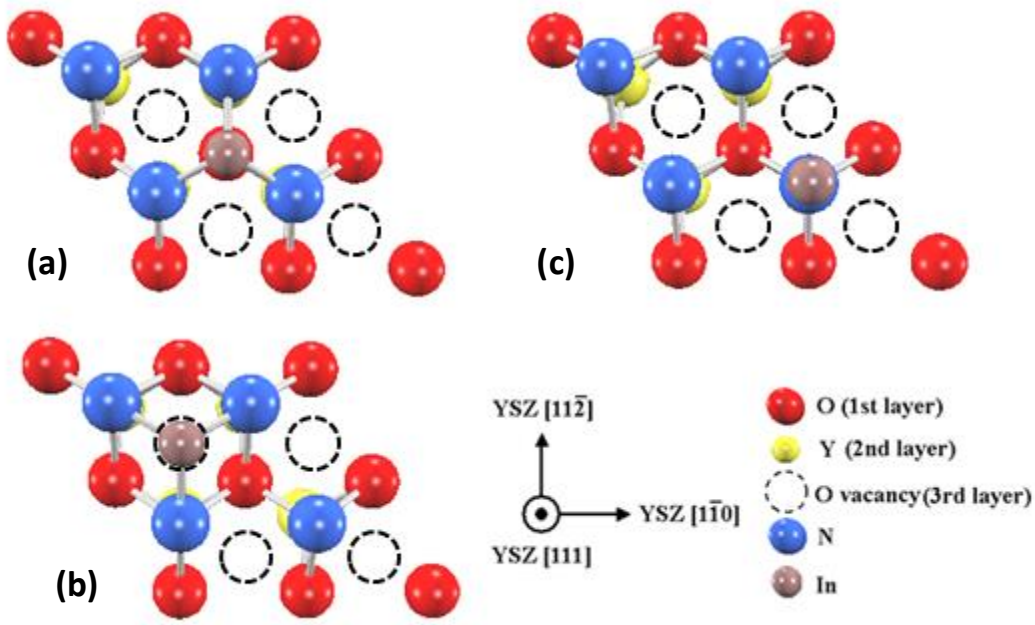

Fig. 4-6 Top views of In-polar InN (a) (b) and N-polar InN (c) on the Y-segregated slab.

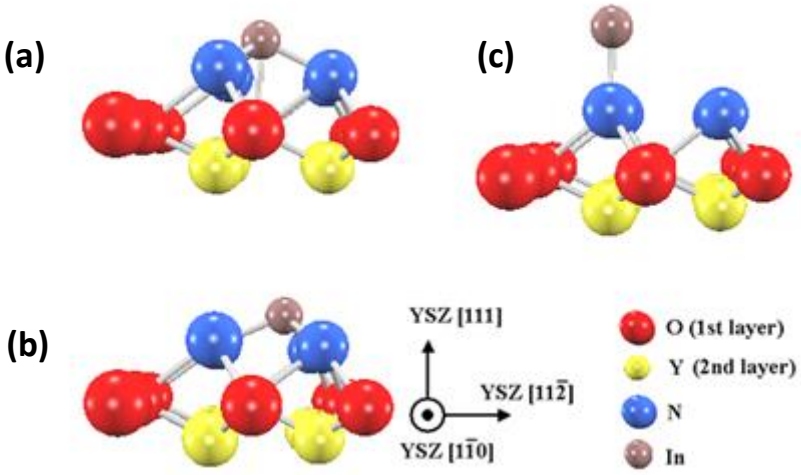

Fig. 4-7 Side views of In-polar InN (a) (b) and N-polar InN (c) on the Y-segregated slab.

To sum this up, in order to investigate the polarity determination of InN on YSZ substrates, six different InN/YSZ interface structures were prepared. For the segregation-free slab, two structures of In-polar and one for N-polar have been shown in Fig. 4-4 and 4-5. For the Y-segregated slab, there are also two structures of In-polar and one for N-polar showed in Fig. 4-6 and 4-7.

The investigations of In adsorption energies on the N layer covered slabs are carried out for the interface structures above. The results of the calculated adsorption energies for In-polar and N-polar structures on Y-segregated and Y-segregation-free YSZ (111) surfaces are summarized in table 4.2. The results reveal that the adsorption energy for In-polar InN on the Y-segregated YSZ surfaces is larger than that for N-polar InN on the Y-segregated YSZ surfaces. In the case of Y-segregated YSZ substrates, a growth of In-polar InN is dominant. On the other hand, the energy difference between In-polar and N-polar InN on the Y-segregation-free YSZ surfaces is quite small. This means the growth of In-polar InN, N-polar InN or mixture of In- and N-polar could happen on the Y-segregation-free substrates.

The results in table 4.2 are consistent with previously reported experimental data. For the Y-segregated YSZ substrates, growth experimental results [4.8] show that the growth of In-polar InN always occurs on the Y-segregated substrate. However, in case of a Y-segregation free YSZ substrate, In-polar InN, N-polar InN and mixture of In- and N-polar InN occurs [4.18]. After the comparison between the calculated adsorption energies in the experiment, the mechanism of InN polarity control on the YSZ substrate can be elucidated. As mentioned before, according to the definition of equation (4.1), the large adsorption energy for In atom means the In atom is stably adsorbed on the N layer covered slab. That is to say, larger adsorption energy means the interface structure is more stable. According to the calculated adsorption energies in table 4.2, In case of the Y-segregated YSZ slab, both the In-polar sites have larger adsorption energies than the N-polar site. This means the In-polar InN is energetically favorable to grow on the Y-segregated substrate. The possibility of N-polar InN growth on the

Y-segregated substrate is minimal. In the case of a Y-segregation-free slab, the energy difference between the In-polar InN and N-polar InN is less than 20 meV. From chapter 3 it is already known that the thermal energy during the InN growth is about 60 meV. For this reason, In-polar InN, N-polar InN and mixture of In- and N-polar InN occurs on the segregation-free YSZ substrate.

Table. 4.2 The adsorption energies of In on N-covering YSZ slabs in eV.

YSZ slab	Adsorption energy of indium		
	In-polar (a)	In-polar (b)	N-polar
Y-segregated	7.86	7.71	5.24
Segregation-free	3.29	3.28	3.27

4.2.2 DOS analysis of the InN/YSZ

In section 4.2.1, the adsorption energies are employed to elucidate the experimental results. The theoretical studies are quite consistent with the experiments. In this section, the DOS analysis will be carried out to investigate the mechanism of polarity determination.

As shown in Fig. 3-10, the difference between segregation-free and Y-segregated slabs is the Y atoms existed at the surface region. Hence, to clarify effects of yttrium segregations on the determination of the polarity, local DOS calculations for In, N, O, Zr and Y atoms will be performed.

As mention in table 4.2, the In-polar structures (a) and (b) on the Y-segregated slab has an absolute advantage over the other structures in adsorption energy. It is necessary to elucidate this large energy difference at first. The DOS analyses of In-polar (a) InN on both segregation-free and Y-segregated slabs are performed first. As shown in Fig. 4-8, the LDOSs of the In-polar InN on the Y-segregated surface (a) and on the Y-segregation free surface (b) are plotted. In case of the Y-segregated slab, it is found

that there is a clear hybridization between In5*s* and O2*p* around -5 eV and -3.7 eV. The hybridization between the N and O is obscure. In case of the segregation-free slab, no obvious hybridization between In5*s* and O2*p* is observed on the Y-segregation-free surface. Only the hybridizations between N and O can be found. These phenomena are likely caused by the difference of atomic arrangements between an In atom and an O atom. As shown in Fig. 4-4 (a) and 4-6 (a), for the In-polar InN on the Y-segregated surface, the In atom is on the top site of the oxygen. The In-O bond length is 2.5 Å. For the In-polar InN on the segregation-free surface, it is only 2.8 Å for the In-O bond. The short In-O bond could be the origin of hybridization between In5*s* and O2*p* on the Y-segregated surface in Fig. 4-8 (a).

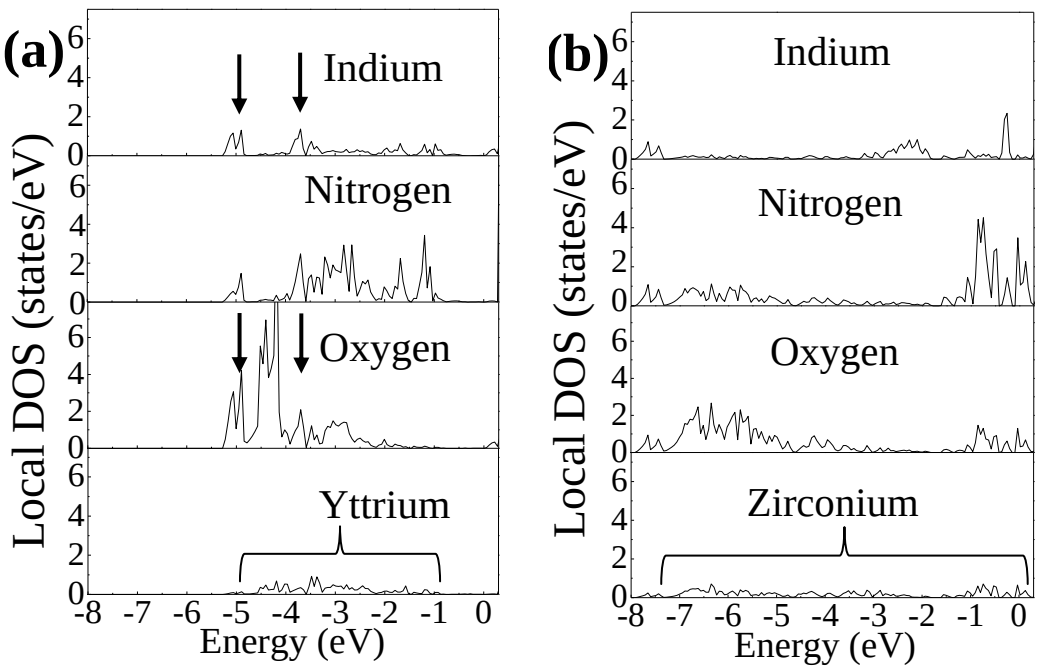

Fig. 4-8 Local DOSs for structures of an indium atom on the nitrogen layer covering (a) In-polar InN on Y-segregated and (b) In-polar Y-segregation free YSZ surfaces.

Further analysis reveals that in Fig. 4-8 (a) the hybridization between N2*p* and Y4*d* is quite small, ranging from -5 eV to -1 eV. On the other hand, the hybridization between N2*p* and Zr4*d* is clearly observed ranging from -8 eV to 0 eV on the segregation-free

slab in Fig. 4-8 (b). This difference is determined by the Y segregation at the surface region. Y segregations also play a crucial role in determining the polarity of InN. Therefore, it can be predicted that In-polar InN structure on the Y-segregated YSZ slab is stabilized by strong In5*s* and O2*p* hybridization caused by short In-O bond because of the Y segregation at the surface region.

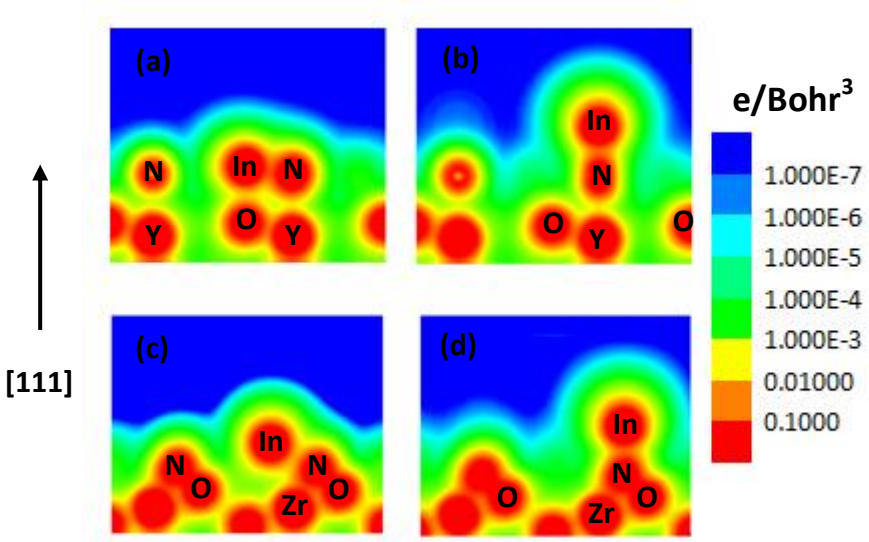

Fig. 4-9 The cross-sectional charge density maps of InN on YSZ substrates: (a) In-polar on Y-segregated slab (b) N-polar on Y-segregated slab (c) In-polar on segregation-free slab (d) N-polar on segregation-free slab.

The analysis of charge density is also carried out to investigate the In-polar structures on Y-segregated and segregation-free slabs. Fig. 4-9 shows us the cross-sectional charge density of In- and N-polar InN on Y-segregated and Y-segregation free slabs respectively. As shown in Fig. 4-9 (a) and (b), the charge densities in the space between the N and the surface O atoms are fairly low. In Fig. 4-9 (c) and (d), the charge densities in the space between the N and the surface O atoms are relatively high. These findings indicate the bonding of a N atom on the Y-segregated YSZ substrates is weaker than that on the Y-segregation free substrates. The result of charge density is quite consistent with the result of the adsorption energy. At the same time, for the In-polar

InN in Fig. 4-9 (a), the charge densities in the space between the In and surface O indicate the In-O interaction could be observed. Meanwhile for the other samples, no such direct In-O interaction can be found. Based on the charge density, it is known that the additional In-O bond stabilizes the In-polar structure on the Y-segregated slab.

In order to understand the charge distribution in the InN/YSZ system, the charge populations of the atoms are calculated based on the results of the Local DOS. The valence number for an atom can be obtained by subtracting the original valence electrons from the calculated charge population. The results are summarized in Table. 4.3.

Table 4.3 The valence number of the atom in the InN/YSZ system.

	In-polarity on Y-segregated surface	N-polarity on Y-segregated surface	In-polarity on zirconia surface	N-polarity on zirconia surface
In ($4d^{10}\ 5s^2\ 5p^1$)	Population: 11.29	Population: 11.54	Population: 11.46	Population: 11.49
	Transfer: +1.71	Transfer: +1.46	Transfer: +1.54	Transfer: +1.51
N ($2s^2\ 3p^3$)	Population: 5.4	Population: 5.52	Population: 5.43	Population: 5.78
	Transfer: -0.4	Transfer: -0.52	Transfer: -0.43	Transfer: -0.78

The results of charge transfers in table 4.3 can be employed to elucidate the polarity determination. For the charge transfer of the In atom, it is found that the In-polarity on Y-segregated slab has the larger value than the others. This means the In atom has a stronger interaction with the N-layer covered slab compared to other interface structures. This result agrees with the calculated adsorption energies. It can be predicted that the large charge transfer in the In atom could be employed to estimate the stability of the In-polar structure.

As mentioned in table 4.2, it is also found that there is only a small difference in adsorption energy between the In-polar (a) and (b) structure. Based on the atomic structure of the surface region, the difference will be elucidated. As shown in Fig 4-4 and 4-6, the difference between In-polar (a) and (b) is the relative position between

the In atom and the first layer O atom. In the case of the segregation-free slab, for In-polar (a), there is only one surface O atom (red) closed to the In atom. For the In-polar (b), there are two surface O (red) atom closed to the In atom. In-polar (a) has a shorter In-O bond than In-polar (b). In the case of the Y-segregated slab, for In-polar (a), the In atom is located in the middle of three oxygen vacancy (broken line) and lied on top of the surface O (red) atom. There will be a shorter In-O bond for In-polar (a) compared to In-polar (b). Shorter In-O bond will lead to larger adsorption energies. The In-O bond length are summarized in table 4.4.

Table 4.4 The In-O bond length (Å) of In-polar InN (a) (b) on segregation-free and Y-segregated slab. The atomic structures are shown in Fig. 4-4 and 4-6.

	In-polar (a)	In-polar (b)
Y-segregated	2.54	3.29
Segregation-free	2.38	2.80

For a better understanding of the effect of the dopant on the InN polarity, detailed investigations of the local DOSs of the N-polar InN on the two segregation-free and Y-segregated slabs were performed too. The results are summarized in Fig.4-10. For the Y-segregated slab in Fig. 4-10 (a), the hybridization between the In5*s* and O2*p* ranging from -4 eV to -1 eV is very strong. For the segregation slab in Fig. 4-10 (b), the hybridization between In and O is very weak.

As shown in Fig. 4-10, it is also found that the hybridization between N2*p* and Zr4*d* can be clearly observed ranging from -1eV to 0 eV. Contrary to this, the hybridization between N2*p* and Y4*d* is too small to be observed. Therefore, it can be predicted that the N-polar InN structure on the Y-segregated YSZ slab is also stabilized by strong In5*s* and O2*p* hybridization caused by short In-O bonds because of the Y segregation at the surface region.

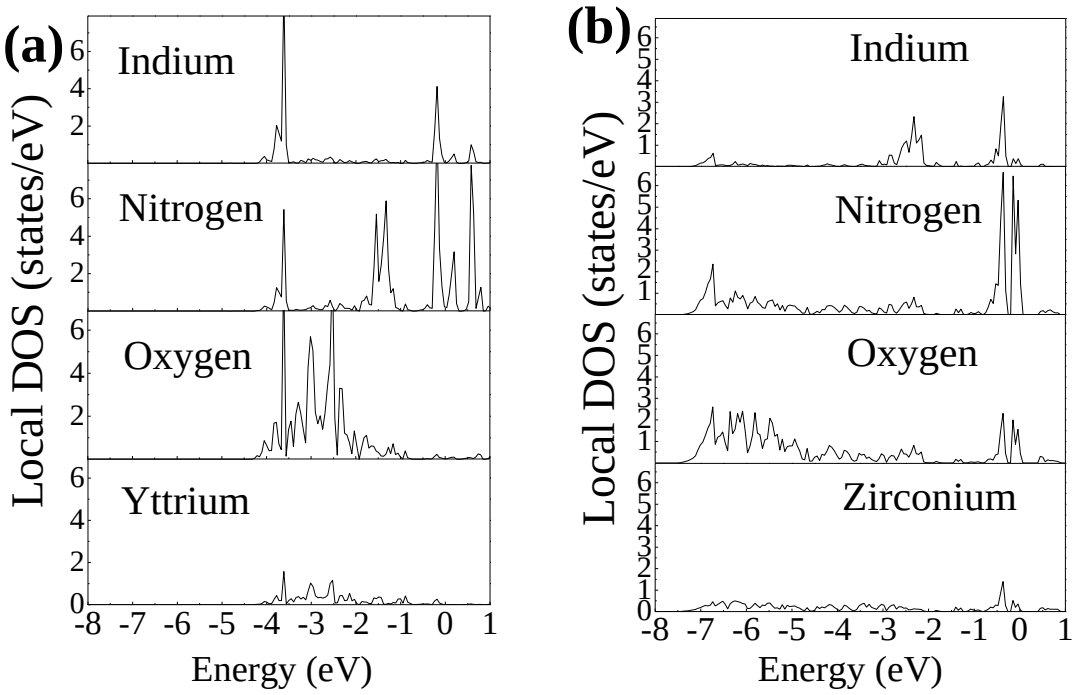

Fig. 4-10 Local DOSs for structures of an indium atom on the nitrogen layer covering (a) N-polar InN on Y-segregated and (b) N-polar Y-segregation free slabs.

To sum this up, because of the Y segregation on the surface region of YSZ (111), the polarity determination is totally different on the segregation-free and Y-segregated slabs. The Zr and Y have differences in the *d*-orbital valence electron. It can be predicted that the difference in d-orbital electron should be main reason to account for such significant changes for the polarity determination on YSZ substrates. The different *d*-orbital valence electrons of Zr and Y atoms will affect the adsorption of the N atom on the YSZ substrates. Moreover, the adsorption energy of In atom on the N layer covering YSZ substrates can depend on the strength of In5*s* and O2*p* hybridization caused by In-O bond length. To put this simply, the polarity determination is dependent on the surface segregated transition metals.

4.3 Summary

In this chapter, the mechanisms of the determination of InN polarity on YSZ (111) substrates were studied based on the theoretical calculations. It was found that the growth of In-polar InN on the Y-segregated YSZ surfaces is energetically more stable than that of N-polar InN. It indicates that In-polar InN is favorably grown on the Y-segregated YSZ substrate. On the contrary, the energy difference between In-polar and N-polar InN on the Y-segregation-free YSZ surfaces is quite small. It means that the mixture of In- and N-polar are possibly grown on segregation-free YSZ substrate. These results are consistent with the experimental results. A detailed analysis of the local DOS shows a clear hybridization between In5*s* and O2*p* on the Y-segregated surface. On the other hand, no hybridization between In5*s* and O2*p* is observed on the Y-segregation-free surface. These are attributed to the distance between an In atom and an O atom, and the hybridization between N2*p* and *d*-orbital metal cations. These results indicate that high quality In-polar InN films can grow on Y-segregated zirconia.

Reference

[4.1] T. Onozu, I. Gunji, R. Miura, S. S. C. Ammal, M. Kubo, K. Teraishi, A.Miyamoto, Y. Iyechika and T. Maeda, Jpn. J. Appl. Phys. **38**,2544 (1999).

[4.2] A. G. Bhuiyan, A. Hashimoto and A. Yamamoto, J. Appl. Phys. **94**, (2003).

[4.3] C. S. Gallinat, G. Koblm¨uller, J. S. Brown and J. S. Speck, J. Appl. Phys. **102**, 064907 (2007).

[4.4] G. Koblm¨uller, C. S. Gallinat and J. S. Speck, J. Appl.Phys. **101**, 083516 (2007).

[4.5] J. S. Park, S.-K. Hong Advances in Materials Research. **12**, 185 (2009).

[4.6] V. Ramachandran, R. M. Feenstra, W. L. Sarney, L. Salamanca-Riba, J. E. Northrup, L. T. Romano and D. W. Greve, Appl. Phys. Lett. **75**, 808 (1999).

[4.7] R. Collazo, S. Mita, A. Aleksov, R. Schlesser and Z. Sitar, J. Cryst. Growth **287**, 586 (2005).

[4.8] A. Kobayashi, K. Okubo, J. Ohta, M. Oshima and H. Fujioka, Phys. Status Solidi A **209**, 2251 (2012).

[4.9]T. D. Veal, P. D. C. King, P. H. Jefferson, L. F. J. Piper and C. F. McConville, Phys. Rev. B **76,** 075313 (2007).

[4.10] D. Muto, T. Araki, H. Naoi, F. Matsuda and Y. Nanishi, Phys. Status Solidi A **202,** 773 (2005).

[4.11] K. Okubo, A. Kobayashi, J. Ohta, H. Fujioka and M. Oshima, Appl. Phys. Express **4**, 091002 (2011).

[4.12] P. J. Schunck, M. D. Mason, R. D. Grober, O. Ambacher, A. P. Lima C. Miskys, R. Dimitrov and M. Stutzmann, Appl. Phys. Lett. **79**, 952 (2001).

[4.13] J. Ohta, H. Fujioka, M. Oshima, K. Fujiwara and A. Ishii, Appl. Phys. Lett. **83**, 3075 (2003).

[4.14] K. Okamoto, S. Inoue, N. Matsuki, T.-W. Kim, J. Ohta, M. Oshima, H. Fujioka and A. Ishii, Appl. Phys. Lett. **93**, 251906 (2008).

[4.15] Y. Takamura, Z. T. Wang, Y. Fujikawa, T. Sakurai, Q. K. Xue, J. Tolle, P.-L. Liu, A. V. G. Chizmeshya, J. Kouvetakis and I. S. T. Tsong, Phys. Rev. Lett. **95**, 266105 (2005).

[4.16] P.-L. Liu and K.-C. Liao, Scripta Materialia **68,** 211 (2013).

[4.17] Y. Oda and A. Ishii and K. Fujiwara e-J. Surf. Sci. Nanotech. **10,** 221 (2012).

[4.18] A. Kobayashi, personal communication of InN growth on YSZ (111) substrates.

Chapter 5 Theoretical study of InN/MnSZ system: a development of new substrate for InN growth

As mentioned before, YSZ substrate is a promising substrate for *c*-InN growth. Even so, a lattice mismatch of 2.3 % still exists between the YSZ substrate and the InN film. To solve this problem, other dopant atoms will be introduced in order to decrease the lattice mismatch. MnSZ has a small lattice constant and exhibits better lattice mismatch. MnSZ (111) is considered as a promising substrate for InN growth. In this chapter, theoretical study will be carried out to investigate the InN growth on the MnSZ substrate.

5.1 Development of new substrate for InN growth

In the first half of this thesis, the growth of InN on the YSZ (111) has been investigated. It has been demonstrated that YSZ (111) is a promising substrate for the epitaxial growth of InN due to the lattice mismatch of 2.3%. Since the lattice mismatch is so important to the growth of InN, the decrease in the lattice mismatch will lead to the improvement of the InN quality.

It is known that the lattice constant of the cubic zirconia is stabilized by dopants depending on the dopant materials. The ionic size and the valence number of dopant atoms are rather different to the Zr atom. On one hand, a dopant with a large ionic size will enlarge the lattice constant gradually as the dopant content increases. On the other hand, a small ionic size dopant will diminish the lattice constant as the dopant content increases [5.1].

It is already known that the lattice mismatch between InN (0001) and YSZ (111) is 2.3%. In order to reduce the lattice mismatch, a decrease in the lattice constant is required. Based on this point of view, in this chapter, in order to further improve the film quality of InN on the YSZ substrate, the development of a new substrate is

required. Here, new dopants will be introduced to replace the yttrium dopant in the YSZ. As a result, the lattice constant will decrease. The improved InN on lattice matched substrate can be expected.

Table 5.1 Ion radii (Å) of different dopants.

Sm^{3+}	Gd^{3+}	Y^{3+}	Yb^{3+}	Sc^{3+}	Mn^{3+}	Ca^{2+}
1.08	1.05	1.02	0.99	0.87	0.78	0.99
Al^{3+}	Ti^{3+}	V^{3+}	Cr^{3+}	Fe^{3+}	Ni^{3+}	Ce^{3+}
0.50	0.76	0.74	0.69	0.64	0.62	1.03

Table 5.1 shows us the ion radii of different dopants for zirconia. The dopants must be chosen carefully. Firstly, the ionic size of the dopant must be smaller than the Y^{3+}. Secondly, the dopant must have the ability to stabilize the cubic zirconia at room temperature. Mn^{3+} is found to satisfy the requirement above. The MnSZ will be chosen as the candidate substrate for InN growth.

5.2 Properties of MnSZ

The manganese trivalent cation is expected to behave like yttrium in the Mn-stabilized cubic zirconia. Mn has a smaller ion radius and can be used as a good candidate to stabilize the cubic zirconia. Firstly, it is theoretically possible that MnSZ can provide a better lattice matched substrate because its ionic radius is smaller than that of Y. Secondly, the studies show that cubic zirconia can be stabilized at room temperature by the introduction of Mn cation [5.2-5.8]. It was found that the Mn dopant dispersed uniformly in the MnSZ structure. It was also found that the lattice constant decreases as the Mn concentration is increased. The reports of the relation between Mn concentration and lattice constant are summarized in table 5.2. Experimental results demonstrate that Mn atoms can act the same as the yttrium dopant to stabilize the cubic zirconia structure.

As shown in table 5.2, a small lattice constant will be realized with high Mn dopant due to the small ionic radius. The lattice constant of MnSZ is a smaller lattice constant than YSZ. Therefore, MnSZ (111) could be a good candidate of the lattice-matched surface for c-plane InN growth. On the basis of the lattice constant in table 5.2, it is possible to estimate that the lattice mismatch between InN (0001) and MnSZ (111) is as small as 0.5%. Compared to the 2.3% lattice mismatch between InN and YSZ substrate, the lattice mismatch is reduced to a larger extent. Based on this point of view, it can be predicted that the InN film quality on MnSZ substrate will be better than that of the YSZ substrate.

Thermal expansion coefficient (TEC) of the substrates is also an important issue for the growth of nitride. The TEC of YSZ is summarized in chapter 1. In the case of the MnSZ, there are only few studies on the TEC of the MnSZ. It is found that the TECs of Mn-doped YSZ increased with Mn-content [5.4]. It can be expected that the TEC of MnSZ is higher than that of YSZ. The TEC mismatch is large for InN/MnSZ compared with InN/YSZ.

Table 5.2 Lattice constants (Å) of different kind cubic zirconia samples depend on Mn contents. (C: cubic phase M: monoclinic phase)

Mn (mole %)	Ref. 5.7	Ref. 5. 8	Ref. 5.9	Ref. 5.10
0	5.11-5.14 (M)	5.090 (C+M)	5.15 (M)	5.11 (C+M)
5		5.089 (C+M)	-	-
10	5.06-5.09 (C)	5.078 (C)	5.08 (C)	5.087 (C+M)
15		5.077 (C)	-	5.076 (C+M)
20		5.069 (C)	5.06 (C)	5.065 (C+M)
25		5.068 (C)	5.04 (C)	5.054 (C)
30		5.052 (C)	-	5.044 (C)

Even though MnSZ is a prime candidate to improve the lattice mismatch, it still faces the problem that there is no single crystal MnSZ substrate for InN growth at this time.

It is known that the MnSZ material could be fabricated by a sol-gel method and PLD growth method [5.7]. However, to our knowledge there are no reports of the MnSZ bulk substrates. The studies of zirconia substrates are mostly focused on the yttria-stabilized zirconia substrate. This means we cannot grow InN on MnSZ substrates via the experiments. Hence, theoretical study will be carried out to confirm the epitaxial growth of InN on the MnSZ substrate since the experiment is limited.

Although the research on the MnSZ substrate is missing, the novel properties of the MnSZ have drawn a lot of attention. Intensive studies have been performed to understand the properties of MnSZ [5.11, 5.12]. MnSZ is proposed as a ferromagnetic semiconductor with a Curie temperature above room temperature. Theoretical investigations are employed for the study of the ferromagnetic properties of MnSZ [5.13-5.15].

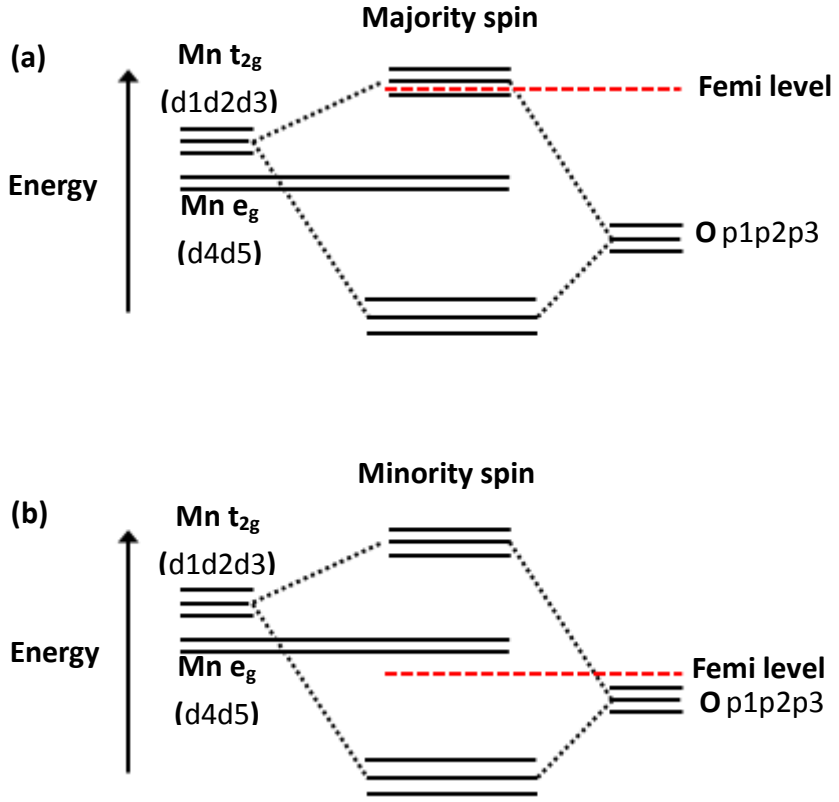

Fig. 5-1 Schematic description of the band splitting and p–d hybridization of Mn in O cubic field: (a) majority spin (b) minority spin.

Theoretical studies demonstrate half-metallic ferromagnetism (HMF) [5.16] in transition metal (TM) impurities-doped cubic zirconia such as the MnSZ [5.13, 5.17]. Ref. 5.17 shows the schematic representation of the band energy for MnSZ. Fig. 5-1 (a) shows us the majority spin and Fig. 5-1 (b) shows us the minority spin. The principal mechanism leading to the appearance of the half-metallic gap is the hybridization of the Mn 3*d* orbitals with O 2*p* orbitals [5.17].

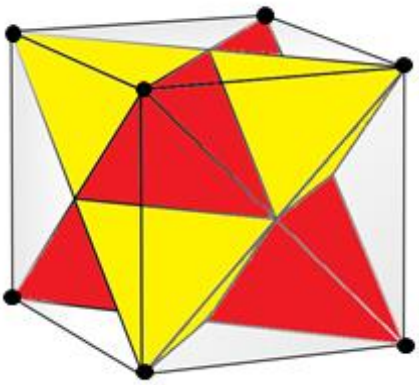

Fig. 5-2 Schematic picture of twofold tetrahedral field in the cubic structure.

For detailed information on the basis of the crystal field theory, Jia *et al*. [5.14] give us the formation mechanism of HMF in MnSZ. The schematic description of the band splitting and p–d hybridization of Mn in an O cubic field is shown in Fig. 5-1 [5.14]. The cubic field can be divided into a twofold tetrahedral (T_d) field as shown in Fig. 5-2. Therein, the *d* orbitals would split into higher triple-degenerated t_{2g} orbitals and lower double-degenerated e_g. According to the crystal field theory, in the T_d field, only the Mn-t_{2g} orbitals hybridize with neighbor O-*p*, while Mn-e_g almost keep unhybridized. The Mn-t_{2g} would further split into a couple of triple-degenerated bonding and antibonding *p*–*d* hybrids orbitals. The bonding *p*–*d* hybrids orbitals are mainly came from O-*p* while the antibonding ones came from Mn-t_{2g}. The Mn *d* orbitals are about 4.6 eV higher than the O *p* orbitals. When the Mn *d* hybridizes with O *p* orbitals, the lower hybridized t_{2g} orbitals would be dominated by the O *p* orbitals and the higher would be dominated by the Mn *d* orbitals. Mn in an O cubic field shows majority HMF,

the minority gap is formed by the Mn-e_g and the bonding *p–d* hybrids orbitals [5.14].

In case of Mn oxide, whether the on-site coulomb repulsive correction (+U) is employed or not requires careful discussions. The common feature after taking into account the on-site coulomb repulsive as well as exchange interactions is the enhancement in both the exchange splitting and the band gap of the oxides, especially when the value of U is a large one. It is well known that the band gaps of semiconductors are systematically underestimated by LDA or GGA. One of the reasons to utilize GGA+U instead of just GGA is to improve the value of the band gap towards the experimental value. The LDA+U is usually employed when the bandgap difference between the theoretical calculation and the experimental result is too large. Compared to the *ab initio* calculation (GGA, LDA), the +U method considered the effect of the experimental results and was taken as the phenomenological methods.

As was previous mentioned, the fundamental nature of MnSZ is far from being well understood. Neither the phenomenological model nor the *ab initio* calculation can successfully describe all the experimental findings. The key issue is the energy position of the 3*d* state of the magnetic Mn impurity. Even though the LDA has been added successfully to the calculation in Curie temperatures T_C of the dilute magnetic semiconductor (DMS), it tend to underestimate the localized character of the magnetic states. The LDA+U can form a bridge between the LDA and the phenomenological results. For example, S.Ostanin *et al*. described an extensive study of MnSZ using the well-established LDA and checked their conclusions with preliminary LDA+ U calculations [5.12]. They found that the effects of the LDA+U method combined with the CPA for the 25% MnSZ raised T_C by about 15%. Jia *et al*. [5.14] used the spin-dependent GGA for the exchange and correlation effects in their theoretical investigation.

On the basis of the previous reports, Mn-stabilized zirconia has been intensively studied as a spintronic material. However, as a lattice matched substrate for c-InN growth, the related investigations are still missing. In this chapter, a Mn-stabilized zirconia (111) surface is employed as a lattice matched substrate for InN growth.

Theoretical investigation is performed to confirm the feasibility of a MnSZ (111) surface as a lattice-matched substrate for InN growth.

5.3 Atomic structure of the MnSZ surface

As mentioned above, among the single crystal cubic stabilized zirconia substrates, only the YSZ substrate already existed. The phenomenon of Y segregation on the YSZ surface is investigated by both experiment and theoretical study. In the case of the MnSZ, there is less research on MnSZ compared to YSZ. Therefore, the atomic structure of the MnSZ surface region is still unclear. To investigate the growth mechanism of InN on the MnSZ substrate, the understanding of the surface structure is required. In this section, the atomic structure of the surface region will be discussed.

Dopant segregation in zirconia has been investigated by theoretical and experimental studies. For the experimental studies, in the case of the Y dopant, the phenomena of Y segregation both in the grain boundary and surface is confirmed by XPS, LEIS and secondary ion mass spectrometry (SIMS). In the case of the other dopants, the Mn segregation at the grain boundary is reported [5.6]. Furthermore, it is reported that segregation at the grain boundaries and free surfaces showed the same enrichment levels [5.18]. The Ti segregation in Ti-doped zirconia and Ce segregation in Ce-doped zirconia are also confirmed [5.18]. The thickness of the segregation layer for all the samples are 2-4 nm.

For the theoretical studies, in the case of Y dopant, the DFT calculations were performed to investigate the segregation of Y in the YSZ (111) surface. It was found that the Y atoms are energetically favorable at the top layers (up to 5 Å) [2.10]. For other dopants, segregations of Ce and Ti have also been confirmed by theoretical investigation [5.19, 5.20].

According to the above results, it can be predicted that the dopant segregation is a common phenomenon in the zirconia. The process of segregation is driven by the reduction of the surface free energy. One reason for the reduction of energy is the

relaxation of the elastic strain [5.21]. The elastic strain of the system is due to the size mismatch between the dopant and the Zr atoms. It can be reduced if dopant ions segregate to the surfaces because more free volume is available at the surface. The other reason is the formation of a space-charge region at the surface [5.22]. Oxygen vacancies and accumulation of the dopants at the surface region will have a space charge effect. This will reduce the surface energy.

As to the atomic structure of the surface region, in the case of the YSZ (111), a sandwich-type surface structure has been established based on experiment results. The first region is 5 Å thick and enriched in yttria. The second region is 60 Å thick and is depleted in yttria. The third region is the bulk structure. As mentioned in chapter 3 and 4, the computational slab model of the YSZ (111) surface is employed on the basis of the previous reports. The results of the theoretical study are quite consistent with the experiment. The growth mechanism of InN on the YSZ substrate has been successfully elucidated.

It is already known that the Y dopant segregation exists at the YSZ surface. However, for the Mn doped YSZ, there are only a few reports about the Mn segregation. D. Pomykalska *et al*. have investigated the MnO-Y_2O_3-ZrO_2 solid solution and made discoveries about the Mn segregation at the grain boundary [5.21]. S. K. Srivastava *et al*. have also found the grain boundary region is poor in Zr and Y but rich in Mn and O elements [5.6]. For the pure MnSZ, Zhao *et al.* have found separated crystalline MnO_x phases become apparent in the MnO-ZrO_2 binary oxides powders, which indicates the segregation of the Mn [5.22]. Due to the experimental results above it can be predicted that the Mn could be segregated at the MnSZ surface the same as the YSZ.

Table 5.3 Bond strength in eV/mol for Zr-, Y- and Mn-O.

	Zr-O	Y-O	Mn-O
Bond strength	7.85 ± 0.4	7.02 ± 0.2	4.16 ± 0.3

It is known that the difference between the enthalpic driving forces for surface segregation play a role in the disparate segregation trends [5.23, 5.24]. Table 5.3 shows us the bond strength of Zr-O, Y-O and Mn-O [5.25]. In the case of the YSZ, the Zr-O bond is stronger than the Y-O bond. This trend can be explained in terms of the more covalent character of the metal–oxygen interaction for Zr than for Y [5.23]. As mentioned before, the most stable termination for the YSZ (111) surface is the O-termination. It will involve the breaking of some metal–oxygen bonds. The unsaturated coordination should be more easily accommodated by Y cations than by the more covalent Zr cations. It is energetically favorable for the yttrium dopant to segregate to the surface rather than the Zr ions. Based on this point of view, in the case of the MnSZ surface, because the Mn-O is weaker than the Zr-O, it will favorable for Mn dopants to segregate to the surface layer too. Therefore, for the MnSZ surface slab, a sandwich-type structure similar with the YSZ surface will be employed as a Mn-segregation (111) surface.

5.4 Adsorption energies of N and In on MnSZ (111)

As mentioned before, MnSZ is a promising candidate for InN growth due to the small lattice constant compared to YSZ. However, unlike the YSZ substrate, the problem is that there is no single crystal MnSZ substrate for InN growth now. At the same time, theoretical study can be carried out to investigate the film growth when the experimental study is limited. Therefore, theoretical study will be employed to solve the problem.

The initial stage of the InN growth on MnSZ substrate is still not clear due to these reasons above. As mentioned in chapter 3, theoretical study can provide a useful tool to understand the initial stage of growth. In this section, since the experiments of InN growth on MnSZ (111) substrates are limited, theoretical calculation will be employed to investigate the events. To confirm the feasibility of the InN grown on the MnSZ substrate, the adsorption energies of In and N atoms on the MnSZ (111) surface will be

investigated.

For the comparison between the YSZ and the MnSZ surface in the next step, the same computational parameters have been chosen for the study of MSZ. The energy calculations and geometry optimizations were carried out within the framework of density-functional theory (DFT) with the generalized gradient approximation (GGA). Wavefunctions were expanded in a plane-wave basis set with a cut-off energy of 60 Ry. Ultrasoft pseudopotentials are used and electron configurations of pseudopotentials for In, N, Zr, Mn and O are $4d^{10}5s^{2}5p^{1}$, $2s^{2}2p^{3}$, $4s^{2}4p^{6}4d^{1}5s^{2}$, $3d^{5}4s^{2}$, and $2s^{2}2p^{4}$ respectively.

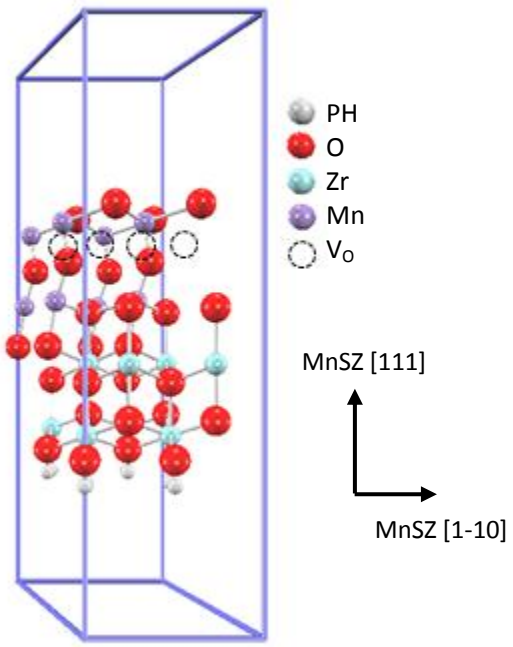

Fig. 5-3 Atomic structure of the MnSZ (111) slab.

Atomic structure of the MnSZ (111) slab is shown in Fig. 5-3. The same as the YSZ surface, Zr atoms are replaced with Mn atoms in the upper half of the zirconia (111) surfaces. It is treated as Mn-segregated substrates. The slab of MnSZ (111) contains 12 layers. It includes four sets of O-Mn (or Zr)-O (or V_O) trilayers. The process of surface relaxation will be carried out to get the optimized surface structure.

In this optimization process, the layers on the bottom O-Zr-O trilayer are fixed at bulk

positions and the top nine layers are fully relaxed with a convergence criteria of 0.05 eV/Å. Vacuum layers with the thickness of 15 Å are inserted to eliminate interactions between the adjacent slabs. The dangling bonds on the bottom of the slab are also terminated by the pseudohydrogens.

As shown in Fig 5-3, both Mn and O vacancies are enriched on the top surface layers. The atomic structure of the MnSZ surface region after realization is very different compared to that of the YSZ surface. The difference can be attributed to the segregated dopants of Mn and Y. According to the previous study in chapter 3, it is known that the first and second layers of the surface greatly affect the adsorption process. Because the atomic structure of surface region has changed so much, a change in the adsorption energy can be expected.

The adsorption energies of In and N atoms on the MnSZ surfaces are studied to investigate growth mechanism of InN on MnSZ (111) substrates at the initial stage. The adsorption energy $E_{adsorption}$ is defined as

$$E_{adsorption} = E_{substrate} + E_{adatom} - E_{total}. \qquad (5.1)$$

Here E_{total} is the energy of the MnSZ substrate with an adatom adsorbed on it. $E_{substrate}$ is the energy of the MnSZ substrate without the adatom. E_{adatom} is the energy of an isolated adatom. According to the definition of eq. 5.1, $E_{adsorption}$ indicates a positive value in general. The larger value corresponds to more stable adsorption.

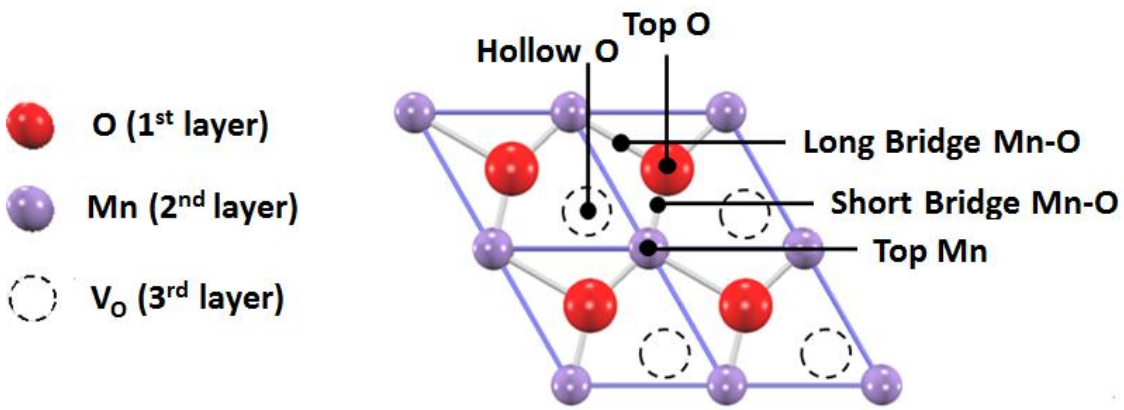

Fig. 5-4 Symmetry adsorption sites on 2×2 MnSZ (111) surface.

The high symmetry sites are selected based on the relative positions of first layer O

and second layer Mn in the MnSZ (111) surface. Five adsorption sites on the MnSZ (111) surface are shown in Fig. 5-4. They are top O site, top Mn site, hollow site, long bridge O-Mn site and short bridge O-Mn site. The results of the adsorption energy are summarized in the table 5.4.

Table 5.4 Adsorption energies (eV) on the Mn-segregated slab surface.

Atom	Adsorption site				
	Top O	Top Mn	Long Bridge Mn-O	Short Bridge Mn-O	Hollow
In	1.13	0.86	1.11	1.06	1.18
N	1.62	1.52	2.34	2.63	1.22

As shown in table 5.4, it is found that the N atom has a large adsorption energy than In on the MnSZ surface indicating that the N is more stable than In at the initial stage of InN growth. The differences in adsorption energies of In atom at various sites are less than that of the N atom. This indicates the migration of In atoms occurs more easily compared to N atoms.

In chapter 3 and 4 it is known the result that the N is more stable than the In atoms on both the cubic zirconia and Y-segregated zirconia surface because the adsorption energy of nitrogen on them is larger than indium. The results are the same in the case of the Mn-segregated surface. Here it can be summarized and concluded that the initial stage of InN growth on the cubic stabilized zirconia is the same as the segregated dopants. Nitrogen atoms are always more stable on the surface than indium atoms. At the same time indium atoms easily migrate on the surface.

Compared with the adsorption energies on YSZ and segregation-free slabs, it can be concluded that the MnSZ surface has the largest adsorption energies for both N and In atoms among the three slabs. As mentioned in chapter 3, it is known that there is a strong hybridization between Zr and N and a weak hybridization between Y and N. The adsorption energies seem to depend on the strength of the metal-N hybridization. Since the MnSZ has the largest adsorption energy, it can be predicted that there will be

a much stronger N-Mn hybridization than that of the N-Zr bond.

Based on the calculated adsorption energies, it is known that nitrogen is more stable than indium at the initial stage of growth. This indicates the first layer should be a nitrogen layer for the InN growth. The interfacial structure of InN/MnSZ and the epitaxial relationship can be obtained as InN [0001] // MnSZ [111] and InN (11-20) // MnSZ (1-10). The results are quite similar with the results on YSZ and segregation-free surface in chapter 3. The epitaxial growth of InN on the MnSZ surface is confirmed through the theoretical study. It can be expected that InN can epitaxially grow on the MnSZ substrate as well as YSZ. The MnSZ can provide a lattice matched surface for InN growth.

The N atom adsorption on the segregation-free, Y- and Mn-segregated substrates will be discussed from the aspect of bond lengths. The bond lengths of N-O and N-metal are summarized in Table 5.5. It can be seen that N atom adsorbed on the Mn-segregated zirconia surface have the largest adsorption energy and shortest bond length. On the other hand, N atom on the Y-segregated zirconia surface have the smallest adsorption energy and longest bond length. The stronger metal-N interaction at the surface will lead to a large adsorption energy and shorter bond length.

Table 5.5 Bond length (in Å) of N atom on MnSZ, YSZ and cubic zirconia surfaces.

Surface	Bond length	
	N-O	N-metal (Mn, Zr, Y)
MnSZ	1.39	1.80
Segregation-free	1.46	2.11
YSZ	2.99	2.70

Since the greatest difference among the three slabs is the metal atom exist at the surface region, the adsorption energies differences should be mostly originated from

this. For a better understanding of the relationship between the N adsorption energy and the segregated transition metal atoms at the surface region, the analysis of the local DOS will be performed for the N adsorption on the segregation-free, Y-segregated and Mn-segregated surfaces, respectively (Fig. 5-5).

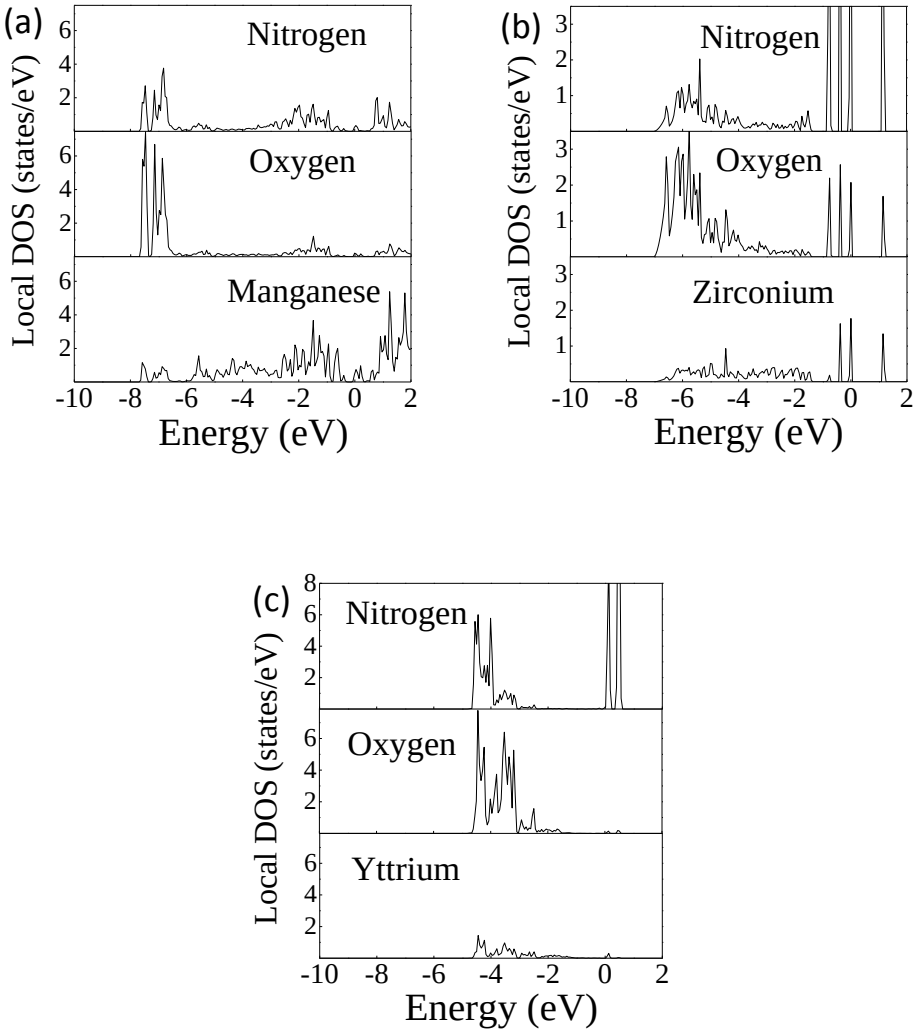

Fig 5-5 LDOSs of N adsorption on (a) MnSZ, (b) segregation-free and (c) YSZ surfaces.

According to the results of the LDOSs, it can be found that the MnSZ surface has the strongest hybridization between Mn 3*d* and N2*p* among the three samples. On the other hand, on the Y-segregated surface the hybridization between Y4*d* and N2*p* is the weakest. It is confirmed that the N atom has the strongest interaction with the MnSZ

surface due to the strongest hybridization between Mn and N. However for the YSZ surface, the N atom has a weaker interaction with the substrate because the N-Y hybridization is so weak. These results can explain why the adsorption energies are different on the three slab models. It is also found that In adsorption follows the same trend as N. The adsorption energies for In on three surfaces follow the same rules too. Fig. 5-6 shows the LDOSs of the In adsorption on MnSZ, segregation-free and YSZ slabs. The segregated transition metal atoms affect the adsorption of In through the hybridization too. Hence, the segregated metal atoms on the surfaces will affect the adsorption energies for both In and N.

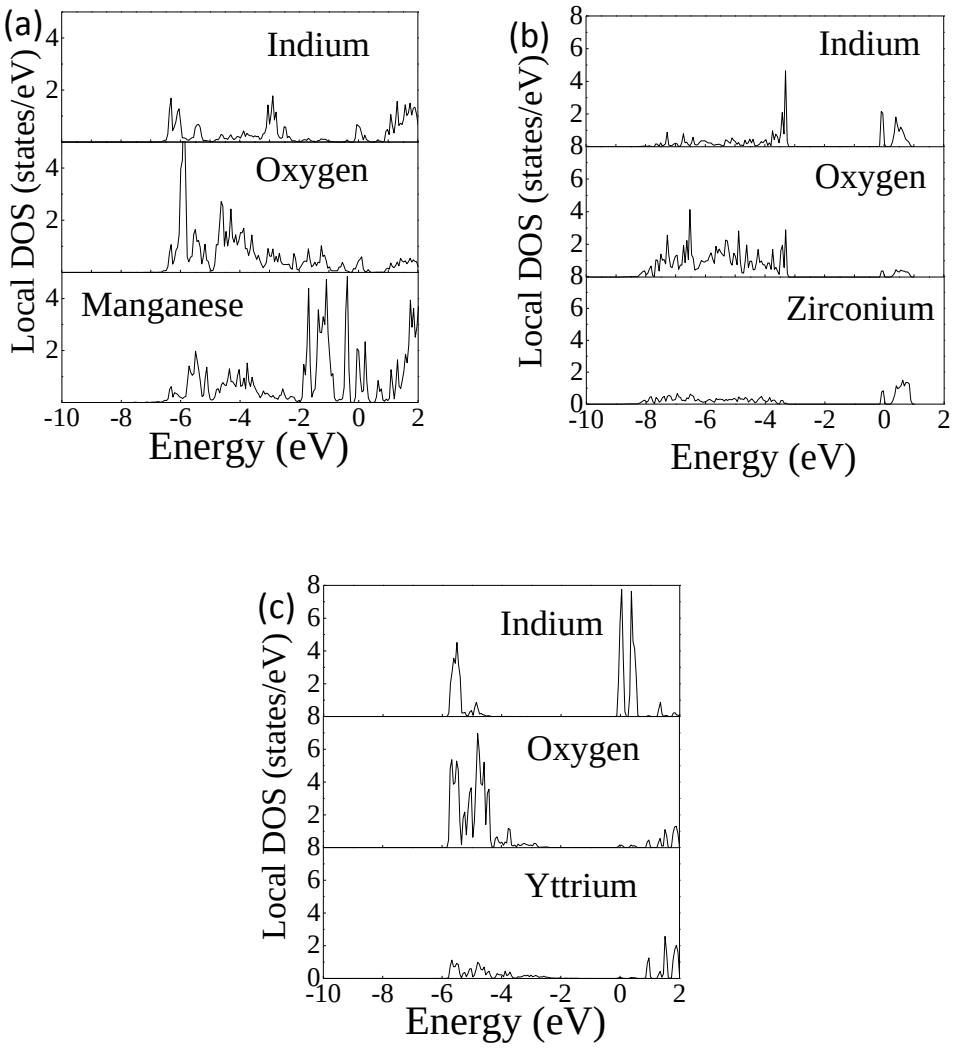

Fig 5-6 LDOSs of N adsorption on (a) MnSZ, (b) segregation-free and (c) YSZ surfaces.

It is already known that the adsorption energy is mostly by the interaction between the adatom and the first two layer of the surface slab. At the same time, the most difference is the metal atoms on the second layer on the surface. By comparison, it is known that the unfilled *d*-orbital of the Zr, Y and Mn are so different. For Mn the number of *d*-electrons in the unfilled orbital is five. On the other side there is only two d-electrons for Zr and one d-electron for Y. It can be expected that a large number of *d*-electrons dopant will lead to the large adsorption energy because the hybridization is enhanced.

As mentioned in Fig. 5-5 and 5-6, in the case of MnSZ slab, the LDOS is governed by strong hybridization at lower energy to -8 eV. The hybridization region is the widest among the three slabs. On the other hand, hybridization in the LDOS for YSZ slab only extended to -5 eV. This hybridization region is the narrowest among the three slabs. Since the band structure for the surface region varies greatly due to the dopant segregation, LDOSs for the atoms at the bulk region for the MnSZ, zirconia and YSZ are performed to validate the investigations.

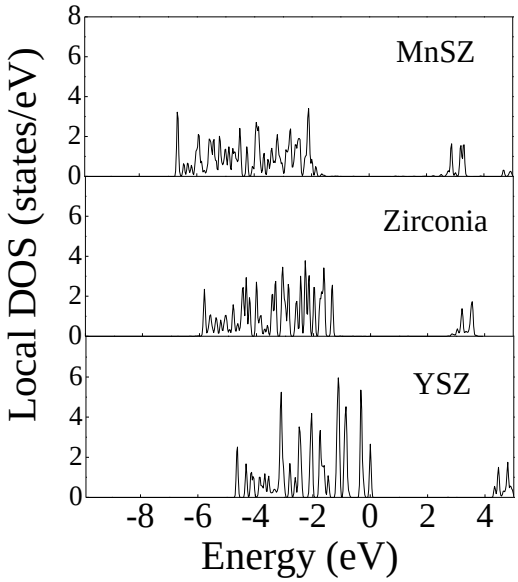

Fig. 5-7 Local DOSs of the O atoms at the bulk position for MnSZ, zirconia and YSZ slabs

Fig. 5-7 shows the LDOSs of the bulk O atoms for MnSZ, zirconia and YSZ slabs. It is

found that the widths of the valence band O2*p* are the same for all the three slabs. The LDOS for MnSZ shifts to the lower energy level and the LDOS for YSZ shifts to the higher energy level. The shift of the LDOS can be attributed to the effects of the dopants at the surface region.

5.5 In adsorption on N-covering MnSZ substrates

Based on the calculated adsorption energy, the polarity of InN on the MnSZ surface will be discussed.

To investigate the relative stability of In-polar InN and N-polar InN on MnSZ (111) substrates, calculations of the adsorption energies of an indium atom on the nitrogen layer covering MnSZ (111) surfaces were performed. An indium atom sited on top of a nitrogen atom is defined as N-polarity InN. On the other hand, an indium atom sited on the center of three nitrogen atoms is defined as In-polarity InN. The top views of In- and N-polar on the MnSZ (111) surfaces are shown in Fig. 5-8.

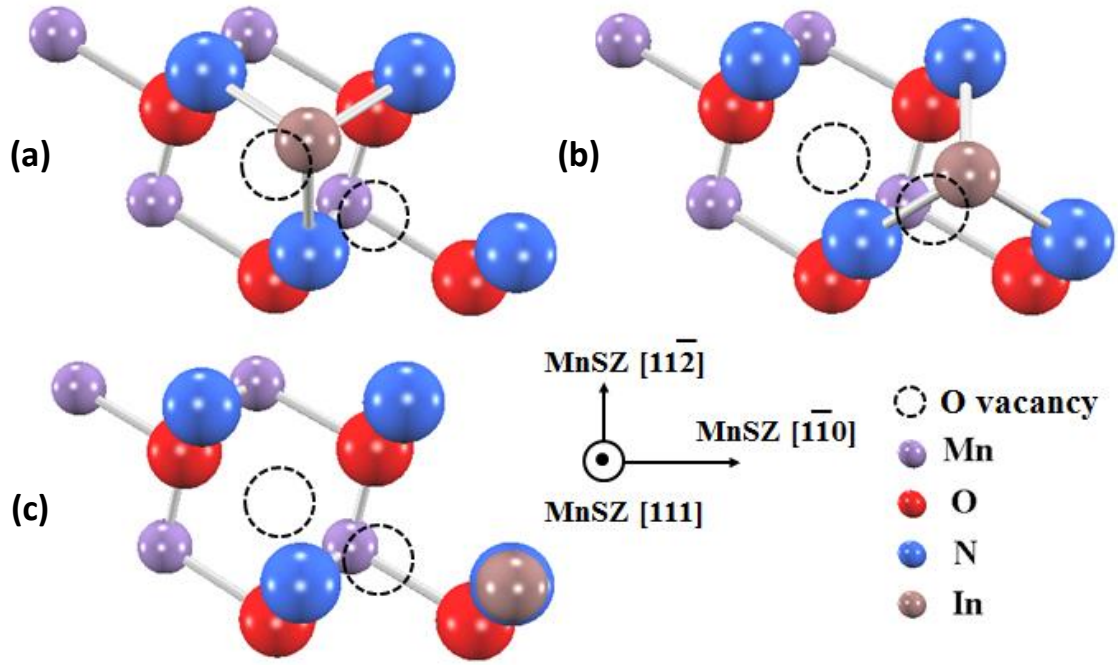

Fig. 5-8 Top views of In-polarity (a) (b) and N-polarity (c) InN on MnSZ (111) slab.

The adsorption energies of an indium atom on the nitrogen layer covering MnSZ (111) surfaces could be calculated by:

$$E_{adsorption} = E_{nlayer/substrate} + E_{In} - E_{total}. \qquad (5.2)$$

Here E_{total} is the energy of an In adsorbed on N layer-covering MnSZ slab. $E_{nlayer/substrate}$ is the energy for the N layer-covering MnSZ slab without In. E_{adatom} is the energy for an isolated In atom.

The results of the adsorption energies for In- and N-polar structures on MnSZ (111) surfaces are summarized in Table 5.6. The results reveal that the adsorption energy of In-polar InN is larger than the N-polar InN, which indicates the In-polar InN is more favorably grown on the MnSZ surface. With the help of Boltzmann distribution, the proportion of the In-polar and N-polar InN during the growth can be roughly estimated. According to the results it is known that the In-polar InN should predominantly grow on the MnSZ substrates without a mixture of In-polar and N-polar InN. This means on the Mn-segregated zirconia surface the pure In-polar InN can be grown and the mixture of In- and N-polar can be prevented.

Table 5.6 Adsorption energies (in eV) of an In atom on the nitrogen layer covering MnSZ (111) surfaces.

Substrate	Adsorption energy of indium		
	In-polar(a)	In-polar(b)	N-polar
MnSZ	3.37	3.35	3.28

From chapter 4, it is already known that surface segregated Y atoms will stabilize the In-polar InN structure in the case of the YSZ. On the other hand, the In adsorption energies of In-polarity and N-polarity are almost the same on the segregation-free

surface. With the addition of the results on the MnSZ surface, the polarity determination of InN on zirconia will be discussed on the three types of zirconia substrates: segregation-free, YSZ and MnSZ.

Table 5.7 shows us the bond length of the In atom for the In-polar structure on three different zirconia surfaces. For the YSZ surface the In atom has the most stable adsorption energy. At the same time, the In atom has the shortest In-N and In-O bonds compared with the other two slabs. These results are quite consistent with the calculated adsorption energies. In-polar InN is extraordinary stable when the yttrium atom is segregated at the zirconia surface. For the segregation-free and MnSZ slabs, the long bonds indicate the weak interaction between the In atom and the N-covered surface.

Table 5.7 Bond length (in Å) of In-polar structure In atom on MnSZ, YSZ and cubic zirconia surfaces.

	MnSZ	Segregation-free	YSZ
In-N	2.65	2.38	2.12
In-O	3.42	3.42	2.54

From the aspect of the atomic structure, as mentioned in chapter 4, the In-polar structure on the Y-segregated surface was energetically stable because the In atom is in the middle of three N atoms and right on the top of the surface O atom. This highly symmetrical site will lead to the smallest In-O bond. The indium atom not only makes bonds with three nitrogen atoms but also makes a bond with an oxygen atom just below itself. On the contrary, for the In-polar structure on the segregation-free and MnSZ surfaces, the In atom is in the middle of three nitrogen atoms, which is the same as the structure on the Y-segregated surface. The difference is the relative position of In and O atoms. In Fig. 5-8, it can be clearly seen that the In atom is not on the top of one oxygen atom but on the hollow site of the oxygen atoms. As a result, In-O bonds on segregation-free and MnSZ slabs are prolonged and the bonding energy is weakened compared with In-O bond on YSZ. This could be the reason why the adsorption

energies of In atoms on both MnSZ and segregation-free surfaces are smaller than that of the Y-segregated surface. The hybridizations between In and O on the MnSZ and segregation-free surfaces are so weak compared with the Y-segregated surface. Therefore, it can be predicted that the atomic structure could be an important reason why the In atom was stable on the Y-segregated surface.

So far, theoretical study has been employed to investigate the growth mechanism of InN growth on the MnSZ substrate. Also, the initial growth stage and the epitaxial growth has been confirmed by the adsorption energy on the MnSZ surface slab. Furthermore, the polarity determination of InN on MnSZ (111) surface was also investigated. It is found that In-polar is favorable on the Mn-segregated surface compared to the segregation-free surface. Based on this point of view, the Mn-segregation substrate can be employed to avoid the mixture of In- and N-polar InN growth. At last, only In-polar InN will be grown on the Mn-segregated substrate. The uniform In-polar film is very important to fabricate high performance InN-based devices.

5.6 Summary

In this chapter, to confirm the feasibility of the epitaxial growth of InN growth on the MnSZ (111) substrate, theoretical study was employed to investigate the initial stage of InN growth on the MnSZ surface. The adsorption energies of one In and N atoms on the MnSZ (111) surfaces were investigated. According to the results, it was found that nitrogen has larger adsorption energy on MnSZ surface than indium, indicating that the adsorption of N atom is more stable at the initial stage of InN growth. On the other hand, small differences in the adsorption energies of In atoms on various adsorption sites indicate that the migration of the indium atoms on MnSZ (111) surfaces occurs readily. The results also suggest that the first layer of InN films consist of a N layer which leads to epitaxial relationships between InN (0001) // MnSZ (111) and InN [11-20]

// MnSZ [1-10]. This alignment makes the lattice mismatch between InN and MnSZ as small as 0.5%. In addition, a local density of states (DOS) analysis revealed that the hybridization effect between the N2*p* and Mn3*d* orbitals plays a crucial role in determining the interface structure for the growth of InN on MnSZ (111) surfaces. Furthermore, it was found that an In atom preferentially adsorbs at the center of three nitrogen adatoms on the MnSZ substrate, which results in the formation of In-polarity InN. Preferential formation of In-polar InN is advantageous for device applications.

Reference

[5.1] D. W. Strickler and W. G. Carlson, J. Am. Ceram. Soc. **48**, 286 (1965).

[5.2] J. Zippel, M. Lorenz, A. Setzer, G. Wagner, N. Sobolev, P. Esquinazi and M. Grundmann Phys. Rev. B **82**, 125209 (2010).

[5.3] N.-H. Hong, C.-K. Park, A. T. Raghavender, O. Ciftja, N. S. Bingham, M. H. Phan and H. Srikanth, J. Appl. Phys. **111**, 07C302 (2012).

[5.4] M. Mori, T. Abe, H. Itoh, O. Yamamoto, G. Q. Shen, Y. Takeda, N, Imanishi, Solid State Ionics **123**, 113 (1999).

[5.5] G. Clavel, M. G. Willinger, D. Zitoun and N. Pinna, Eur. J. Inorg. Chem. **2008,** 863 (2008).

[5.6] S. K. Srivastava, P. Lejay, B. Barbara, O. Boisron, S. Pailhès and G. Bouzerar, J. Appl. Phys. **110**, 043929 (2011).

[5.7] J. Zippel, M. Lorenz, J. Lenzner, M. Grundmann, T. Hammer, A. Jacquot and H. Bottner J. Appl. Phys. **110**, 043706 (2011).

[5.8] A. Keshavaraja and A. V. Ramaswamy, J. Mater. Res. **9**, 837 (1994).

[5.9] J. I. Gutiérrez-Ortiz, B. de Rivas, R. López-Fonseca, S. Martín, J. R. González-Velasco, Chemosphere **68**, 1004 (2007).

[5.10] M.A. Schubert, S. Senz and D. Hesse, Thin Solid Films **517**, 5676 (2009).

[5.11] S. Chang and R. Doong, J. Phys. Chem. B, **108**, 18098 (2004).

[5.12] J. H. Tian, B. C. Liang, Y. Wang and S. F. Li, J. Electroanal. Chem. **526**, 36 (2002).

[5.13] S. Ostanin, A. Ernst, L. M. Sandratskii, P. Bruno, M. Dane, I. D.Hughes, J. B. Staunton, W. Hergert, I. Mertig and J.Kudrnovsky, Phys. Rev. Lett. **98**, 016101 (2007).

[5.14] X. Jia, W. Yang, M. Qin and J. Li, J. Magn. Magn. Mater. **321**, 2354 (2009).

[5.15] J. Yu, L. Duan, Y. Wang and G. Rao, Physica B **403**, 4264 (2008).

[5.16] R. A. de Groot, F. M. Mueller, P. G. van Engen and K. H. J. Buschow, Phys. Rev. Lett. **50**, 2024 (1983).

[5.17] T. Archer, C. Das Pemmaraju and S. Sanvito, J. Magn. Magn. Mater. **316**, 188 (2007).

[5.18] G. S. A. M. Theunissen, A. J. A. Winnubst and A. J. Burggraaf, Journal of Materials Science **27**, 5057 (1992).

[5.19] S. Gennard, F. Cora and R. A. Catlow, J. Phys. Chem. B **103**, 10158 (1999).

[5.20] H. R. Chauke, P. Murovhi, P. E. Ngoepe, N. H. de Leeuw and R. G. Crespo, J. Phys. Chem. C, **114**, 15403 (2010).

[5.21] H. B. Lee, F. B. Prinz and W. Cai, Acta Materialia **58**, 2197 (2010).

[5.22] Q. Zhao, W. Y. Shih, H.-L. Chang and W.-H. Shih, Ind. Eng. Chem. Res. **49**, 1725 (2010).

[5.23] R. Grau-Crespo, N. H. de Leeuw, S. Hamad and U. V. Waghmare, Proc. R. Soc. A **467**, 1925 (2011).

[5.24] T. Tauer, R. O'Hayre and J. W. Medlin, J. Mater. Chem. A **1**, 2840 (2013).

[5.25] J. F. Shackelford and W. Alexander, Materials science and engineering handbook (2001).

Chapter 6 Conclusions and Outlook

6.1 Introduction

InN has the highest electron mobility and saturation velocity among the group-III-nitrides. These excellent transport properties make it a promising candidate for high speed electron device applications. High crystalline quality InN film is required since the transport property could be greatly affected by the threading dislocation density. However, the growth of high quality InN suffers from a lack of suitable foreign substrates. Until now the most used substrates for InN growth always have large lattice mismatches. Hence, the development of new substrates with small lattice mismatches with InN is highly required. Fortunately, the cubic stabilized zirconia (111) surfaces are found to provide the lattice matched surfaces for hetero epitaxial growth of *c*-InN because it shares a threefold rotational symmetry with the InN c-plane and possibly gives a small lattice mismatch. In fact, the experiments of InN growth on yttria stabilized zirconia (YSZ) (111) substrates are already reported. In spite of the developments on InN growth, further improvements of the InN film quality on zirconia substrate is still required to give full access to its superiors transport properties.

It is known that the understanding of the mechanism of InN growth on the zirconia substrates is inherently important to the film growth itself. Based on this mechanism we can optimize the growth and improve the film quality at last. Today the growth mechanism for the *c*-InN growth on zirconia (111) is not clearly understood because the experimental technology is limited. Meanwhile the theoretical study of the novel InN/zirconia system is still missing. For these reasons, in this work the first principles calculations are employed to investigate the growth mechanism of InN on zirconia surfaces. The theoretical study can provide a useful tool to investigate the film growth at the atomic scale.

In this doctoral thesis, first principles calculations are employed to investigate the

initial stage of InN film growth and the polarity determination of the first InN monolayer on three different kinds of zirconia surface: the pure zirconia (111) surface, the YSZ (111) surface and the MnSZ (111) surface. The pure cubic zirconia surface is taken as the surface segregation-free zirconia substrate. On the other hand, for the surface Y- and Mn-segregated zirconia (111) substrates, the Zr atoms in the upper half of the pure zirconia surface are replaced with Y and Mn atoms respectively, and the compensating oxygen vacancies at the nearest neighbor (NN) were also taken into account.

Chapter 1 introduces us the research background of this thesis. Chapter 2 gives us the theory and computational methods of the thesis. The investigation of the initial stage of InN growth on YSZ substrates is shown in chapter 3. The mechanism of polarity determination of InN/YSZ is demonstrated in chapter 4. Regarding MnSZ, both the initial growth stage and the InN/MnSZ polarity determination are studied in chapter 5.

6.2 Initial stage of InN growth on segregation-free, Y-segregated and Mn-segregated zirconia (111) substrates

The initial stage of InN epitaxial growth on three kinds of cubic stabilized zirconia (111) substrates was investigated by the use of first principles calculations based on the density functional theory (DFT) with the generalized gradient approximation (GGA). The adsorption energies of an indium atom and a nitrogen atom on three kinds of cubic stabilized zirconia (111) surfaces were studied by total energy calculation.

In chapter 3 the adsorption on pure zirconia and Y-segregated zirconia surfaces are discussed. In chapter 5 the adsorption on the Mn-segregated zirconia surface is discussed. It has been found that the adsorption energy of a single N adatom on the zirconia surface is larger than that of a single In adatom, which means a nitrogen monolayer is more strongly bound to the substrate than an indium monolayer at the initial stage of the growth. These results indicate that the first layer of InN (0001)

should be a nitrogen layer. It is known that during the experiment of nitride growth, the inert N_2 gases are excited by the radiofrequency (RF) or electron resonance (ECR) plasma. As a result, the nitrogen source is very active compared to the metal source. This could be one important reason why the nitrogen atom has a large adsorption energy and is more strongly bound to the zirconia surface compared to the indium atom.

The energy differences between adsorption energies for indium atoms on various sites indicate that migration of In atoms on cubic stabilized zirconia (111) surfaces occurs easily. However, large differences between adsorption energies for N atoms on various sites suggested that N atoms tended to stay in one site with the largest adsorption energy for each of the zirconia substrates.

Deduced from the calculations, the most stable of the interfacial structures is the initial stage of the growth. The epitaxial relationships of InN (0001) // cubic zirconia (111) and InN [11$\bar{2}$0] // cubic zirconia [1$\bar{1}$0] could be obtained the same for all the three substrates. The theoretical study provided epitaxial relationships are quite consistent with the experimentally confirmed epitaxial relationships of InN growth on YSZ substrates. On the basis of these results it is shown that the InN film could be epitaxially grown on the cubic stabilized zirconia (111) substrates rightly independent of surface segregated dopants such as Y and Mn. It also can be demonstrated that the MnSZ acts as a better lattice matched substrate for InN growth even though there is no experimental result for such an InN/MnSZ system.

The sequence of adsorption energies on Mn-segregated surface, pure zirconia surface and Y-segregated zirconia surface has been substantiated. This indicates that the adsorption energy could be greatly affected by changing the dopants in cubic stabilized zirconia substrates. Detailed investigation of the local density of state (LDOS) has found that a metal dopant at the surface layer will affect the adsorption energy. In the case of the zirconia (111) surface, the first layer of (111) surface is the oxygen layer. The bonding between first layer of oxygen and the adatom plays the most important role in determining the adsorption energy. At the same time, the second layer

consisting of metal cations could also affect the adsorption energy according to the strength of the bonding interaction between the metal cation and the adatom. It has been found that effect of the segregated metal atoms depends on their own atomic characteristics, which is especially true for the *d*-orbital electrons of the metal atoms. For example, yttrium has fewer *d*-electrons and the Y-segregated substrate has smaller adsorption energies. Oppositely, manganese has more *d*-electrons and the Mn-segregated substrate has larger adsorption energy. Zirconium is in the middle of the three.

It has been shown that the initial stage is a very important factor to the crystalline quality of the subsequent InN film. It is found that the adsorption can be altered through the interaction between the metal cation and the adatom. Specifically, the effect of the dopants segregation provides us with a solution to replace metal atoms at the second layer. There will be different bond strength between the dopant and the adatom since various dopants are introduced in the zirconia surface. This means the adsorption of InN on the zirconia (111) will be modified according to the dopant concentration on the zirconia surface region. The change of the adsorption at the initial growth stage will subsequently affect the InN growth since the in-plane epitaxial relationship is determined by the adsorption. Finally, it has emerged that the N adsorption is so important because the epitaxial relationship is dependent on the N adsorption. At the same time the N adsorption could be affected by the metal dopants on the surface. Hence, the InN growth can be altered by selecting different kinds of dopant metal cations without changing the zirconia itself. According to the investigations in this work, the metal dopant with a small ionic size is favorable. The adsorption energy of film precursors such as In and N should be large. From this point of view, the Mn atom is considered to be a better candidate than Y atom. With the help of theoretical calculations, it is possible for us to predict the III-nitrides film growth at the initial stage and the in-plane epitaxial relationships between the III-nitrides film and the foreign substrates.

6.3 The polarity determination of *c*-InN on segregation-free, Y-segregated and Mn-segregated zirconia (111) substrates

To compare the stability of In-polar InN and N-polar InN on cubic stabilized zirconia (111) substrates, calculations of the adsorption energies of an indium atom on the nitrogen monolayer covering zirconia substrates were performed. The adsorption site for indium determines the polarity of InN. The adsorption of an indium atom at the center of three nitrogen atoms (''Hollow N'') leads to In-polarity InN, whereas the adsorption on the top of a nitrogen atom (''Top N'') corresponds to N-polarity InN.

The mechanisms of polarity determination on three kinds of cubic stabilized zirconia are discussed in this. In chapter 4, the stability of In- and N-polar InN on pure zirconia (111) and Y-segregated zirconia (111) substrates are discussed. In chapter 5, the stability of In- and N-polar InN on the Mn-segregated substrate are discussed. According to the results, for the pure zirconia surface, the energy difference between In- and N-polar is extremely small, which indicates that In-polar, N-polar and the mixture of the two are easily grown on the pure zirconia substrate. For the Mn-segregated surface, the adsorption energy for the In-polar InN is larger than that for the N-polar InN. From this result, it can be expected that the In-polar InN should predominantly grow on the MnSZ substrates without a mixture of In-polar and N-polar InN. For the Y-segregated surface, the energy difference is much greater than that of the MnSZ surface. This result indicates the In-polar InN is more stable and easier to be grown on the Y-segregated substrate compare to the MnSZ substrate.

A detailed study on the LDOS and the atomic interface structures for In-polar InN on all three substrates were performed to clarify the polarity mechanism of such results. It has been found that the In-polar InN structure could be stabilized by the interaction between top In atom and the surface oxygen of the zirconia substrates. Strong In-O interaction will stabilize the In-polar structure just like the stable In-polar structure on the Y-segregated surface. On the contrary, with weak In-O interaction such as on the

pure zirconia surface, the In-polar structure resting on it will become unstable. It is believed that all of these results could be attributed to the different metal atom layers at the surface region of the three zirconia substrates. The surface structure of zirconia will be changed when different metal atoms are segregated at the surface region. These metal atoms not only affect the N (or In) adsorption on the zirconia surface, but they also have their effect on the adsorption of In on the N-covered surface via the surface oxygen atoms. According to the results, the In-polar InN structure could be energetically stabilized and distinguished from the N-polar InN structure with Y or Mn dopants replacing the Zr at the zirconia (111) surface. Simply, enhancing the In-O bond strength by a small bond length will stabilize the In-polar structure.

It is known that polarity is an important issue for InN-based device fabrication because the polarity of the InN films seriously affects the device performance due to the generation of the spontaneous piezoelectric polarization fields. The polarity uniformity of the nitride film is absolutely required, and then the mixture of the two polarities should be avoided during growth. In this study it is clear that the In-O bonds affected by the surface segregated metal atoms, which will emphasize the In-polar structure and prevent the mixture of In- and N-polar InN growth once. Choosing the segregated dopants properly in the zirconia surface will be a promising method in the future to realize polarity uniformity and avoid the mixture of both In- and N-polar InN growth at the same time. According to the investigations contained, In-polar structure can be stabilized by the segregation of the dopant on the surface region. It can be predicted that in stabilized zirconia, the segregated transition metal atoms with fewer *d*-orbital valence electrons and shorter In-O bond length on the surface will be a good candidate for the growth control of the InN polarity. From this point of view, both Mn and Y atom are considered to be good candidates since the In-polar InN can be obtained on the YSZ and MnSZ substrates. Based on the results of polarity determination, it is known that theoretical study could be used to predict the polarity stability of the III-nitrides in the c-direction.

6.4 Future prospects

Nowadays the electrical property of the as-grown InN is still far away from the calculated value. Reducing the threading dislocation and improve the film quality is one of the great challenges in the InN field.

First principles calculations provide us a useful tool to investigate the InN film growth on the atomic scale. In this thesis, the growth mechanisms of InN on the zirconia (111) surface are investigated by theoretical study. The initial stage and the polarity determination of the InN film on zirconia (111) are elucidated. Both of these two factors are extremely important to of the electrical properties and InN-based device performance in the future works.

Theoretical study also helps us to theorize that the zirconia (111) surface is stabilized by Mn besides the Y dopants. It can be expected that InN grown on the MnSZ will have a low dislocation density because of the small lattice mismatch between the film and substrates. Accordingly, the electrical property of InN will be further improved. It is found that the initial growth stage and the polarity determination are also effected by the dopant atoms such as Mn and Y segregated at the zirconia surface. As the potential transport property of InN is unlocked, unique devices with excellent performance based on high quality InN could be expected in the future.

Acknowledgment

I left China after finishing the master program and started my Ph.D. program in Japan. Here, I have the great opportunity to study the group III-nitrides relevance. The Ph.D. experience is memorable. During this period I met different students, postdocs, professors, and staffs in the lab and on campus.

Foremost, I would like to express my sincerest gratitude to my supervisor Prof. Hiroshi Fujioka for continuous supports of my Ph.D. Study and research, for his guidance, patience, enthusiasm and valuable insights. The sound discussion, advice and assistance of research associate Shigeru Inoue, for which I am extremely grateful.

I am greatly indebted to the China Scholarship Council (CSC) for the financial support as the scholarship that gave me the great opportunity to pursue my studies in Japan. Thanks to all the members in the group of Prof. Fujioka with whom I spent memorable time during these years. Special thanks to their warm friendship, knowledge exchange, valuable discussion, close cooperation and help throughout the life in Japan.

Last but not the least, I would like to thank to my parents and relatives for their continuous encouragements and supports.

GUO Yao

Publications

1. Y. Guo, S. Inoue, A. Kobayashi, J. Ohta, and H. Fujioka, Theoretical study of the initial stage of InN growth on cubic zirconia (111) substrates, Phys. Status Solidi RRL **7**, 207 (2013).

2. Y. Guo, S. Inoue, A. Kobayashi, J. Ohta, and H. Fujioka, Theoretical investigation of polarity determination for *c*-plane InN grown on yttria-stabilized zirconia (111) substrates with yttrium surface segregation, Appl. Phys. Express **6**, 021002 (2013).

3. Y. Guo, S. Inoue, A. Kobayashi, J. Ohta, and H. Fujioka, Theoretical investigation of InN growth on Mn-stabilized zirconia (111) substrates, Thin Solid Films (submitted).